The Climber-Tether Interface of the Space Elevator

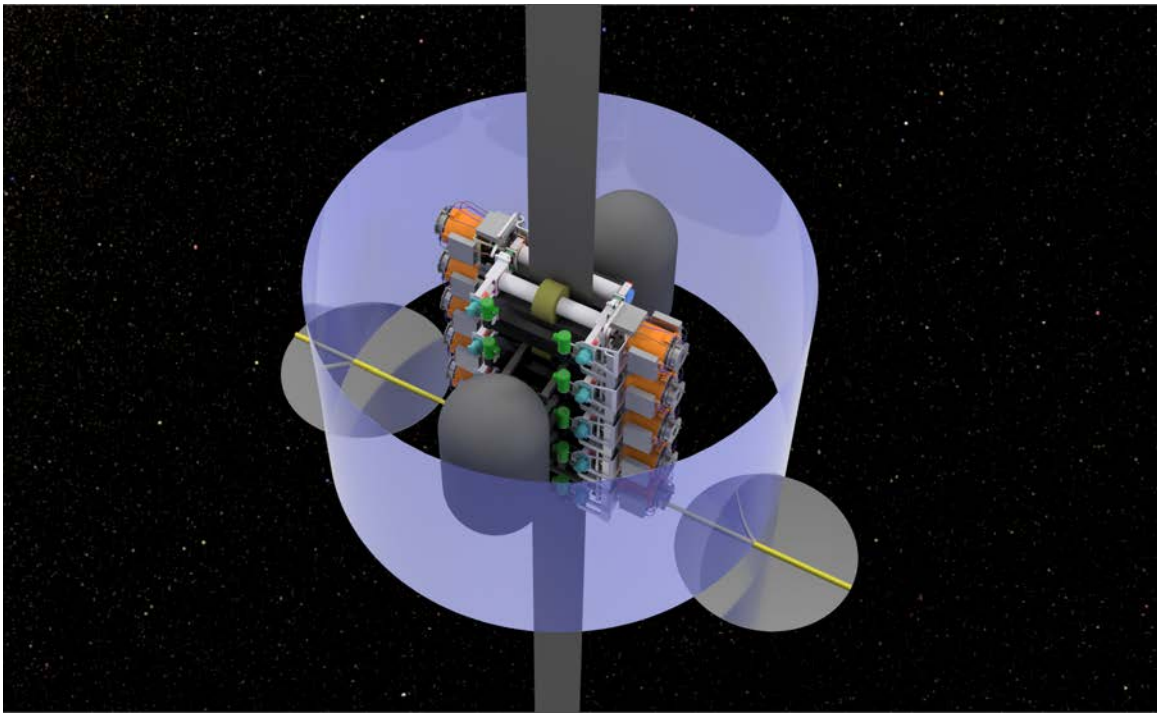

Dennis H. Wright
Larry Bartoszek
A.J. Burke
David Dotson
Hassan El Chab
John Knapman
Martin Lades
Adrian Nixon
Paul W. Phister, Jr.
Peter Robinson

The Climber-Tether Interface of the Space Elevator

International Space Elevator Consortium
Spring 2023

Authors:
Dennis H. Wright
Larry Bartoszek
A.J. Burke
David Dotson
Hassan El Chab
John Knapman
Martin Lades
Adrian Nixon
Paul W. Phister, Jr.
Peter Robinson

Preface

In order to increase the knowledge base in the field, the International Space Elevator Consortium (ISEC) undertakes each year the study of an issue important to the development of Earth-anchored space elevators.

At the inception of this study in 2020, recent advances in strong material technology made it clear that an in-depth examination of the state of the art of such materials would be useful. Enough was becoming known that the physical conditions at the interface between the space elevator climber and tether could be identified and used to determine the requirements of the strong materials. In the process, the study evolved into a multi-disciplinary effort, ranging from atomic physics and chemistry to aerospace and mechanical engineering to orbital mechanics. As a result, more than two years were required for its completion.

The goals of the study were to identify the physical conditions that must be met in order to allow climbing, to set forth the current state of the art in tether materials, to demonstrate by conceptual design that a payload-carrying climber could be built with today's technology and to outline the research necessary for future development of tethers and climbers.

It is hoped that the results of this study will convince the reader that advances in strong material development and climber design have brought the space elevator much nearer to reality.

Signed:

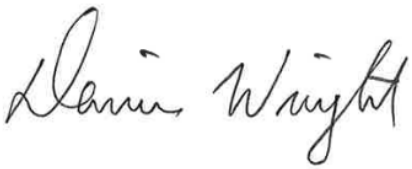

ISEC Vice President and Director of Studies
31 January 2023

Executive Summary

The "climbability" conditions of a space elevator climber, and those imposed by payload and speed requirements, determine the design of the climber and tether. For an Earth-based space elevator a frictional drive with opposing wheels gripping the tether and providing traction was chosen as the most feasible configuration. The physical conditions at the interface between the space elevator climber wheels and the space elevator tether determine whether or not climbing is possible.

These conditions were used to set limits on critical design parameters such as the coefficient of friction between tether material and wheels, the range of allowable climber wheel radii, the minimum torque to be supplied by drive motors or drive train, the minimum strengths (tensile, compressive and shear) of the tether and wheel materials and the amount of waste heat to be rejected by radiators.

Because mass production of single crystal graphene and graphene super-laminate (GSL) seems near at hand, GSL was selected as the tether material. While GSL has sufficient tensile and compressive strength to support itself and climbers, its shear strength may be too small. Cross-bonding graphene layers within GSL during production is one possible way to increase shear strength.

A conceptual design of the climber was conducted assuming that only present-day technology would be used. It showed that a system of ten wheel-pairs and twenty electric motors could not lift a 20 t climber, even without payload, but that five wheel-pairs and ten high-torque electric motors could lift a climber of 20 t having 9 t of payload.

Extrapolating current trends showed that many improvements in motor and material technologies are feasible and will allow reductions in climber mass with corresponding increases in payload. It thus seems possible that a 20 t climber with a 14 t payload will be achieved. These improvements include higher-torque, low-mass motors and tether materials specifically designed for better shear strength and higher coefficient of friction.

A number of unknown or poorly understood properties were identified which need to be studied or measured. A program of molecular modeling should be carried out so that the GSL manufacturing process can be understood and modified to provide the type of tether material needed. Because GSL is expected to be orthotropic, many of its elastic response parameters, along with its stress-strain curve, will need to be measured. Friction measurements will also be required.

Further improvements of the tether and the climber require a multi-parameter optimization of the climber and the tether designs. This is typically handled in a trade study for which a list of trades is provided.

Despite the challenges to friction-based tether climbing identified in this study, methods of overcoming them have been proposed and no roadblocks to the process have yet been found.

Table of Contents

Preface **3**

Executive Summary **4**

1 Introduction **8**
1.1 Constants and Nomenclature 9

2 The Climbability Condition **12**
2.1 Introduction 12
2.2 Local Climbability 13
2.2.1 Performance Parameters 15
2.2.2 Climber-Tether Interface 21
2.2.3 Climber 23
2.2.4 Tether 29
2.2.5 Scaling Laws 30
2.3 Summary 32

3 Tether Characteristics **34**
3.1 Purpose and Status 34
3.2 Materials 34
3.2.1 Graphene super-laminate 35
3.2.2 Hexagonal Boron Nitride 36
3.2.3 Carbon Nanotubes 36
3.3 Materials Manufacturing 36
3.3.1 Carbon nanotubes 36
3.3.2 Hexagonal Boron Nitride 37
3.3.3 Large-area Sheet Graphene 37
3.3.4 Manufacturing Summary 39
3.4 Design Considerations 39
3.4.1 Requirements 39
3.4.2 Lamination 42
3.4.3 Braiding 44
3.5 Molecular Modeling 44
3.6 Proposed Tether Design 45

4 Climber Design **47**
4.1 Design Philosophy 47
4.2 Assumptions in the Conceptual Design 47
4.3 Climber Components 48
4.3.1 Motors 48
4.3.2 Wheels, Axles and Bearings 50

4.3.3 Wheel Compression Mechanism . . . 54
4.3.4 Coupling Between the Axle and the Motor Drive Shaft . . . 62
4.3.5 Quick Disconnect Mechanism . . . 63
4.3.6 Power Distribution . . . 64
4.3.7 Brakes . . . 67
4.3.8 Interconnecting Structures . . . 67
4.3.9 Mass Budget . . . 73
4.4 Reducing the Weight of the Traction Drive . . . 73
4.4.1 Reducing the Wheel Radius . . . 73
4.4.2 Material Substitution . . . 75
4.4.3 Increasing Motor Torque . . . 77
4.5 Five-Wheel-Pair Climber Design . . . 78
4.5.1 Adapting the Climber Components to the Five-Wheel-Pair Design 79
4.5.2 Heat Dissipation . . . 82
4.5.3 Power Requirements . . . 85
4.6 Summary . . . 87

5 Projected Improvements **88**
5.1 Tether Material . . . 88
5.1.1 Coefficient of Friction . . . 88
5.1.2 Shear Strength . . . 89
5.2 Climber Improvements . . . 89
5.2.1 High Torque Motors . . . 89
5.2.2 Superconducting Motors . . . 90
5.2.3 Lighter Materials . . . 93

6 Proposed Research **95**
6.1 Molecular Modeling . . . 95
6.2 Material Properties . . . 97
6.2.1 Anisotropic Parameters . . . 97
6.2.2 Measurement and Testing . . . 99
6.2.3 Summary of Required Measurements . . . 100
6.3 Climber Redesign and Trade Study . . . 101
6.3.1 Improved Design . . . 101
6.3.2 Trade Study . . . 101

7 Summary **105**
7.1 Climber . . . 105
7.2 Tether . . . 105
7.3 Interface . . . 106
7.4 Challenges and Prospects . . . 107

Appendix A Choice of Climber Type **109**
A.1 Electrostatic Gripper . . . 109
A.1.1 Hexagonal Boron Nitride . . . 112
A.1.2 Critique . . . 112
A.2 Linear Induction Motors . . . 112
A.2.1 Critique . . . 115
A.3 Capstans . . . 116
A.3.1 Examples . . . 117
A.3.2 Critique . . . 118
A.4 Pinched Wheel Drive . . . 118
A.4.1 Critique . . . 119
A.5 Tank Tracks . . . 119
A.5.1 Critique . . . 121
A.6 Summary . . . 121

Appendix B Payload Example: Liquid Oxygen **122**

Appendix C Trade Space Methodology **127**

Appendix D Material Properties **130**
D.1 Mechanical Properties . . . 130
D.2 Electrical, Thermal and Optical Properties . . . 131
D.3 Titanium Alloy Properties . . . 132

Appendix E International Space Elevator Consortium **133**

Appendix F ISEC and IAA Studies **136**
F.1 ISEC Yearly Study Reports . . . 136
F.2 IAA Studies on Space Elevators . . . 137

1 Introduction

The first effort to quantify the viability of an Earth-based space elevator in terms of the strength of its tether, the mass of its climber and the logistics of constructing and maintaining it, was the space elevator feasibility condition (Shelef 2011). It assumed a simple space elevator concept (Edwards & Wesling 2002), which is linearly scalable, to set limits on payload throughput, power requirements and the rate at which a space elevator could replace itself.

The primary inputs to the feasibility condition are the tensile strength and material density of the tether; the tether must be strong enough and light enough to support itself and any devices that climb it. Materials that satisfy this requirement, such as single crystal graphene (SCG) (Xu et al. 2017), hexagonal boron nitride (hBN) (Wang et al. 2019) and some varieties of carbon nanotubes (Zhang et al. 2013) exist today in small quantities and it is expected that mass production of at least one of these will be seen in the near future (Nixon et al. 2021). An assessment of both tether and climber materials and their projected readiness for use was done by Swan, Raitt, Swan, Penny & Knapman (2013).

Assuming that sufficient amounts of strong material will become available, the next question is whether or not a payload-bearing climber can be built. A climber must be able to grip the tether and propel itself up or down or remain stationary. This requirement can be referred to as the climbability condition, which consists of the set of conditions, such as friction, pressure, shear and heat transfer, which exist at the interface between the climber and the tether. A determination of the likely range of values for each of these parameters will allow an estimate of whether or not climbability is possible.

The construction of a successful space elevator climber will require the optimization of a large number of parameters which apply at the climber-tether interface. In order to reduce this parameter space and concentrate thought, some assumptions about the type of climber must be made. Here, a frictional drive with opposing wheels gripping the tether and providing traction is the chosen method. Several other methods were considered but found lacking due either to inefficiency or insufficiently developed technology. These methods and critiques of them are provided in Appendix A.

A conceptual design using this method was developed and was used to establish minimum parameters for the climbability condition. The conceptual design assumes that only present-day (2023) technology is required for its construction, but projections are made for improvements based on near-future technology.

On the tether side of the interface, details of its construction will be important and must be examined down to the atomic level. Once again, assumptions were made to narrow the scope of study. Here, SCG or hBN, or a combination of the two are considered, with CNTs remaining a possibility for the future. The actual tether material is expected to consist of thousands of layers of SCG, hereafter referred to

as graphene super-laminate (GSL). Several tether fabrication methods are examined, including how to laminate atomically thin layers with cross-bonding for strength.

Having chosen both a tether material and a climber drive type, it is necessary to establish the values of the parameters for each. Although much is known about friction drives and how to build them, very little is known about the proposed tether materials. The field today is advancing rapidly and reliable parameter values are scarce. For this reason a substantial program of testing is required. An extensive list of parameters, relevant to the climber-tether interface, is proposed for measurement.

1.1 Constants and Nomenclature

The current topic spans several disciplines and many orders of magnitude in scale. This often leads to conflicts in terminology and reserved symbols for various constants. One particular case is the use of SI and English units. Here, SI units are used wherever possible. In some cases, though, where particular components are referred to, or software defaults are assumed, English units will appear. In these cases the corresponding conversion to SI will be included.

Other frequently used terms and constants are defined in the following tables.

Physical Constants

$\epsilon_0 = 8.854 \times 10^{-12}$	: permittivity of free space
$\mu_E = 3.9860 \times 10^5$ km^3/s^2	: gravitational parameter of Earth (Earth's mass × universal gravitational constant)
$G_{SC} = 1361$ W/m^2	: solar constant
$g = 9.80665$ m/s^2	: standard gravity
$\Omega = 7.29212 \times 10^{-5}$ rad/s	: angular velocity of Earth's rotation
$R_E = 6378$ km	: equatorial radius of Earth
$R_G = 42164$ km	: radius of geosynchronous orbit
$\sigma_{SB} = 5.6704 \times 10^{-8}$ W/m^2/K^4	: Stefan-Boltzmann constant

Units

K	: Kelvin
kg	: kilogram
km	: kilometers
ksi	: kilo-pounds per square inch = 6.895 MPa
N, kN, MN	: Newton, kiloNewton, megaNewton
Pa, MPa, GPa, TPa	: Pascal, megaPascal, gigaPascal, teraPascal
t	: metric ton = 1000 kg
ton	: US ton = 0.907185 metric ton
V, kV, MV	: volt, kilovolt, megavolt
W, kW, MW	: watt, kilowatt, megawatt

Acronyms

CFRC	: carbon fiber reinforced composite
CNT	: carbon nanotube
FEA	: finite element analysis
GEO	: geostationary Earth orbit
GSL	: graphene super-laminate
hBN	: hexagonal boron nitride
LEO	: low Earth orbit
SCG	: single crystal graphene

Variable and Parameter Names

α	: absorptivity of a radiating body
α_a, α_d	: angular acceleration, deceleration of wheel
A_c	: area of contact patch between wheel and tether
d	: radial deformation of wheel
E	: Young's modulus
ϵ_{motor}	: electric motor efficiency
ε	: emissivity of a radiating body
F_c	: compression force
F_t	: tractive force
f_{tav}	: ratio of trip-averaged clamp pressure to maximum clamp pressure
f_S	: average fractional surface area exposed to Sun
h	: altitude (distance above Earth's surface)
μ	: coefficient of friction
J	: rotational moment of inertia
j	: heat energy flux
κ	: electrical conductivity
λ	: thermal conductivity
M	: torque
m_c	: mass of climber
ν	: Poisson's ratio
N_{wheels}	: number of climber wheels
N_{wp}	: number of wheel-pairs
ω	: angular velocity
P_L	: limiting mechanical power
ρ	: mass density
R_W	: undeformed wheel radius
R_{eff}	: effective wheel radius averaged over deformations
σ	: compressive or tensile stress
S_f	: maximum fatigue stress
T	: temperature
ΔT	: differential tether tension
τ	: shear stress
v_{max}	: maximum climber velocity
W_W	: width of wheel

2 The Climbability Condition

2.1 Introduction

The primary function of a space elevator is to transport a payload between a planetary surface and space. Any climber carrying that payload must interact with the tether in order to ascend or descend. It must do so in a reasonable amount of time, while carrying an economically feasible payload and being durable enough to survive long travel times and distances. All of these requirements comprise a general condition referred to here as climbability.

The central issue is whether or not the climber can propel itself up or down. This is referred to as local climbability, so-called because it deals with the immediate vicinity in which the climber grips the tether and because it concerns only the physical parameters making climbing possible. Issues such as climber velocity, power availability or payload are not considered in this case.

The interactions at the interface between the tether and the climber traction device must be identified so that local climbability conditions can be quantitatively defined. If the initial climber design satisfies these conditions, the broader issues of power and velocity optimization, payload mass throughput and maintenance may be considered.

Defining the local climbability conditions requires understanding of properties in four mainf areas:

- **performance parameters**, including design-independent parameters such as speed, mass and power consumption,
- **tether**, including material composition, maximum stress and maximum pressure,
- **climber**, encompassing drive type, wheel radius, available torque and scaling laws, and
- **climber-tether interface**, encompassing coefficient of friction, maximum interface pressure, tractive force and thermal behavior.

Reference compendia of the current understanding is collected in Appendix D. These data reflect the current consensus in material parameters. At the time of this study, the tether material is not available in sufficiently large quantities for practical testing. Thus, some of its properties are based on anticipated or extrapolated values. Chapter 3 discusses existing candidate materials, their properties and the prospects for adapting them to space elevator use.

The properties of materials and their interactions can be categorized as mechanical, electromagnetic, chemical, thermal and optical/radiative. For a friction drive, in

this first assessment, electromagnetic, chemical and radiative aspects are not considered, although they are useful for the investigation of the details of friction, radiation damage and cross-bonding of tether layers, to name a few. The influence of those three, or the cross influence of all five properties, on the ultimate tether strength can be highly complex and is left for future investigation. This leaves mechanical and thermal interactions to be considered as the primary properties for the friction drive.

Ideally material properties and interactions would be fully parameterized and the optimal traction for a given tether/climber configuration could be determined with a simple formula for climbability. This would permit easy substitutions as engineering progresses. However, due to the complexity of the interactions, some parameters are best captured by using reference designs of the climber. Reference designs can be tested with today's materials, allowing the resulting performance parameters to be extrapolated into the ranges which apply to a space elevator.

The description of the climber-tether interface begins with the basic mechanical properties in vacuum, which are applicable to most of the elevator, and can demonstrate how a climber holds position, accelerates and climbs. Once a basic set of parameters is established, it can be extended later with more complex and higher-order effects. These include force distributions imposed by realistic climber designs and other modalities such as heating due to friction or external sources such as sunlight, chemical changes in the tether, high energy radiation interacting with materials, electromagnetic fields interacting with climber and tether and atmospheric effects such as wind, corrosion or lightning. All of these require further assessments.

2.2 Local Climbability

Regardless of the type of drive it uses, a climber can be viewed as a black box which consumes tether at one end and produces it at the other. Between the surface of the Earth and geosynchronous altitude, an ascending climber consumes high tension tether at its upper end and produces lower tension tether at its lower end. The difference of the tensions is the force that supports and accelerates the climber. How this difference is produced depends on the drive type. In what follows, it is assumed that the motor shaft is directly coupled to the axle without a gearbox or torque converter.

Figure 1 shows the essential part of an opposed-wheel friction drive: the tether and one of the two wheels which pinch it. As the wheel rotates, a tractive force F_t is generated from the compressive force F_c and the friction between the wheels and the tether. Electric motors provide the torque $M = R_W \times F_t$, where R_W is the wheel radius. The sum of tractive forces from multiple pairs of wheels increases the tension in the upper tether and decreases it in the lower tether so that $T_{up} - T_{down} = m_c[a(r) - g(r)]$, where m_c is the climber mass and $a(r)$ is the total acceleration as function of altitude which must overcome the effective gravity $g(r)$.

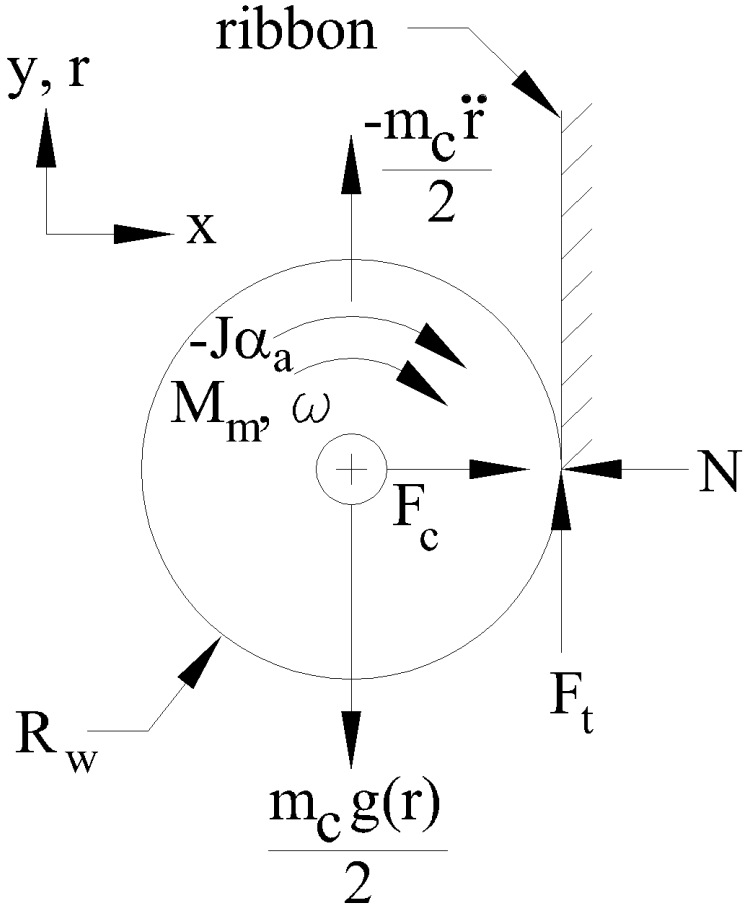

Figure 1: Free body force diagram for one climber wheel in contact with the tether. The compressive force F_c is directed perpendicular to the tether (ribbon) so that a normal force N is created. The tractive force F_t is generated by motors providing a torque M_m across a wheel radius R_W. The total upward acceleration $\ddot{r}$ must overcome the effective gravitational acceleration $g(r)$. m_c is the climber mass. ω is the angular velocity and α the angular acceleration of the wheel. The factor $\frac{1}{2}$ in the upward and downward forces reflects the fact that only one of the two pinching wheels is shown in the force diagram.

2.2.1 Performance Parameters

A large number of parameters, some as yet unknown, will have to be specified in order to build a working climber. Some do not directly affect the mechanics of the climber-tether interface, but need to be set as a starting point in the design of the climber. These parameters have to do with climber performance and were chosen on the basis of economics and efficiency.

Climber Mass

A 20,000 kg climber might consist of 6000 kg of climber mechanism and 14,000 kg of payload. These values are guesses which provide an economically attractive throughput to GEO (Edwards & Wesling 2002), while allowing a sufficient mass budget for the climber mechanism.

This study deals with the effects of a single climber on the tether. In operational mode, the space elevator will have several climbers on the tether at any one time. How their total mass and departure frequency will affect the tether load and mass is taken into account elsewhere (Robinson 2022).

Time of Climb to GEO and Maximum Power

The energy consumed by a climber as it travels from the surface of the Earth to GEO is critical to the commercial viability of the space elevator. Reasonable values of the energy require that power and transit time be balanced against one another, with power in this case meaning mechanical power only. Due to motor inefficiencies, large at lift-off and small at most other times, total power expended is always greater than mechanical power.

One method of power management is to cap the mechanical power of the climber. This results in a distinct power profile in each of four time periods which comprise the transit to GEO: initial acceleration from rest to maximum power (Δt_{ia}), constant maximum power (Δt_{cp}), gradual power reduction imposed by a constant climber speed limit (Δt_{cv}) and deceleration to rest at GEO (Δt_{dc}).

The initial acceleration is determined by the torque on each wheel axle:

$$M_{motor} = \alpha_a \left[J + m_w R_W^2 \right] + m_w R_W \left[\mu_E / R_E^2 - \Omega^2 R_E \right] , \tag{1}$$

where α_a is the angular acceleration of the wheel, $m_w = m_c / N_{wheels}$ is the climber mass apportioned among the wheels and J is the rotational moment of inertia of each axle, its bearings and couplings and the motor shaft which drives it. The first term on the right, then, is the torque due to the total rotational inertia of one assembly of wheel, axle and motor shaft. The second term is the torque due to the effective gravitational force (gravity minus centrifugal) at the surface of the Earth, apportioned per wheel.

Solving for α_a gives

$$\alpha_a = \frac{M_{motor} - m_w R_W \left[\mu_E / R_E^2 - \Omega^2 R_E\right]}{J + m_w R_W^2} \ , \tag{2}$$

which can be used to get the angular velocity and altitude as a function of time:

$$\omega = \alpha_a t \ , \ h = \frac{1}{2}\alpha_a R_W t^2. \tag{3}$$

The elapsed time t_L at which the limiting power P_L is reached is given by

$$P_L \ = \ \omega M(h=0) = \alpha_a t_L m_c \left[\mu_E / R_E^2 - \Omega^2 R_E\right] \ , \tag{4}$$

or

$$t_L \ = \ \frac{P_L}{\alpha_a m_c \left[\mu_E / R_E^2 - \Omega^2 R_E\right]} \ = \ \Delta t_{ia} \ , \tag{5}$$

where it is assumed that the altitude gained in time t_L is small enough that the effective gravity is unchanged.

The period of constant maximum mechanical power lasts until a climber speed limit is reached. With constant power and decreasing effective gravity as a function of altitude, the velocity would increase without limit. Practical considerations such as friction at the climber-tether interface, steering and the velocity-dependent Coriolis force make a speed limit necessary. The length of this period is

$$\Delta t_{cp} = \int_{h_1}^{h_2} \frac{dh}{v} \ , \tag{6}$$

where h is the altitude, h_1 is the altitude at which the power limit is first reached, h_2 is the altitude at which the speed limit is attained and v is the climber velocity. Noting that $v = R_W \omega$ and that

$$\frac{1}{\omega} \ = \ \frac{M(h)}{P_L} \ , \tag{7}$$

where $M(h)$ is the sum of the torque generated by all climber motors as a function of altitude,

$$M(h) = R_W m_c \left[\frac{\mu_E}{(R_E + h)^2} - \Omega^2 (R_E + h)\right] \ , \tag{8}$$

with m_c the climber mass. Noting

$$\int_{h_1}^{h_2} \frac{dh}{v} \ = \ \int_{h_1}^{h_2} \frac{dh}{R_W \omega} \ = \ \frac{1}{P_L R_W} \int_{h_1}^{h_2} M(h) dh \tag{9}$$

allows the time to be calculated:

$$\int_{h_1}^{h_2} \frac{dh}{v} \ = \ \frac{m_c}{P_L} \int_{h_1}^{h_2} \left[\frac{\mu_E}{(R_E + h)^2} - \Omega^2 (R_E + h)\right] dh \ , \tag{10}$$

so that

$$\Delta t_{cp} = \frac{m_c}{P_L}\Big[\mu_E\Big(\frac{1}{R_E+h_1} - \frac{1}{R_E+h_2}\Big) - \Omega^2\Big(\frac{(R_E+h_2)^2-(R_E+h_1)^2}{2}\Big)\Big] \ . \qquad (11)$$

It remains to determine h_2, the altitude at which the speed limit begins. This is the greatest altitude attained before the power dips below P_L. Thus,

$$P_L \ = \ v_{max}F(h_2) \ = \ v_{max}m_c\big[\frac{\mu_E}{(R_E+h_2)^2} - \Omega^2(R_E+h_2)\big] \ . \qquad (12)$$

The term in brackets is the difference of the gravitational and centrifugal accelerations. Noting that the geosynchronous radius R_G can be defined by

$$\frac{\mu_E}{R_G^2} \ = \ \Omega^2 R_G \ , \qquad (13)$$

so that Equation 12 may be rewritten as

$$\frac{P_L}{m_c v_{max}} \ = \ R_G\Omega^2\big[\frac{R_G^2}{(R_E+h_2)^2} - \frac{(R_E+h_2)}{R_G}\big] \ . \qquad (14)$$

Rearranging further,

$$\Big(\frac{R_E+h_2}{R_G}\Big)^3 + \frac{P_L}{m_c v_{max} R_G \Omega^2}\Big(\frac{R_E+h_2}{R_G}\Big)^2 - 1 \ = \ 0 \ , \qquad (15)$$

which can be solved for h_2.

The time to traverse the region of constant velocity is

$$\Delta t_{cv} \ = \ \frac{h_3-h_2}{v_{max}} \ , \qquad (16)$$

where h_3 is the altitude at which deceleration begins. Assuming constant deceleration,

$$h_3 = R_G - R_E - \frac{1}{2}R_W\alpha_d\Delta t_{dc}^2 \ , \qquad (17)$$

with

$$\Delta t_{dc} \ = \ \frac{v_{max}}{R_W\alpha_d} \qquad (18)$$

and α_d the angular deceleration.

The total transit time is then

$$\Delta t \ = \ \Delta t_{ia} + \Delta t_{cp} + \Delta t_{cv} + \Delta t_{dc} \ , \qquad (19)$$

or, using Equations 5, 11, 16 and 18,

$$\Delta t \;=\; \frac{P_L}{\alpha_a m_c\big[\mu_E/R_E^2 - \Omega^2 R_E\big]} + \frac{m_c}{P_L}\Big[\mu_E\Big(\frac{1}{R_E+h_1} - \frac{1}{R_E+h_2}\Big) - \Omega^2\Big(\frac{(R_E+h_2)^2-(R_E+h_1)^2}{2}\Big)\Big] + \frac{h_3-h_2}{v_{max}} \;+\; \frac{v_{max}}{R_W\alpha_d}\;. \quad (20)$$

The time to GEO thus depends on five climber parameters: the specific power P_L/m_c, the maximum speed v_{max}, the initial angular acceleration α_a, the final angular deceleration α_d and the wheel radius R_W. α_a in turn depends on R_W, the motor torque M_{motor}, J and the climber mass per wheel.

A past climber study (Swan, Swan, Penny, Knapman & Glaskowsky 2013) suggested that reasonable values of the limiting power and maximum velocity would be 4 MW and 200 km/h (55.56 m/s). As mentioned in Chapter 4, a high-torque motor could provide $M_{motor} = 5600$ N-m at 1900 RPM. It would drive a likely angular moment of inertia of $J = 5$ kg m^2. For a 20,000 kg climber with ten wheels, the climber mass per wheel, m_w, is 2000 kg. To achieve a velocity of 200 km/h at 1900 RPM requires a wheel radius $R_W = 0.2794$ m, so that Equation 2 gives

$$\alpha_a = \frac{5600 \text{ N-m} - (2000 \text{ kg})(9.8 \text{ m/s}^2)(0.2794 \text{ m})}{5 \text{ kg m}^2 + (2000 \text{ kg})(0.2794 \text{ m})^2} \;=\; 0.768 \;\; \text{s}^{-2}\;.$$

With the specific power $P_L/m_c = 200$ W/kg and the above value for the angular acceleration, the time it takes to reach that power is given by Equation 5 :

$$\Delta t_{ia} \;=\; \frac{200 \text{ W/kg}}{(0.2794 \text{ m})(9.8 \text{ m/s}^2)(0.768/\text{s}^2)} \;=\; 95.1 \text{ s}\;.$$

The velocity and altitude reached at that time follow from Equation 3 :

$$v \;=\; R_W\alpha_a t_L \;=\; 20.4 \text{ m/s} \;=\; 73.5 \text{ km/hr}\;,$$

$$h_1 \;=\; 0.5(0.768/\text{s}^2)(0.2794 \text{ m})(95.1 \text{ s})^2 \;=\; 970 \text{ m}\;.$$

With the above values of specific power and maximum velocity, Equation 15 can be solved for h_2, giving 4064 km. Using $h_2 = 4064$ km and $h_1 = 0.97$ km in Equation 11 yields the total time at limited power $\Delta t_{cp} = 120{,}660.5$ s = 33.52 h = 1.40 d.

The deceleration time is small even with small deceleration, so its value is somewhat arbitrary. Setting it to twice the initial acceleration, $\alpha_d = 1.536$ s^{-2}, so that the time it takes to stop is (Equation 18)

$$\Delta t_{dc} \;=\; \frac{55.56 \text{ m/s}}{(0.2794 \text{ m})(1.536 \text{ s}^{-2})} \;=\; 129.5 \text{ s}\;.$$

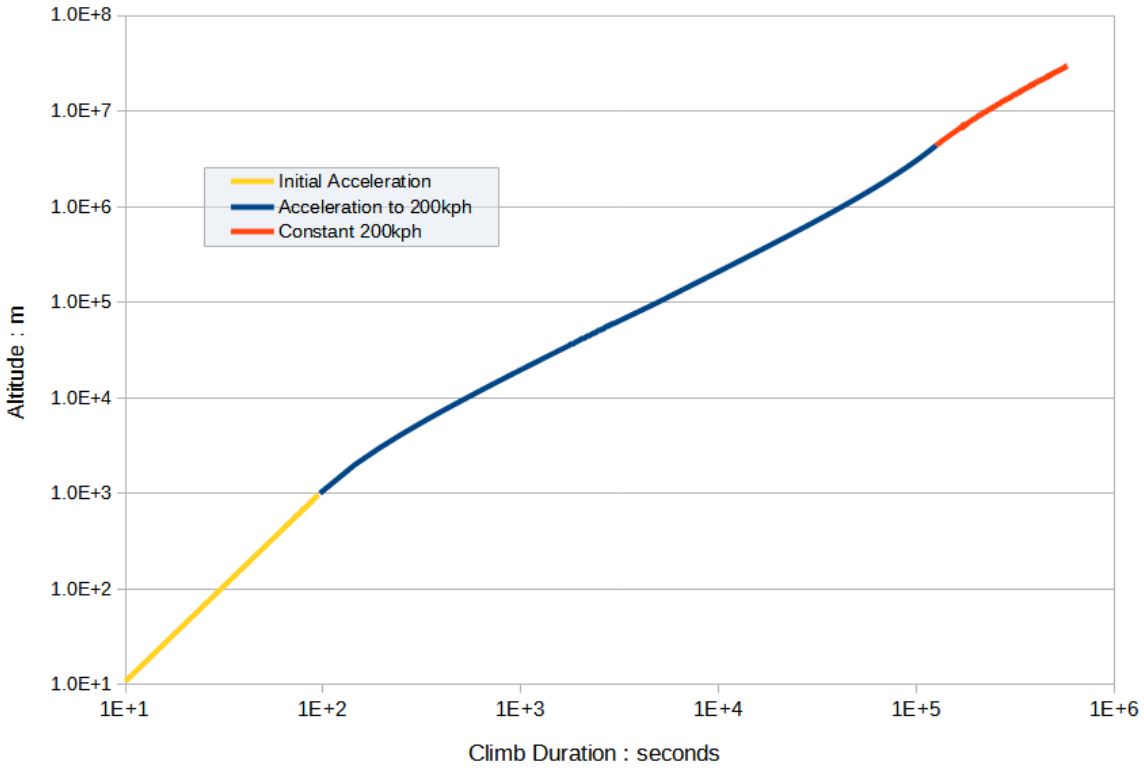

Figure 2: Log-log plot of altitude vs. time for a 20,000 kg climber illustrating three of the four distinct climber power regions: constant acceleration limited by motor torque (yellow), constant power limited to 4 MW (blue) and constant velocity, 200 km/hr (red). The constant deceleration region does not appear due to its short duration.

The stopping distance is

$$0.5(1.536\ \text{s}^{-2})(0.2794\ \text{m})(129.5\ \text{s})^2\ =\ 3596\ \text{m}\ .$$

Finally, the total time at maximum velocity is, from Equation 16

$$\Delta t_{cv}\ =\ \frac{(42164-3.6)\ \text{km}-(6378+4064)\ \text{km}}{200\ \text{km/hr}}\ =\ 158.59\ \text{hr}\ =570,931.2\ \text{s}\ ,$$

The total travel time is thus 95.1 + 120,660.5 + 570,931.2 + 129.5 = 691,816.3 s = 192.17 hr = 8.01 d. If a higher climber velocity were possible, for example 300 km/hr, the specific power could be lowered to 150 W/kg, giving a total transit time of 6.51 d.

The periods of climber power are shown in the altitude vs. time plot of Figure 2 and a summary of altitude and time values for each power region is shown in Figure 3.

Climber and Tether Environment

Parameters related to the robustness of materials against the electromagnetic, radiation and chemical surroundings are currently not available in detail for this study.

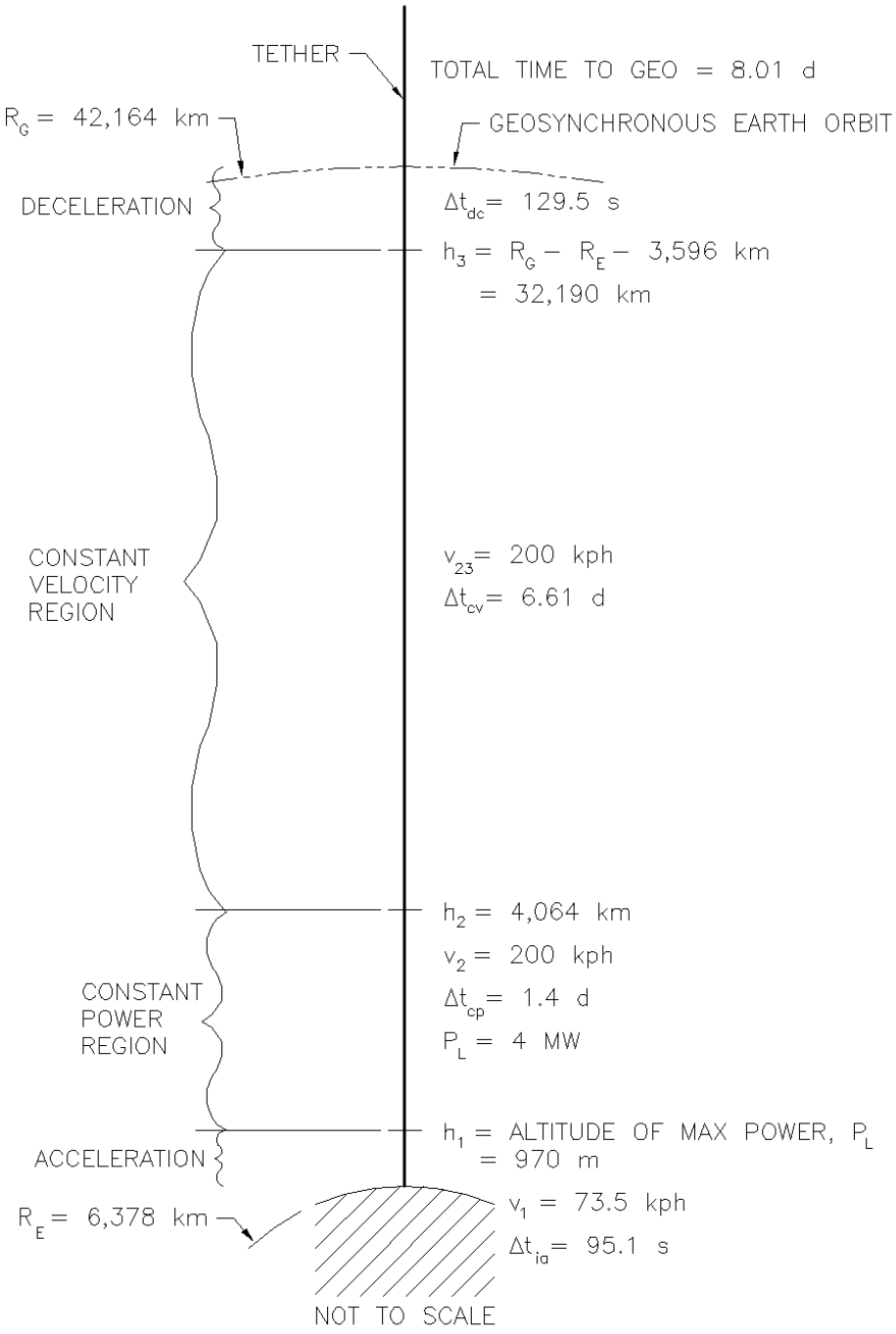
TETHER
TOTAL TIME TO GEO = 8.01 d
R_G = 42,164 km
GEOSYNCHRONOUS EARTH ORBIT
DECELERATION
Δt_{dc} = 129.5 s
$h_3 = R_G - R_E$ = 3,596 km
= 32,190 km
CONSTANT VELOCITY REGION
v_{23} = 200 kph
Δt_{cv} = 6.61 d
h_2 = 4,064 km
v_2 = 200 kph
CONSTANT POWER REGION
Δt_{cp} = 1.4 d
P_L = 4 MW
h_1 = ALTITUDE OF MAX POWER, P_L
= 970 m
ACCELERATION
v_1 = 73.5 kph
R_E = 6,378 km
Δt_{ia} = 95.1 s
NOT TO SCALE

Figure 3: Summary plot of altitude and time values for 8 day climb from Earth's surface to GEO

2.2.2 Climber-Tether Interface

Conditions at the interface between the climber wheel and tether can be understood in terms of the contact patch. Hertzian contact theory provides a way to calculate the stresses in this region, given the material parameters of wheel and tether, the coefficient of friction between them and the forces applied by the climber mechanism. The resulting interface stresses define the minimal material strengths required for climbing and allow estimates of heat build-up in the wheels and tether.

Friction The key parameter in converting the compressive force supplied by the climber into tractive force is the coefficient of friction μ,

$$F_t = \mu F_c \ . \tag{21}$$

μ depends on the materials and surfaces of the two components in contact and is almost always an empirical parameter, rather than one that can be calculated. For most mechanical applications, the value of μ between two materials is well measured, but in the case of SCG it is not. Almost all measurements to date use atomic force microscopes with diamond-tipped probes, leading to values of μ more appropriate to SCG-carbon interfaces than to SCG-metal interfaces. A recent diamond-probe value of μ for SCG is 0.03 (Table 5), in the lubricant range. Metal-tipped probes, when they become available, may return more applicable values, and these may be higher.

For practical applications, μ must be greater than 0.05, though 0.1 is much more common. If new data do not reveal a higher coefficient of friction, it is possible to modify graphene super-laminate (GSL) to increase it. Methods to do so are discussed in Chapter 3. In the calculations that follow, $\mu = 0.1$ is assumed to be the minimum value.

Temperature

The maximum temperature at the interface must not be greater than the lower of the maximum operating temperatures of the wheel or the tether,

$$T_{interface} \leq min(T_{maxW}, T_{maxT}). \tag{22}$$

The melting temperature of SCG (5500 K, Appendix D) is much higher than that of any likely wheel material. Titanium alloys, for example, melt at around 1900 K. This suggests that the maximum tether operating temperature will be much higher than that of the climber wheels. Thus, the wheel material determines the interface maximum, and wheel cooling must be considered.

Pressure

The area of contact between the drive wheel and the tether, and the pressure there, can be calculated by Hertzian contact theory (Shigley & Mischke 1989). For a

cylinder pressed against a plane, the area of the elliptical contact patch is given by

$$A_c = \sqrt{\frac{\pi R_W W_W F_c}{E^*}} \;\; with \;\; \frac{1}{E^*} = \frac{1-\nu_1^2}{E_1} + \frac{1-\nu_2^2}{E_2} \; . \tag{23}$$

F_c is the compressive force clamping the wheels together, R_W is the radius of the wheel and W_W is the width of the wheel. E_1 and E_2 are the Young's moduli of the tether and wheel materials, respectively, and ν_1 and ν_2 are the corresponding Poisson's ratios. The maximum pressure is

$$P_{max} = \frac{F_c}{A_c} = \sqrt{\frac{E^* F_c}{\pi R_W W_W}} \; . \tag{24}$$

Contact theory assumes that both the tether and wheels can be treated as solids. The wheels use cutouts to reduce mass, leading to a possible departure from behavior as a solid cylinder. This is likely a small effect and at any rate would increase the contact area, thereby decreasing the maximum pressure. The tether will be very thin, about 10 μm at its thinnest. It is questionable, then, if it can be treated as a solid plane. An alternate calculation assumes that the tether can be neglected in determining the contact area and pressure. In that case, cylinder-on-cylinder contact must be calculated. Assuming that the two wheels are identical in radius and material, Equations 23 and 24 can be used, but with $E^* = E_2/(1-\nu_2^2)$.

For the particular materials used here, GSL and titanium alloy (Ti-6Al-4V), the two methods give similar results. Using values from a reference climber design (see Chapter 4), $F_c = 355{,}858$ N, $R_W = 0.2794$ m and $W_W = 0.3$ m. For a tether, $E_1 = 1$ TPa and $\nu_1 = 0.456$. For a titanium alloy wheel, $E_2 = 113.8$ GPa and $\nu_2 = 0.342$. The cylinder-on-plane contact area and pressure are then

$$A_c = 8.95 \text{ cm}^2 \; , \;\; P_{max} = 397 \text{ MPa} \; . \tag{25}$$

For the cylinder-on-cylinder case, $E^* = 128.9$ GPa to get

$$A_c = 8.53 \text{ cm}^2 \; , \;\; P_{max} = 417.4 \text{ MPa} \; . \tag{26}$$

These values are close to those for the cylinder-on-plane case. Since the maximum pressure is of interest, the cylinder-on-cylinder values will be used going forward.

Maximum Combined Stress

The only mechanical stress at the interface is pressure. An effectively rigid climber chassis and the choice of a pinched-wheel drive make torsion and bending negligible. Neither tension nor shear are intrinsic to the interface; each has different values on the tether side and on the wheel side. The applied stresses, tension, compression and shear, in the wheel are

$$\sigma_t = 0 \; , \; \sigma_c = P_{max} \; , \; \tau = \frac{F_t}{A_c} \; , \tag{27}$$

where F_t is the tractive force from the wheel, and in the tether are

$$\sigma_t = \frac{\Delta T}{A_t} \ , \ \sigma_c = P_{max} \ , \ \tau = \frac{\Delta T}{A_c} \ , \tag{28}$$

where A_t is the cross sectional area of the tether and ΔT is the difference in tether tension above and below the climber.

The Mohr combined stresses will be functions only of σ_c, σ_t and τ:

$$\sigma_1 = \frac{\sigma_t + \sigma_c}{2} + \sqrt{\left(\frac{\sigma_t - \sigma_c}{2}\right)^2 + \tau^2} \ , \tag{29}$$

$$\sigma_2 = \frac{\sigma_t + \sigma_c}{2} - \sqrt{\left(\frac{\sigma_t - \sigma_c}{2}\right)^2 + \tau^2} \ , \tag{30}$$

$$\tau_{max} = \sqrt{\left(\frac{\sigma_t - \sigma_c}{2}\right)^2 + \tau^2} \ , \tag{31}$$

where σ_1 and σ_2 are the principal maximum and minimum normal stresses and τ_{max} is the combined maximum shear stress. These values are limited by the maximum operating stresses of the tether and wheel materials.

2.2.3 Climber

Conditions for the climber include lift, wheel stress, available torque, the range of possible wheel radii and the rates at which heat is built up and dissipated. Lift, wheel stress and available torque depend directly on tractive force, while the wheel radius and heat have more complex dependencies.

Lift

The pinched-wheel reference configuration provides traction by symmetrical compression of the tether between two wheels. The tractive force F_t per wheel increases the tether tension above and decreases it below the wheel pair, causing a differential

$$\Delta T \ = \ 2F_t \ . \tag{32}$$

Lift occurs when

$$N_{wp}\Delta T \ = \ 2NF_t \ > \ m_c[g(r) - c(r)] \ . \tag{33}$$

$g(r)$ and $c(r)$ are the gravitational and centrifugal accelerations at the equator as a function of altitude and N_{wp} is the number of wheel pairs of the climber.

At $r = R_E$, $g(r) - c(r) = 9.78$ m/s^2, so that a 20,000 kg climber has a force of $(9.78 \text{ m/s}^2)(2 \times 10^4 \text{ kg}) = 195.6$ kN. For five wheel-pairs, the tractive force per wheel required to accelerate the climber is then $F_t > 19.56$ kN, or a tension difference of 39.12 kN.

Wheel Stress Near the Interface

Equation 27 gives the applied stresses in the wheel near its interface with the tether. Except for σ_t, these vary with altitude. From Equation 24, P_{max}, and hence σ_c, is proportional to the square root of the axle clamping force F_c. Using Equations 21 and 23, the shear can be re-expressed as

$$\tau \;=\; \frac{F_t}{A_c} \;=\; \mu F_c / \sqrt{\frac{\pi R_W W_W F_c}{E^*}} \;=\; \mu \sqrt{\frac{F_c E^*}{\pi R_W W_W}} \;=\; \mu P_{max} \;, \tag{34}$$

so that the shear, too, is proportional to $\sqrt{F_c}$. F_c is largest at the Earth's surface, but can be reduced with increasing altitude as $g(r) - c(r)$ decreases. Maximum stresses, then, are to be calculated at the Earth's surface.

The applied stresses $\sigma_t = 0$, $\sigma_c = P_{max}$ and $\tau = \mu P_{max}$ are used in Equations 29, 30 and 31 to get the combined stresses, which must be less than the yield and shear strengths for the wheel material:

$$\sigma_1 = \frac{P_{max}}{2}[\sqrt{1+4\mu^2}+1] \;< \sigma_{ty} \;, \tag{35}$$

$$\sigma_2 = \frac{P_{max}}{2}[\sqrt{1+4\mu^2}-1] \;< \sigma_{cy} \;, \tag{36}$$

$$\tau_{max} = \frac{P_{max}}{2}\sqrt{1+4\mu^2} \;< \tau_y \;. \tag{37}$$

Table 1 shows the above stresses using $\mu = 0.1$ and $P_{max} = 417.4$ MPa, compared to the material strengths listed in Table 7 of Appendix D. All the maximum stresses induced by the interface pressure and friction are well below the wheel material yield strengths.

Stress	Value (MPa)	Yield Strength (MPa)
σ_1	421.5	$\sigma_{ty} = 880$
σ_2	4.1	$\sigma_{cy} = 970$
τ	212.3	$\tau_y = 550$

Table 1: Combined Stresses in Ti-6Al-4V Alloy

Torque and Angular Momentum

In order to hold and accelerate a wheeled climber, each of the wheel drives must supply the tractive force F_t acting at a lever arm which is the wheel radius R_W:

$$M_m = F_t R_W \;. \tag{38}$$

Maximum torque will be required when the climber starts its ascent. The acceleration must be $g - c + a$, where $g - c$ is the net of the gravitational and centrifugal

accelerations at the equator and a is the acceleration required to move upward. a is given by the wheel radius times the initial angular acceleration given in section 2.2.1:

$$a = 0.768 \text{ s}^{-2} \times 0.2794 \text{ m} = 0.215 \text{ m/s}^2 \ .$$

The total acceleration required is then about 10 m/s^2 (9.78 + 0.215) and the climber mass per motor is 2000 kg. The motor must supply a torque of $F_t \times R_W$ = 10 m/s^2 × 2000 kg × 0.2794 m = 5585 N-m or about 5600 N-m.

At the point of lift-off, the angular velocity of a wheel is $\omega = 0$. Assuming the acceleration is constant at its initial, torque-limited value, ω increases linearly with time until maximum mechanical power (4 MW) is reached. At that point its value will be 73 s^{-1} or 697 RPM, according to Equation 5. The required torque falls off with increasing altitude so that, in the power-limited regime, ω increases to about 1900 RPM.

Wheel Radius

The climber wheel radius is a key design parameter, with a range of values limited by drive motor performance, material fatigue and axle spacing. The upper limit on the radius is imposed by the maximum torque that can be supplied by the motors,

$$R_W < \frac{M_{max}}{F_t} \ , \tag{39}$$

where F_t is the tractive force shown in Figure 1 and M_{max} is the rated torque of the motor. The tare weight of the climber must be as small as possible, so the mass of the wheel could also limit the radius. However, with strong, lightweight materials and weight-efficient design, the torque provides a tighter upper limit. Purpose-built electric motors with masses around 200 kg can deliver 5700 N-m of torque (HelixMotor 2022). With a tractive force $F_t = 19,620$ N per climber wheel, R_W could be as large as 0.29 m.

A lower limit on the wheel radius can be set by fatigue considerations. A climber wheel will make millions of revolutions on a trip to GEO. Each time a portion of the wheel surface comes into contact with the tether, the wheel is locally compressed and expands again after it rotates out of contact. The repeated flexing of the wheel material causes fatigue, which can be expressed as a stress. The maximum fatigue stress that a material can sustain decreases exponentially as a function of the number of cycles until it reaches a constant, infinite cycle value.

High cycle fatigue stress is measured for many materials. Table 2 shows the maximum stress for titanium alloy Ti-6Al-4V at several cycle values. These values reflect the 50% confidence level, which means failure will occur 50% of the time when the given cycle number is reached. The 50% confidence level values were taken from Janecek et al. (2015). For greater reliability, these values were converted here to the 97.5% confidence level.

Cycles	1.2×10^5	1.0×10^7	4.8×10^8	8.2×10^9
50% C.L.	0.571	0.515	0.470	0.439
97.5% C.L.	0.487	0.429	0.384	0.353

Table 2: Maximum Fatigue Stress (GPa) of Ti-6Al-4V Alloy

To get an idea of how many cycles a wheel might survive, the 97.5% values should be compared to the average pressure at the wheel-tether contact patch. The contact pressure, supplied by the axle clamps, will be greatest at the surface of the Earth and decrease as the climber ascends into lower effective gravity. The pressure averaged over the trip to GEO is

$$P_{av} = f_{tav} P(R_E) \ , \tag{40}$$

where $P(R_E)$ is the contact pressure at Earth's surface and

$$f_{tav} = \frac{1}{R_G - R_E} \int_{R_E}^{R_G} dr \big(\frac{\mu_E}{r^2} - \Omega^2 r\big) \ \Big/ \ \Big(\frac{\mu_E}{R_E^2} - \Omega^2 R_E\Big) \ = \ 0.139 \ . \tag{41}$$

Contact theory gives the pressure as a function of wheel radius. Taking the pressure in Equation 24 to be the maximum fatigue stress S_f, an inequality for the wheel radius R can be found :

$$R_W > \frac{E^* F_c}{\pi w S_f^2} \ . \tag{42}$$

Applying the clamp force fraction f_{tav} and noting that $E^* = E/(1-\nu^2)$,

$$R_W > \frac{f_{tav} F_c}{\pi w S_f^2 (1-\nu^2)/E} \ . \tag{43}$$

From Table 2 it can be seen that the fatigue stress curve flattens out at very high cycles. The 97.5% CL values do not change much above 10^9 cycles, where they are between 0.35 and 0.37 GPa. Taking $S_f = 0.36$ GPa, $F_c = 355,858$ N, $w = 0.3$ m and $E/(1-\nu^2) = 129.1$ GPa, Equation 43 gives

$$R_W > \frac{0.139(355,858 \text{ N})}{\pi(0.3 \text{ m})(0.36 \text{ GPa})^2/129.1 \text{ GPa}} = 0.052 \text{ m} \ .$$

With this minimum radius, a wheel would make 110 million revolutions on a trip to GEO and survive perhaps 100 such trips.

The wheel radius is thus bounded,

$$\frac{M_{max}}{F_t} > R_W > \frac{f_{tav} F_c}{\pi w S_f^2 (1-\nu^2)/E} \ . \tag{44}$$

Other considerations may constrain R_W further as the climber design evolves.

Climber Heating

Drive motor inefficiency, solar radiation, resistive losses in electrical buses and electronics, wheel-tether friction and elastic deformation of the climber wheels all contribute to the heat that builds up during climber operation. The heat must be dissipated at a rate sufficient to maintain the ambient climber temperature at reasonable operating levels for equipment and payloads. The only means to do this is by radiation since, for most of its journey, the climber is in vacuum.

Motor inefficiency and solar radiation are by far the largest sources of heat and the only ones that need be taken into account for a first estimate of the mass of a radiative cooling system.

A typical efficiency for electric motors is 96%, so at an average power consumption of 4 MW, 160 kW of waste heat will be generated.

The flux density of solar radiation in space is given by the solar constant G_{SC}. This is for a surface constantly illuminated by, and whose perpendicular points directly at, the Sun. For practical applications this value will be reduced by a factor f_S, which takes into account, among other things, day-night cycles and changes in the orientation of the spacecraft with respect to the Sun. In a constant power scenario the climber will spend most of its time at low altitudes where the day-night cycle is dominant. Also, the radiator panels will not always point directly at the Sun, especially if they form a cylindrical or spherical shell around the climber. An estimate of $f_S = 0.33$ is reasonable and the effective solar flux will be $f_S G_{SC}$ or 450 W/m^2.

The electrical bus that delivers current to the drive motors will be exposed to vacuum and radiate I^2R losses quickly. These losses, about 3800 W, thus do not contribute to the heat budget. Onboard electronics, used for control and communication, do contribute and can have large inefficiencies between 30 and 70%. Without a detailed design of the climber's onboard systems, it is difficult to estimate the waste heat from this source, but it seems reasonable to say that it will not be large compared to the heat generated by the motors.

Friction between the drive wheels and tether can be divided into two parts, sticking and slipping. In the sticking, or adhesion, region of the contact patch, there is static friction but no kinetic friction and therefore no energy loss. Kinetic friction occurs in the slip zone where the forward velocity of the axle v is larger than the product of the axle rotational velocity ω and the effective wheel radius R_{eff}. The fraction of the contact patch which undergoes kinetic friction can be estimated roughly by the slippage:

$$S = 1 - \frac{\omega R_{eff}}{v} \ . \tag{45}$$

The radius R_{eff} takes into account the deformation of the wheel as it is pressed into the tether, or the opposing wheel. Contact theory gives the value d of the deformation, so that

$$R_{eff} \approx R(1 - \frac{d}{3R}) \ , \tag{46}$$

where R is the undeformed wheel radius. Substituting Equation 46 into Equation 45 and using $v = R\omega$ gives

$$S = 1 - \frac{R_{eff}}{R} \; = \; \frac{d}{3R} \; = \; \frac{\omega d}{3v} \; . \tag{47}$$

The "slip velocity", $\frac{\omega d}{3}$ can be used to get the power of kinetic friction at its highest near the Earth's surface:

$$P_f = m_c g \mu \frac{\omega d}{3} \; , \tag{48}$$

with g the standard gravity, μ the coefficient of friction and m_c the climber mass. For titanium alloy wheels on a graphene tether, the wheel deformation d is about 11 μm. For $\mu = 0.1$, $\omega = 3000$ rpm and $m_c g = 196$ kN for a 20,000 kg climber, the power going into frictional heat is 22.6 W, a negligible amount.

Repeated deformation of the climber wheels as their surfaces rotate into and out of contact with the tether will be elastic rather than plastic. The resultant release of heat is therefore expected to be small and will be neglected in the current estimate.

Climber Cooling

The requirements of the heat rejection system can be estimated using the Stefan-Boltzmann law for black body radiation,

$$j = \sigma_{SB} T^4 \; , \tag{49}$$

where j is the energy flux, σ_{SB} is the Stefan-Boltzmann constant and T is the temperature of the radiating body. The radiated power P is given by

$$P = A \varepsilon \sigma_{SB} (T^4 - T_{sink}^4) \; , \tag{50}$$

where A is the area of the radiator, ε is the emissivity of the radiating body and T_{sink} is the sink temperature, in this case the average temperature of space surrounding the climber. The total rejected power requirement is then

$$P_{rejected} = P_{motors} \frac{1 - \epsilon_{motor}}{\epsilon_{motor}} + \alpha f_S G_{SC} A = \varepsilon \sigma_{SB} (T^4 - T_{sink}^4) A \; , \tag{51}$$

where P_{motors} is the mechanical power to the driver motors, ϵ_{motor} is the motor efficiency and α is the absorptivity of the surface of the radiator panels.

The mass of the heat rejection system is largely driven by the area of the radiator panels. Equation 51 is used to calculate this, given the input heat temperature T:

$$A = \frac{P_{motors} \frac{1 - \epsilon_{motor}}{\epsilon_{motor}}}{\varepsilon \sigma_{SB} (T^4 - T_{sink}^4) - \alpha f_S G_{SC}} \; . \tag{52}$$

As noted earlier, $P_{motors} = 4$ MW, $\epsilon_{motor} = 0.96$ and $f_S = 0.33$. The sink temperature can be taken as the ambient temperature of near-Earth space, $T_{sink} = 283$ K.

$T = 400$ K represents the upper end of the operating range of water-titanium heat rejection systems (Maxwell et al. 2014). Radiator panels can be painted with magnesium oxide white, which has $\varepsilon = 0.9$ and $\alpha = 0.09$ (Henninger 1984). With these values, the resulting area required to dissipate the main sources of heat is thus $A = 178$ m^2

Titanium-water systems have typical areal densities of about 1.25 kg/m^2 (Maxwell et al. 2014), leading to a system mass of 222 kg.

2.2.4 Tether

Material

The primary tether candidate at this time is graphene super-laminate (GSL). Layered boron-nitride or carbon nanotubes are alternative candidates having different advantages and disadvantages. Tests of single-layer graphene demonstrate sufficiently high tensile strength (130 GPa) and low density (2260 kg/m^3) to support a space elevator tether and a number of climbers. Because this material is still under development, many of its properties are unknown. For example, it is very likely that multi-layer graphene, due to its layered structure, will not be isotropic. That is, the propagation of applied stresses through the material will depend on their direction. In the following discussion, however, isotropy is assumed simply because there are not enough data to define the anisotropic parameters. Details of the tether materials are discussed in Chapter 3. Known or estimated properties, with citations, can be found in the data reference in Appendix D.

Tether Stress Near the Interface

Equation 28 gives the applied stresses in the tether near the interface with the wheel. Using Equation 32, these become

$$\sigma_t = \frac{2F_t}{A_t} \, , \sigma_c = P_{max} \, , \tau = \frac{2F_t}{A_c} \, . \tag{53}$$

σ_t decreases with altitude because F_t decreases and the cross section A_t increases with altitude up to GEO. Because maximum stress is of interest, this value can be taken at $r = R_E$,

$$\sigma_t \;=\; \frac{2F_t}{A_t} \;=\; \frac{2[g(R_E) - c(R_E)][m_c/(2N)]}{m_c[g(R_E) - c(R_E)]/\sigma_0} \;=\; \frac{\sigma_0}{N} \, , \tag{54}$$

where σ_0 is the equilibrium stress, constant throughout the tether, m_c is the climber mass and N_{wp} is the number of wheel pairs. As in Equation 34, τ remains constant,

$$\tau = 2\mu P_{max} \, . \tag{55}$$

As in Equations 29, 30 and 31, the Mohr combined stresses are

$$\sigma_1 = \frac{\sigma_0/N + P_{max}}{2} + \sqrt{\left(\frac{\sigma_0/N - P_{max}}{2}\right)^2 + 4\mu^2 P_{max}^2} < \sigma_{ty} \ , \tag{56}$$

$$\sigma_2 = \frac{\sigma_0/N + P_{max}}{2} - \sqrt{\left(\frac{\sigma_0/N - P_{max}}{2}\right)^2 + 4\mu^2 P_{max}^2} < \sigma_{cy} \ , \tag{57}$$

$$\tau = \sqrt{\left(\frac{\sigma_0/N - P_{max}}{2}\right)^2 + 4\mu^2 P_{max}^2} < \tau_y \ . \tag{58}$$

The stress σ_0 is determined by the tensile strength of the tether. From Table 5 in Appendix D, the graphene tensile strength is 130 GPa. To get maximum operational values, this must be reduced by a safety factor. Using the NASA standard for spacecraft (Zipay et al. 2015), a factor of 1.4 is applied to get $\sigma_0 = 130/1.4 = 92.9$ GPa. Table 3 shows the principal stresses using $\mu = 0.1$, $P_{max} = 0.4174$ GPa, $\sigma_0 = 92.9$ GPa and $N = 5$, compared to the material strengths in Table 5 of Appendix D.

Stress	Value (GPa)	Yield Strength (GPa)	Strength citation
σ_1	18.58	$\sigma_{ty} = 130$	Lee et al. (2008)
σ_2	0.417	$\sigma_{cy} = 14$	Yoshiasa et al. (2003)
τ	9.08	$\tau_y = 0.14$	Liu et al. (2012)

Table 3: Combined Stresses in GSL Tether

The large tensile strength dominates, so that the total tensile and total compressive stresses are very little changed from the applied stress values, and are well below the material yield strengths. The combined shear stress, however, is about 65 times that of the measured shear strength of SCG. The shear strength of multi-layer graphene must be increased at least 100 times for it to be used as the tether material. Means of accomplishing this are discussed in Chapter 3.

2.2.5 Scaling Laws

The space elevator tether is linearly scalable, that is, its mass is proportional to that of the climber. If the desired climber mass doubles, so must the mass of the tether. It is important to know whether or not the mass of the climber scales in a similar fashion or if it is subject to the more severe square-cube scaling of objects in terrestrial gravity. Knowing the scaling laws of the climber allows its optimal size and mass to be found.

The total climber mass, including payload, able to climb the elevator depends on the traction force that can be generated. Of course, to achieve the same traction force with a lower climber mass improves the payload fraction. The traction force in turn depends on a combination of the friction force and motor torque that can be generated. It is assumed that the climber contact with the tether exploits the maximum permitted pressure between tether and climber wheels. The following relations show how the traction force scales with the above parameters.

Number of wheel sets: each pair of wheels added increases the length and mass of the climber in a linear, discrete way. This can be formalized as

$$m_c = N_{wp} m_{wp} + m_{overhead}, \tag{59}$$

where m_{wp} consists of all the mass associated with a single pair of wheels that compresses the tether. This includes the drive motors, axles, couplings, wheels, brakes and compression jacks, as well as the parts of the climber chassis, electrical bus and cooling system that are proportional to length. $m_{overhead}$ accounts for all other climber components that do not increase in mass with the number of wheel pairs. Relative to the total climber mass, this is probably small if $N_{wp} > 3$.

Wheel width : the width of the wheel should match the width of the tether in order to maximize the area of the contact patch between wheel and tether. The wheel design will include hollows and other mass optimizations, but its mass will still depend more or less linearly on the width. The wheel width does not scale with tether mass unless the tether mass is increased by increasing its width.

Wheel radius : the radius is chosen based on motor torque, motor speed and travel time to GEO. It affects the contact patch size, but only as the square root of the radius, according to a Hertzian contact model (Equation 23). Hence this parameter does not scale with the tether mass or the number of wheel pairs. The wheel mass is roughly proportional to its width and the square of its radius, and thus subject to square-cube scaling.

Motor torque : motor torque is proportional to the volume of the rotor, and also depends linearly on some material properties that determine magnetic flux and currents. The mass of the combined wheel/motor structure is then also proportional to its volume and subject to square-cube scaling.

Overall Scaling : The climber mass thus appears to scale in a hybrid manner: each wheel pair is subject to square-cube scaling, while the total mass scales linearly with the number of wheel pairs. This linearity can be maintained if the following climber assembly procedure is followed. As each wheel pair, with its apportioned payload, is assembled, it is run a little way up the tether where it clamps on. The tether now bears

its weight. Subsequent wheel pairs are added in the same way, each independently supported by the tether, rather than by a unified climber frame. Square-cube scaling is thus avoided. Eventually all the wheel-pairs will be connected by a frame, but only to provide rigidity and not to support weight.

Built in this way, there is no limit to the mass of the climber as long as the tether can be built big enough. There are two caveats to this. The wheel pair still scales by square-cube which means that its mass will be structurally limited. The total mass of the climber is not limited in this way, but the means of constructing the climber is, so that the jigs, scaffolding and so on are subject to square-cube. These will eventually limit the total mass of the climber, although not as severely as strict square-cube.

2.3 Summary

Local climbability can be defined by the following conditions.

- **Friction:** the coefficient of friction between the wheel and tether surfaces must exceed a practical minimum.

$$\mu > \mu_{min} \ .$$

- **Interface Temperature:** the temperature at the interface must be less than the maximum service temperature of either material.

$$T_{interface} < min(T_{maxW}, T_{maxT}) \ .$$

where T_{maxW} and T_{maxT} are the maximum temperatures for the wheel and tether, respectively.

- **Combined Stress:** combined stresses depend on interface pressure, contact patch area and differential tether tension, and may not exceed maximum operating values.

$$\sigma_{ttot} = \frac{\sigma_t + \sigma_c}{2} + \sqrt{\left(\frac{\sigma_t - \sigma_c}{2}\right)^2 + \tau^2} \ < \ \sigma_{tmax} \ ,$$

$$\sigma_{ctot} = \frac{\sigma_t + \sigma_c}{2} - \sqrt{\left(\frac{\sigma_t - \sigma_c}{2}\right)^2 + \tau^2} \ < \ \sigma_{cmax} \ ,$$

$$\tau_{tot} = \sqrt{\left(\frac{\sigma_t - \sigma_c}{2}\right)^2 + \tau^2} \ < \ \tau_{max} \ ,$$

where the applied tensional stress is

$$\sigma_t = \begin{cases} \Delta T / A_t & for\ tether \\ 0 & for\ wheels \end{cases} \ ,$$

the applied compressive stress is

$$\sigma_c = P_{max}$$

and the applied shear is

$$\tau = \begin{cases} \Delta T/A_c & for\ tether \\ F_t/A_c & for\ wheels \end{cases} .$$

- **Lift:** the difference in tether tension induced by tractive force must exceed the difference of gravity and centrifugal force.

$$N_{wp}\Delta T \ = \ 2N_{wp}F_t \ > \ m_c[g(r) - c(r)] \ , \tag{60}$$

where N_{wp} is the number of wheel pairs, $2N_{wp}F_t$ is the total tractive force due to all wheels and $N_{wp}\Delta T$ is the total difference in tension above and below the climber. m_c is the climber mass and $g(r)$ and $c(r)$ are the gravitational and centrifugal accelerations.

- **Motor Torque:** total motor torque must exceed the product of initial tractive force and climber wheel radius.

$$M_{total} > F_t R_W, \tag{61}$$

where R_W is the wheel radius and $M_{total} = 2N_{wp} * M_m$. N_{wp} is the number of sets of opposing wheels comprising the climber and M_m is the maximum operating torque of the motor driving each wheel.

- **Wheel Radius:** the wheel radius must be large enough to avoid high cycle stress failure and smaller than the motor torque per tractive force.

$$\frac{M_{total}}{F_t} > R_W > \frac{F_{cav}}{\pi W_W p_F^2 (1-\nu^2)/E} \ , \tag{62}$$

where F_{cav} is the applied compressive force averaged over the trip to GEO and W_W is the width of the wheel. The remaining parameters are properties of the wheel material, with p_F the fatigue pressure as a function of the number of wheel rotations, E the Young's modulus and ν the Poisson's ratio.

- **Cooling:** solar and waste heat must be rejected at a rate sufficient to keep ambient temperatures within operating ranges for climber equipment.

$$P_{rejected} = \epsilon\sigma_{SB}(T^4 - T_{sink}^4)A \ > \ P_{waste} + P_{sol}\alpha A, \tag{63}$$

where P_{waste} is the heat generated mostly by motor inefficiency, P_{sol} is the solar radiation incident on the radiator panels and σ_{SB} is the Stefan-Boltzmann constant. The radiator panels have an emissivity ϵ, an absorptivity α and a total area A. T is the input temperature of the heat to be rejected and T_{sink} is the temperature of the climber environment.

3 Tether Characteristics

3.1 Purpose and Status

The space elevator tether has two functions: to support itself and to raise payload. The sum of climber masses will be small compared to the total tether mass, but the stresses their drives exert on the tether will be significant. As yet, no material of sufficient strength exists in large enough quantities to serve these functions, but the prognosis for mass production of such materials in the near future is good.

Candidate materials for the tether are carbon nanotubes (CNT), graphene superlaminate (GSL) and hexagonal boron nitride (hBN). Laboratory samples of each of these have been produced with sufficient specific strength (Wright et al. 2021), but kilometer-scale lengths will be required so that they can be spliced together to make a 100,000 km long tether.

Until recently, CNTs appeared to be the prime candidate for the tether material, however, progress in making longer lengths seems to have stalled. Proposed manufacturing processes for the 2D materials, GSL and hBN, seem to have no limits on the lengths or speeds at which they can be produced. This, and the fact that 2D materials seem geometrically best suited to the construction of an essentially 2D tether, make GSL or hBN the preferred options.

3.2 Materials

There are three candidate materials with the required strength. These materials are described as single crystal. Crystal in this context refers to an uninterrupted repeating pattern at the molecular scale and is a single molecule of material that will produce the maximum strength possible. Where defects and vacancies are present the material is described as polycrystalline, and the material has a lesser strength. The molecular structures of single crystal carbon nanotubes, single crystal graphene and single crystal hexagonal boron nitride (hBN) are shown in Figure 4.

These materials can be classified as one dimensional (1D) or two dimensional (2D). Dimensions in this context refers to the number of spatial dimensions in which a molecule can grow while still retaining the same characteristics. For example, carbon nanotubes can grow from either end of the tube, provided it is not capped, and remain the same material. If extra carbon atoms were to be added to the sides of the tube this would change the nature of the material. Similarly, graphene and hBN can only grow in the x and y dimensions with carbon atoms attached with covalent bonds.

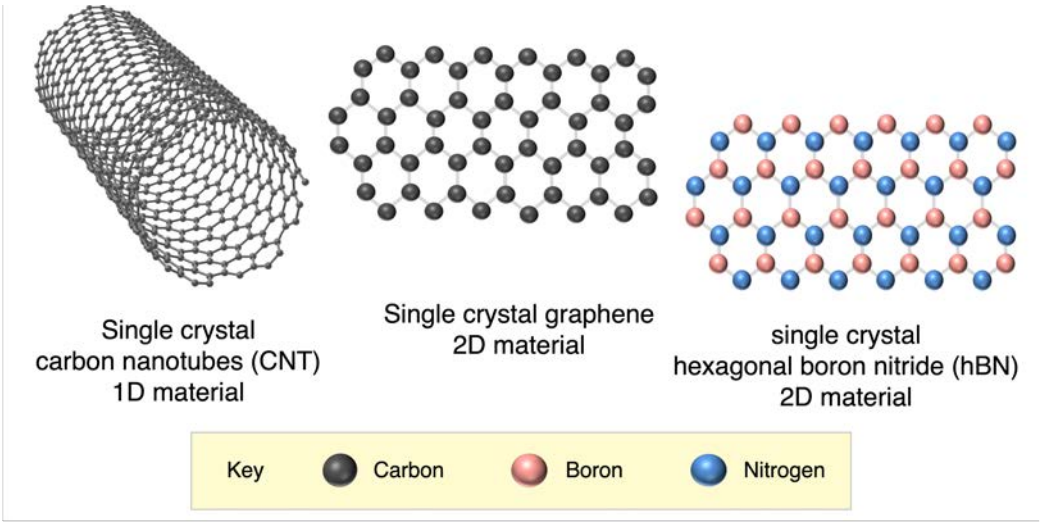

Figure 4: Molecular structure of candidate tether materials

3.2.1 Graphene super-laminate

Multi-layered single crystal graphene consists of layers of single crystal graphene stacked in such a way as to maximize the Van der Waals forces between them. To simplify the language, the term graphene super-laminate (GSL) is used here to mean a Van der Waals homostructure of multi-layered single-crystal large-area graphene.

Each layer is a single molecule of sp2 hybridized carbon 0.335 nm thick (Class for Physics of the Royal Swedish Academy of Sciences 2010). To create a tether of sufficient strength, up to about 12,000 such molecules will need to be laid on top of one another. This thickness assumes a 20 t climber departing Earth each day on a tether up to one meter in width. To increase the mass raised, either the tether thickness or width must be increased. The most stable, and strongest, of the possible layering orientations is called AB stacking. A stick-and-ball model of this configuration is shown in Figure 9. Graphene layers in AB stacking will not slide by one another as easily as they do in alternative configurations such as AA stacked or randomly stacked (turbostratic) graphene (Latychevskaia et al. 2019).

In addition to its high tensile strength (130 GPa) (Lee et al. 2008) and low density (2260 kg/m3) (MaterialProperties 2022), GSL offers many other useful properties including high electrical and heat conductivity, high current density, and good resistance to chemical attack by free radicals. Of direct relevance to the climbability condition, graphene can sustain very high compressive forces, up to 14 GPa (Yoshiasa et al. 2003). This is much higher than the climber wheels will exert.

Graphene, however, is rather slippery, with a recently measured coefficient of friction of 0.1 (Dwivedi et al. 2021) (Table 5). This value is on the low side for a pinched-wheel climber design and modifications to the surface of a GSL tether may eventually be required (Wright et al. 2021). The resistance of GSL to shear forces

is also on the low side with a shear modulus between 0.19 and 0.49 GPa (Qu et al. 2019).

3.2.2 Hexagonal Boron Nitride

Hexagonal boron nitride (hBN) is another 2-D material in which boron and nitrogen atoms are arranged in a hexagonal pattern. Figure 4 shows the structure. It has a lower strength, 100.5 GPa (Paul et al. 2017), than GSL, but this is somewhat compensated by a lower density (2.0 to 2.2 g/cm^3 (Lipp et al. 1989)) and higher interlayer shear strength (3.07 to 4.31 GPa (Qu et al. 2019)). hBN has a relatively high thermal conductivity, 751 W/m/K (Cai et al. 2019), but unlike GSL it is a good electrical insulator. It is in many ways complementary to GSL; where more friction or insulation is needed, hBN could be used, having a coefficient of friction between 0.23 and 0.27 (Koskilinna et al. 2006) (Table 5), and where more strength or electrical conductivity is needed GSL could be used.

3.2.3 Carbon Nanotubes

Although not examined in this study, carbon nanotubes (CNTs) were the first of the strong materials to be proposed for constructing the space elevator tether. It is useful to compare their properties to those of GSL and hBN. CNTs come in many varieties depending on the pattern of the carbon atoms and the number of atomic layers (walls). For simplicity only single-walled carbon nanotubes (SWCNT) are discussed here. SWCNTs have the same strength as GSL (Table 5), but a lower density than either GSL or hBN, which is a distinct advantage. The coefficient of friction is similar to that of hBN, so it is easier to grip. SWCNTs have a very good electrical conductivity, but not as high as GSL. Thermal conductivity appears to be better than that for GSL.

In the laboratory, SWCNTs and single crystal graphene have been produced with similar lengths (0.5 m), so it would appear that they are both good candidates for the tether material. GSL was chosen for this study because of the greater likelihood that it could be produced in longer lengths, at higher rates and at an earlier date.

3.3 Materials Manufacturing

To achieve a focus on the material of choice, the state of the art of manufacture of these materials was reviewed.

3.3.1 Carbon nanotubes

Carbon nanotubes are manufactured industrially. OCSiAl, a Luxembourg based manufacturer has a carbon nanotube production capacity with its Tuball subsidiary company that is stated to be 90 t of CNTs per year. The company says this accounts for over 97% of the global graphene nanotube market. However, the carbon nanotubes

it produces are just 5 μm in length and seem to be used as powdered additives to enhance the performance of other materials (Tuball 2022).

Longer CNTs have only been made in the laboratory. The longest single-molecule carbon nanotube made so far is 0.5 m in 2013 (Zhang et al. 2013). Since then no further improvements in length have been reported. The state of the art of carbon nanotube manufacture seems to be to make nanotube forests with a length of 0.14 m and probably polycrystalline (Sugime et al. 2021).

3.3.2 Hexagonal Boron Nitride

Large-area sheet hBN is produced industrially. The most prominent manufacturer is Grolltex Technologies in California, USA. The company has developed a batch process that manufactures hBN by a CVD method on metal foil and can transfer the material to other substrates. However, this is restricted to 200 mm diameter wafers for the semiconductor industry (Grolltex 2022).

3.3.3 Large-area Sheet Graphene

The industrial state of the art making large area graphene is capable of manufacturing polycrystalline material. The industrial manufacture of single crystal has yet to be attained. However, progress has been astonishing, and several industrial companies have developed scaleable processes making polycrystalline material.

General Graphene Inc., based in the USA, has announced that its Gen 3.0 roll-to-roll graphene production line has been commissioned and can make 100,000 m^2 of graphene on copper foil per year (Nixon 2022). Figure 5 shows the production line.

General Graphene has also demonstrated the ability to separate the graphene from the copper foil and create multilayered graphene samples on a transparent plastic film substrate. The company provided samples to ISEC as shown in Figure 6.

In South Korea, two companies have created industrial-scale graphene manufacturing plants. LG Corporation has developed a roll-to-roll production method that can make graphene on copper foil at speeds of up to one meter per minute and lengths of up to one kilometer (Nixon 2022). Charmgraphene has gone further and can produce graphene on copper foil at speeds of two meters per minute and lengths of one kilometer (Nixon 2022). The company has also automated the separation of graphene from the copper foil and transfer to other substrates. Figure 7 shows the publicly released images of their production lines.

Charmgraphene has also demonstrated the ability to separate graphene from the copper foil surface. They can create free-standing multi-layered graphene (Nixon 2021). Free-standing means there is no substrate support; the atomic layers of graphene support themselves. Figure 8 shows a sample of 20 to 30 layers of free-standing graphene in a frame. The multi-layered graphene is 110 mm wide by 144 mm in length.

Figure 5: General Graphene Inc. roll-to-roll graphene production line. Image credit: General Graphene.

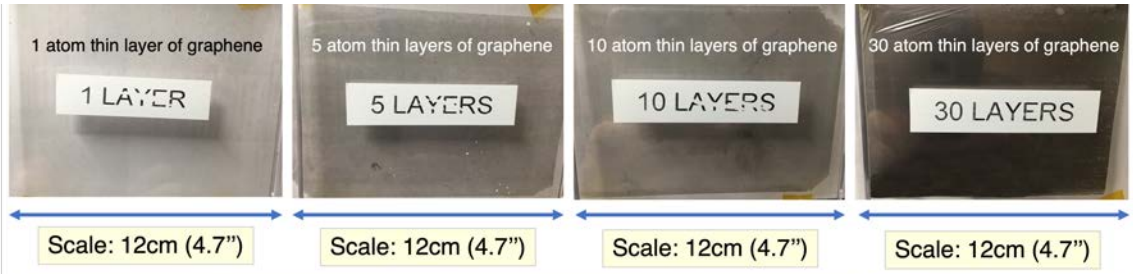

Figure 6: Samples of multiple graphene layers made for ISEC. This is not tether quality graphene and is meant only to show the pace of manufacturing development. Image credit: Michael Fitzgerald (International Space Elevator Consortium).

While industrial manufacturers are making polycrystalline graphene, work continues on making single crystal graphene in the laboratory. The longest sheet of single crystal graphene was made at a scale of 500 mm by 50 mm at Peking University, Beijing, China in 2017 (Xu et al. 2017). The largest area of single crystal graphene to date has been reported by researchers from Oak Ridge National Laboratory, who demonstrated the manufacture of single crystals of 300 mm by 300 mm area (Vlassiouk et al. 2018).

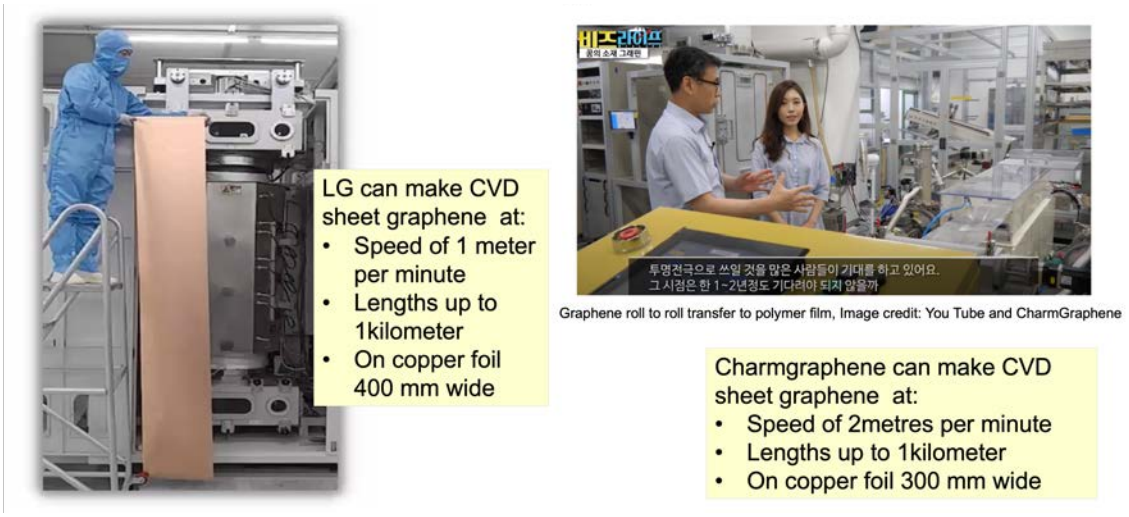
LG can make CVD sheet graphene at:
• Speed of 1 meter per minute
• Lengths up to 1kilometer
• On copper foil 400 mm wide
투명전극으로 쓰일 것을 많은 사람들이 기대를 하고 있어요.
그 시점은 한 1~2년정도 기다려야 되지 않을까
Graphene roll to roll transfer to polymer film, Image credit: You Tube and CharmGraphene
Charmgraphene can make CVD sheet graphene at:
• Speed of 2metres per minute
• Lengths up to 1kilometer
• On copper foil 300 mm wide

Figure 7: CVD production lines at LG and CharmGraphene. Image credits: LG and CharmGraphene.

3.3.4 Manufacturing Summary

To make the material for the space elevator tether requires manufacturing on very large scales and speeds. Carbon nanotubes can be made at sub-meter lengths, very slowly. Hexagonal boron nitride can be made industrially but only at a scale of 200 mm in diameter for electrics applications.

Graphene on the other hand can already be made at lengths of one kilometer and a speed of two meters per minute. None of these materials can be made at tether quality yet, however the trajectory clearly favors graphene as the industrial material of choice, and this is why graphene was the focus of attention for this study.

3.4 Design Considerations

Assuming that the basic tether material will be made available, the next step will be to determine how it should be structured. The tether will not consist of a monolithic and isotropic block of material, but rather of laminations of thin layers or weavings of thin tubes spliced together. The final design will depend on the basic material properties, the stresses and environmental conditions to which the materials will be subjected and the details of the tether assembly process.

3.4.1 Requirements

Stresses

The requirements for the tether material in the vicinity of the climber can be taken from the combined stresses listed in Table 3. Implicit in the climbability requirements was that the tether could sustain a tension of $\sigma_{TS} = 130/1.4 = 92.9$ GPa, where 1.4 is

Figure 8: CharmGraphene multi-layer free-standing polycrystalline graphene. Image credit: CharmGraphene.

the safety factor. Thus it was assumed that the applied tensile stress was never more than 92.9 GPa. The resulting combined tensile stress per wheel pair was 18.58 GPa, well below the yield strength.

Resistance to shear forces is a critical requirement; the downward force due to climber mass on the surface of the tether must not exceed the force holding the layers together. The maximum combined shear force at the interface was found to be 9.08 GPa, 65 times larger than the measured shear strength of 0.14 GPa.

The compression of the tether due to the wheels must not exceed the compressive strength of the tether. The combined compressive stress was found to be 0.417 GPa, well below the quoted yield strength of 14 GPa. Comparing this to the 0.88 GPa compressive strength of titanium wheels (Table 1), it is the wheels and not the tether that set the maximum allowed compression at around 0.9 GPa.

For the tether material in the immediate region of the climber, there are no requirements concerning bending or torsional stresses. Having chosen not to use a

capstan drive, the tether will not be subject to bending moments. The climber frame which holds the wheel pairs in place will prevent any significant torsion.

Environmental Conditions

The tether will be immersed in a variety of environments including atmosphere, vacuum, electromagnetic fields, radiation fields and thermal gradients.

Corrosive chemicals in the Earth's atmosphere will degrade the tether. Salt water and water vapor at low altitudes and oxygen radicals in the higher altitudes will react with the tether materials and decrease their strength. While a single layer of graphene has every one of its atoms exposed to its environment, the great bulk of the atoms in GSL will be insulated due to its many tightly packed layers. Only the surface layers and edges will be vulnerable to chemical reactions. The same is likely to be true for hBN. In both cases, edge reactivity could be suppressed by folding or rolling. A single CNT exposes all of its atoms as well. Reactivity could be reduced by braiding the CNTs, but this is unlikely to remove as many atoms from environmental contact as in the case of GSL.

The large electrical conductivities of GSL and CNTs mean that significant currents and forces may be induced in the tether by Earth's electromagnetic fields. These can result in displacements of thousands of kilometers at the apex when extreme solar storms arise, but usually such oscillations are small and certainly negligible in the immediate region of the climber. This issue could even be eliminated by building a tether partially or entirely with hBN, which is an insulator. There are, then, no particular electrical requirements of the materials in this respect.

Thermal gradients are certain to occur along the tether length and particularly in the region of the climber where friction with the wheels will induce heat at the contact areas. High thermal conductivity in the tether will mitigate this problem.

The radiation environment will be severe. Hard ultraviolet and particle irradiation is ubiquitous in space and the upper atmosphere and the tether materials must be resistant to it. The tensile strength of CNT yarns was reduced by about 50% after a long exposure to space radiation (Ishikawa et al. 2019). GSL may perform better in such circumstances since the carbon atoms in laminations would be packed more closely together than in CNT braids, thus retaining more strength when atomic bonds are destroyed.

Assembly Conditions

The basic material will be manufactured on Earth in the form of sheets of GSL or hBN, or fabrics of woven CNTs. The lamination of GSL and hBN layers into thicker sheets requires a good vacuum environment in order to avoid intercalation. This argues for the lamination to be done in space, requiring an assembly satellite in GEO. Rolls of the basic material must be transported to space by rocket and therefore must fit into available cargo holds. The proposed tether width poses no problem in this regard and the thinness of each layer means that a very large number of sheets

would fit into a single roll of manageable mass.

3.4.2 Lamination

The most straightforward option for building a tether out of 2-D materials is lamination. Given their nanometer-scale thickness, thousands of layers will be required to construct a practical tether.

Natural Bonding

Layers of single crystal graphene will naturally adhere to one another by Van der Waals bonding to form GSL. The bonding arrangement with the smallest distance between layers is called AB stacking which is illustrated in Figure 9. The Van der Waals forces are strongest in this arrangement and would provide the most resistance to shear stress.

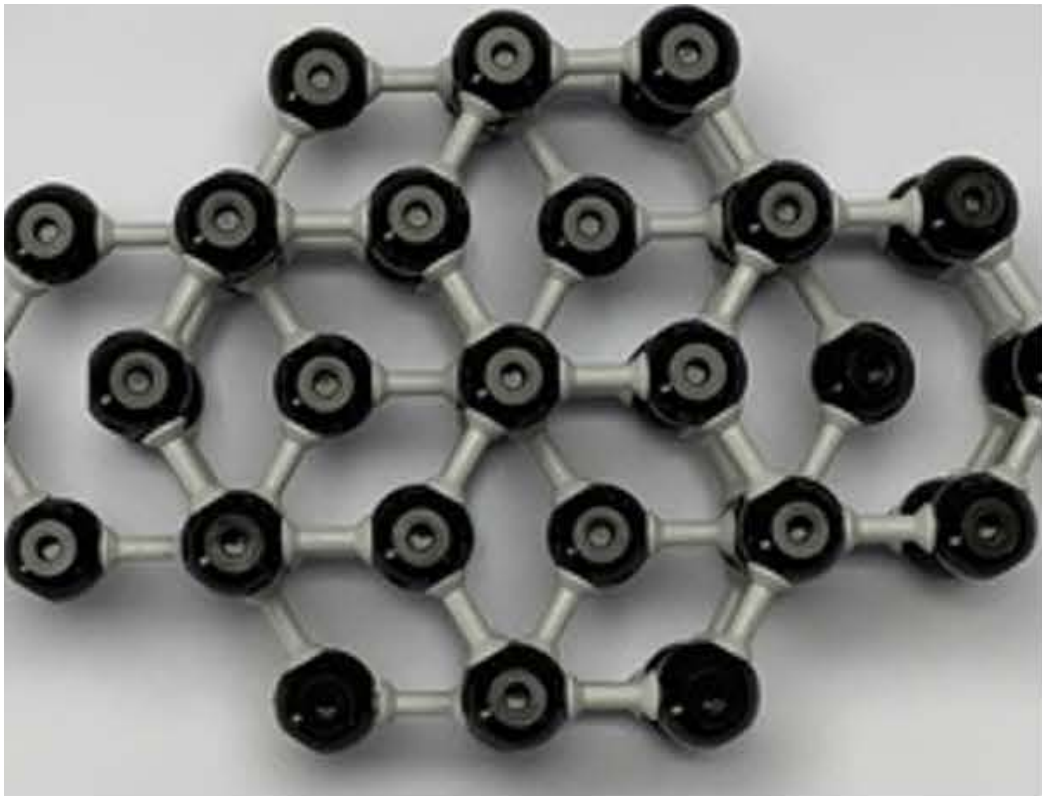

Figure 9: View looking down on a model of AB stacked multi-layer graphene. Each alternate carbon atom in a six-atom ring is located directly above the center of a ring directly below it.

Spot Welding

If the Van der Waals forces are not strong enough, large shear forces on the surface of the tether material will not be sufficiently distributed into the bulk and de-lamination will occur. According to Table 3 the shear strength of GSL is 0.14 GPa, about 65 times too weak to support the climber. Thus, another bonding option must be considered.

In GSL, the carbon atoms are connected by hybrid sp2 bonds. The remaining π orbitals are unbonded and oriented perpendicular to the plane of the graphene layer. When two such layers are pressed together, the sp2 bonds and π orbitals create sp3 bonds between the layers, as shown in Figure 10. The sp3 hybrid bond is the one found in diamond and accounts for its strength. The pressure at which this type of bonding occurs is thought to be about 23 GPa (Yoshiasa et al. 2003). Ultrafast lasers can achieve such pressures and have been used to synthesize the diamond phase (sp3 bonds) from the layered phase (sp2 bonds) (Maia et al. 2015). It has also been shown recently that when several atoms take part in this bonding, the results are irreversible (Niu et al. 2022). Perhaps this process could be applied on an industrial scale to produce a material resistant to the shear stresses expected in the space elevator tether.

Figure 10: Stick-and-ball model of "spot-welded" multilayer graphene. The sp3 hybrid bonds are shown in the center, between two layers of graphene.

Increasing Friction

Research for this study discovered that reliable figures for friction in 2D materials are not easily found and that the literature contains a wide range of values from 0.03

to 0.1 (Shin et al. 2011, Dwivedi et al. 2021) (Table 5). These values are obtained using atomic force microscopy in which a diamond tip is dragged over the sample surface. The view of the study group was that fresh work needs to be conducted using a metal coated tip against the graphene surface. Larger scale tests are preferred when macroscopic samples can be obtained. This would replicate the conditions of a climber wheel against a graphene tether more reliably. A coefficient of friction value of 0.1 was chosen for this study as it was the most recently measured.

However the lamination is done, the surface of the tether is likely to be rather smooth, with a coefficient of friction of about 0.1. This is a manageable number in mechanical engineering, but on the edge of practicality for friction drives in space elevator climbers.

Two methods may be able to raise the effective coefficient of friction. One is to introduce hydrogen onto the surface of the GSL. Measurements show that this increases the coefficient of friction to about 0.13 (Wang et al. 2013). Another method would be to use hBN as an outer layer bonded to a tether bulk consisting of GSL; GSL and hBN naturally bond to one another forming a Van der Waals heterostructure (Yankowitz et al. 2019). According to Table 5, hBN has a coefficient of friction of about 0.25, which would provide much more holding force between the climber wheels and tether. Other methods involve making the surface rougher by the creation of diamond studs at regular intervals using high pressure, and wrinkling or creping the surface.

3.4.3 Braiding

Another option is to construct the tether using CNTs or rolled-up GSL or hBN layers. These tubular structures would be braided into threads and woven to create the tether fabric. This method has two advantages. Because the tubular molecular structure has no edges, it is highly resistant to attack by oxygen radicals and other chemicals in the atmosphere. Also, sheets produced by braiding and weaving would create a rougher surface with a much higher coefficient of friction for the climber wheels. The main disadvantage is that a braid is always weaker than its component threads.

3.5 Molecular Modeling

The methods listed above for increasing shear strength and the coefficient of friction are conjecture based on some recent measurements. They have to date not been attempted in any manufacturing process. Absent this, it is useful to see if computer modeling can shed some light on the possibility of these processes. Molecular modeling can be used to see how macro-molecules interact with each other and with their environments.

The key requirement of such modeling is the prediction of macroscopic material properties and the formation and propagation of defects, based on the electromagnetic interactions of individual molecules. The list of properties to be modeled and predicted include the coefficient of friction between graphene sheets and other materials, and the multi-axial tensile, shear and compression strengths of single and multiple graphene layers. Also to be modeled are the formation of defects and their propagation, the adsorption of gasses, the effects of pressure and temperature and the effects of the various stacking configurations of graphene sheets.

Two calculations would be of immediate interest for the GSL manufacturing process: calculation of the adsorption of hydrogen onto graphene is one possible way to predict how the coefficient of friction of the modified material would vary with hydrogen concentration; the introduction of localized pressure at intervals along the length of a two-layer graphene structure would indicate whether or not sp2 bonds in the two sheets could be converted to sp3 bonds between sheets, thus allowing the "spot-welding" of layers.

It is also essential to understand how defects are formed and propagated under the various stresses that will be applied to the tether material. Knocking carbon atoms out of their hexagonal pattern and the introduction of irregularities that could show up during manufacturing need to be simulated as well as how these irregularities develop into strength-reducing tears in the material.

In principle, all of these calculations can be done, but the major challenge, and one reason that these calculations have not been done, is that large numbers of atoms must be included in the calculation space in order to make predictions of macroscopic parameters. This is likely to require advanced computational methods and supercomputers. Several approaches to this problem and the computer codes required are discussed in Chapter 6.

3.6 Proposed Tether Design

There are several candidates for the basic material from which a space elevator tether may be constructed. Based on requirements from climbability and climber design, and speculation about the internal structure of the tether, a preliminary tether design is presented here.

An essentially two-dimensional structure will consist in its bulk of approximately 12,000 layers of AB-stacked single crystal graphene with its shear strength augmented by periodic spot welding between the layers. Several layers of hexagonal boron nitride will be laminated on either face of the GSL ribbon in order to provide increased friction and radiation hardness. These layers will also be cross-linked to layers beneath them by spot welding. To prevent chemical reactions at the edges of the molecular layers, it may be possible to use much wider layers and fold them accordion style before binding them together.

An alternative geometry of woven braids of CNTs or GSL/hBN tubes would pro-

vide greater friction for the climber wheels and resistance to chemical attack, but would likely lack the necessary tensile strength for supporting itself.

4 Climber Design

4.1 Design Philosophy

Given the throughput values desired for the space elevator, the drive type of the space elevator climber (Appendix A) and the climbability conditions set out in Chapter 2, a reference conceptual design was developed for the climber. It was assumed that only existing technologies would be used in the design. This rather conservative assumption was made for two reasons: design is easier when speculation about component specifications is not required, and a design using off-the-shelf technologies serves as a useful starting point for extrapolations into future technologies. In the end, a climber design using current technology might not meet the physical or economic needs of a space elevator, but with rapidly advancing technologies in the material and propulsion arenas, it is likely that a design using near future technologies will meet these requirements.

It was first assumed that the study would concentrate only on climbing in vacuum, in order that complications due to atmosphere could be avoided in the design. Other types of climber or space elevator variations (Knapman et al. 2018, Knapman & Swan 2014, Robinson & Knapman 2022) might better deal with those issues. Such a simplification turned out not to be possible for the reference conceptual design performed here because many of the drive components, such as motors with fans for air cooling, are not vacuum compatible. Using commercially available parts means that these are used on Earth in atmosphere. Gearboxes and electronics for use in space are by nature custom designs. Climber operation in the atmosphere presents a different set of challenges from climbing in vacuum, but also some advantages, especially in thermal management. This section does not address the possibility of using different climber types or different configurations for travel over the space elevator as a whole, but presents many design methodologies that would be used for any climber.

This chapter shows how the design process proceeds iteratively, switching between the component and system levels as various requirements react against each other. The goal is to create a climber with as much of its mass budget devoted to payload as possible. For decades, people have hypothesized that the first commercially viable climber would mass 20 t, carry 13 t of payload and have a traction drive massing 7 t or less. Achieving a payload ratio of 65% is difficult and some technological advancements are suggested that will be necessary to approach that number.

4.2 Assumptions in the Conceptual Design

The conceptual design in this report assumes a number of features of the tether that supports the climber. The tether is assumed to be shaped like a ribbon made from any of the candidate materials that are strong enough to be used for a space

elevator. The ribbon was assumed to be 10 μm thick, and constant in thickness at every altitude. It was also assumed to be 0.31 m wide at the surface of the Earth and up to 1.55 m wide at the altitude of geosynchronous orbit. This difference in width is determined by the taper ratio of the tether, which in turn is determined by the specific strength of the tether material. These dimensions lead to some climber features, such as an axle long enough to accommodate a 1.55 m wide tether.

Some assumptions come from the requirements of the design stated earlier: the top velocity of the climber is 200 kph; the trip time to geosynchronous orbit is approximately one week; and the total mass of the climber is 20,000 kg.

An important assumption is that the coefficient of friction between the wheels and the tether is $\mu = 0.1$. Carbon nanotubes or graphene are known to have values larger than this, but previous studies have shown that the coefficient of friction must be at least 0.1 because this number drives most of the stresses in the components of the climber. Strategies to achieve this value and to improve on it were discussed in Chapter 3.

In this conceptual model, every wheel is driven by a motor. The design has a direct drive between between the wheel and motor, with no mechanical transmission such as a gearbox or torque converter. This is because an electric motor, as in some locomotives, has a wide useful speed range from zero to some maximum value. Any transmission would add mass, cost and complexity to the design, with a potential impact on durability and reliability.

4.3 Climber Components

4.3.1 Motors

A survey of commercially available electric motors indicates that light-weight motors such as those used in the electric aircraft industry are the best candidates to drive the axles. To drive the wheel/axle combination, the motor must produce a torque proportional to the volume of the motor rotor. The mass of the motor increases with the torque it must produce. Thus, the torque-to-mass ratio is important, as is the mass-to-power ratio. Plots of mass vs. power and mass vs. torque for various types of motors, shown in Figures 11 and 12, indicate which type has the lowest mass for the power and torque. magniX motors (magniX 2021), with the best mass vs. power performance, were chosen for the initial climber conceptual design. Figure 13 shows the magniX motor in an an aircraft application.

General Electric motors (GeneralElectric 2021) are typical industrial motors for applications that demand reliability and for which the mass of the motor is not a consideration in the design. They can be found in many industrial and mining environments. They are far too heavy for an aerospace application. In previous studies, there were no curves below that of the Empire motors in the mass vs. power curve. Companies like magniX, Emrax (Emrax 2021) and Magnomatics (Magnomatics 2021)

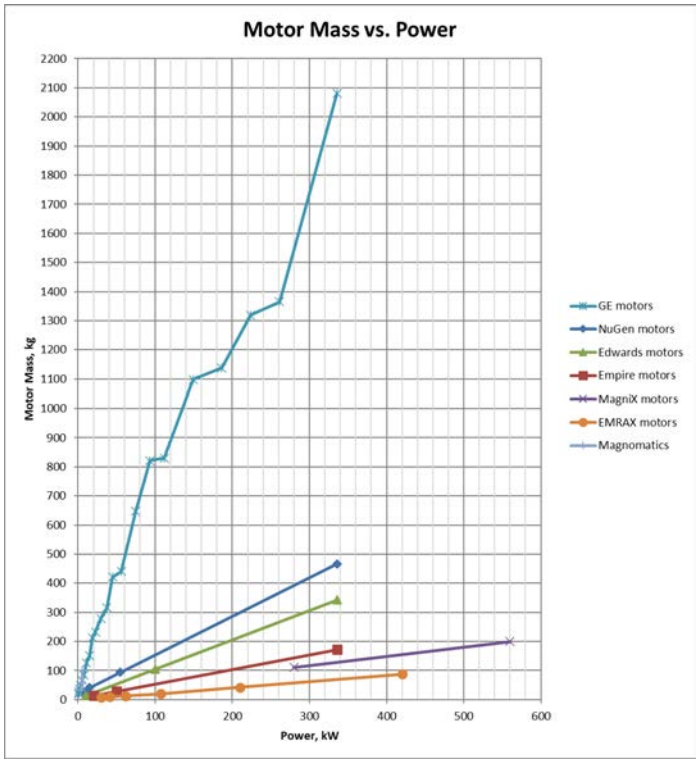

Figure 11: Motor mass vs. power for several types of electric motor

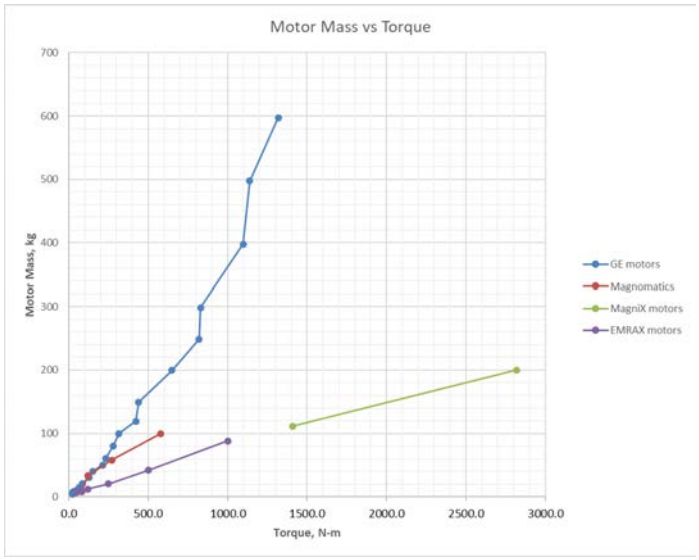

Figure 12: Motor mass vs. torque for several types of electric motor

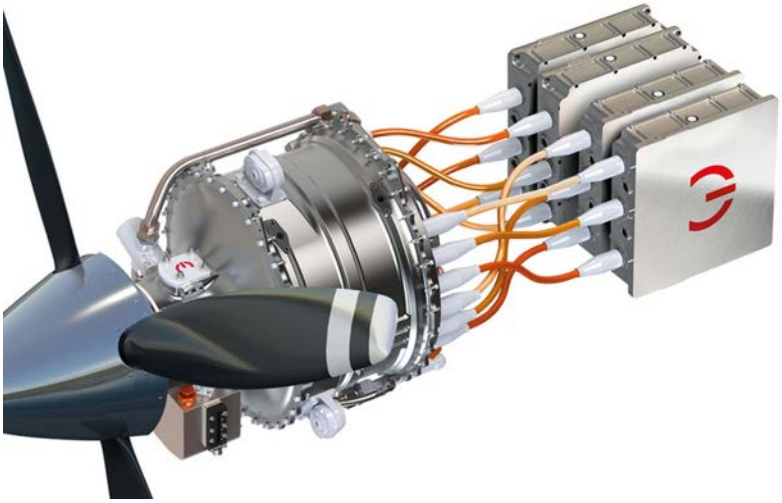

Figure 13: magniX motor in an aircraft application

have greatly extended the design space for light, powerful motors.

The specification from the magni650 motor used in the first climber design includes a continuous torque of 2,814 N-m, available from 0 to 1900 RPM. The mass of the motor is 200 kg. With these numbers, the wheels can be sized for the average velocity of 200 kph and a rotation rate of 1900 RPM.

4.3.2 Wheels, Axles and Bearings

The basic unit of the pinched-wheel climber design is a wheel mounted at the center of an axle. Each end of the axle passes through a sealed spherical roller bearing mounted on the climber chassis and one end is connected to a motor through a shaft coupling. Two of these units are paired and clamped together so that the wheels oppose one another and exert pressure on the tether between them. Figure 14 shows a single wheel pair and the orientation of the motors.

The wheels will be constructed of titanium alloy, Ti 6Al-4V, with as much mass as possible removed while maintaining strength. To achieve a speed of 200 kph at 1900 RPM, the wheel radius is 0.2794 m. Its width is 0.31 m where it comes in contact with the tether, and is determined by the width of the tether near the surface of the Earth. The wheels shown could be manufactured from multiple disks of titanium and welded together to form the full wheel.

The axle is assumed to made from aluminum, Al 6061-T6. The outside radius of the axle is 0.127 m. Dimensions of the axle were determined from the normal force necessary to create the friction force that supports the climber on the tether and gives it traction. The axle is hollowed out to reduce weight. As mentioned in Chapter 2, each wheel provides a contact area with the tether through which the friction force is applied. The total weight of the climber is supported by the output torque of the

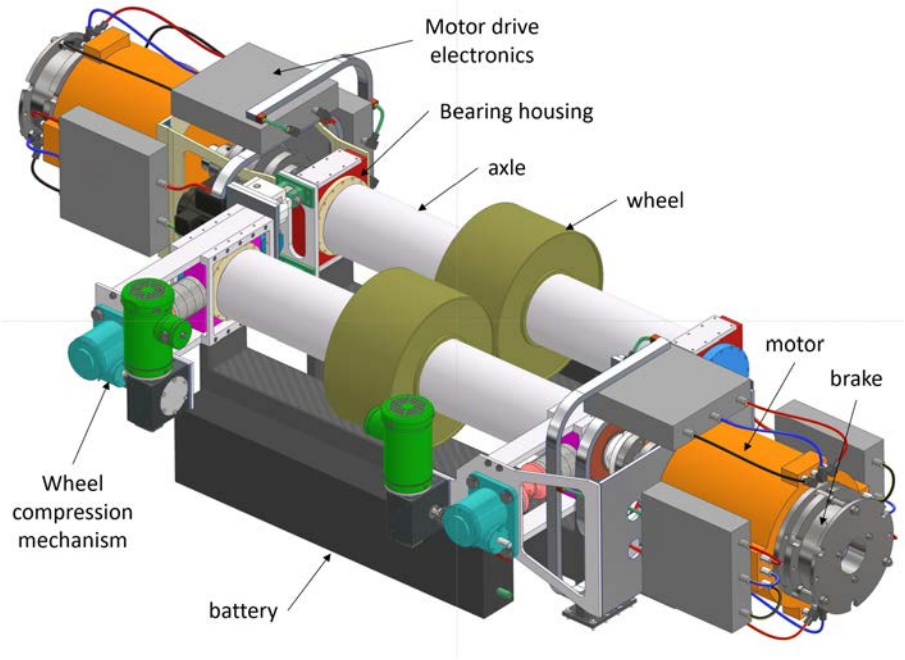

Figure 14: A wheel pair showing floating and fixed axles

motors, so the total number of motors is determined from the motor torque and the wheel size.

Rearranging Equation 61 and setting the motor torque to 2814 N-m, the equation becomes

$$\frac{m_c g R_W}{N_w} \leq M_{total} \ ,$$

where M_{total} is the motor torque and $N_w = 2N_{wheelsets}$ is the number of wheels. Knowing the mass of the climber, the acceleration due to gravity, the radius of the wheel, and the continuous output torque of the motor, N_w is also known:

$$N_w \geq m_c g R_W / 2814 \text{ N-m } = \ (20,000 \text{ kg})(9.8 \text{ m/s}^2)(0.2794 \text{ m})/2814 \text{ N-m} = 19.46.$$

There must be 20 wheels, or 10 wheel pairs, assuming the characteristics of the magni650 motor and the chosen wheel radius.

Figure 15 shows an early model of the ten-wheel-pair climber on the narrow tether near the surface of the Earth. This climber is missing many later enhancements. Most of the structure was assumed to be aluminum at this point in the design. The disks near the bottom and to the sides were placeholders for PV arrays to receive light from power beaming to power the climber.

Figure 16 shows why the axles are as long as they are, as the climber must be able to ascend to the altitude of GEO where the tether is much wider. The model shown has components within a few centimeters of the tether when the tether is at its widest. Further consideration must be given to the gap between the climber and the tether at the places where the tether is widest to allow for a steering margin. Given the long trip, the number of wheel rotations needed, and typical manufacturing tolerances of

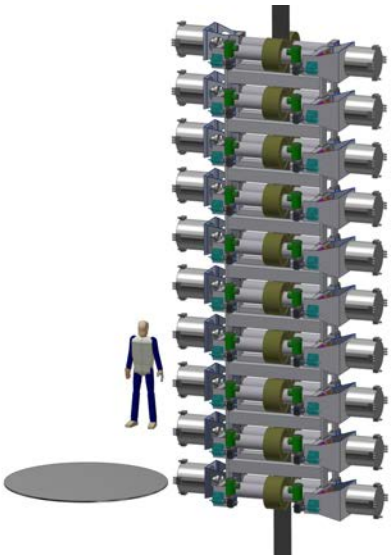

Figure 15: Early rendering of the solid model of the 10 wheel-pair climber at the narrow part of tether

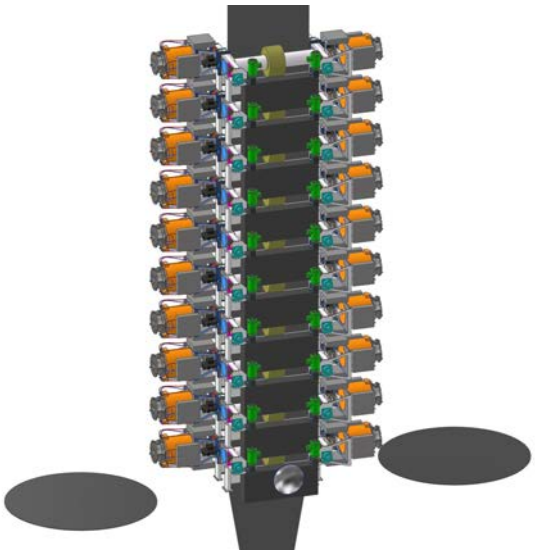

Figure 16: More developed model of the 10 wheel-pair climber at the wide portion of the tether

the wheels, the climber will drift and not remain centered on the tether. The climber must never intersect the tether as this will lead to damage to both tether and climber.

Figure 16 shows further development of the climber such as added subsystems for motor drive electronics, batteries, and an antenna for remote control of the climber. Development of each of the subsystems is critical to an accurate mass estimate of the traction drive.

Based on the Young's moduli of the wheel material and the tether material, almost all of the deformation required to create a contact patch will occur in the wheel. The pressure of one opposing wheel against the other will also cause the axle to flex perpendicular to its length. The bearings must accommodate the flex and be able to function in vacuum and in temperature extremes so that their lubrication remains liquid. Bearings must also be capable of running at speeds of up to 3000 rpm for extended periods of time. Figure 17 shows an example of a spherical roller bearing which can accommodate the bending of the axle by allowing the center axis of the inner race to rotate with respect to the axis of the outer race while rotating.

The force on the axles and the rotation speed cause two concerns: the lifetime of the bearings and metal fatigue in the wheels and axles will likely determine the operational lifetime of the climber; and frictional heat will be generated in each of these components which will need to be dissipated. The bearings require a lubrication recirculation system which pumps cooled oil into the bearing and carries away the warmed oil to the heat exchanger. Typical bearing seals to retain the lubrication are shown in Figure 18, but the fluid fittings and plumbing for the oil system have not been modeled yet. As can also be seen in that figure, not all of the fasteners that tie

Figure 17: Spherical roller bearing

the model together have been fully analyzed or inserted into the model. That is a detailed design analysis job that awaits future effort.

Another very important analysis that has not been performed rigorously yet is the bearing lifetime analysis. The spherical roller bearing selected has a dynamic load capacity of 195,000 lbs (867.4 kN) and a static load capacity of 230,000 lbs (1023.1 kN). It was selected to have a substantially higher rating than the applied load to ensure long life. From (Shigley & Mischke 1989), the life of a spherical roller bearing can be estimated from the following formula:

$$L = \left(\frac{C}{F}\right)^{\frac{10}{3}}, \tag{64}$$

where L is the life of the bearing in millions of cycles, C is the basic load rating in pounds (the dynamic load rating in this case) and F is the applied radial load (in pounds) on the bearing. The basic load rating C is determined by the manufacturer such that if the applied load equals C, the bearing life would be 1 million cycles. If C =195,000 lbs and F = 20,000 lbs (from the compression mechanism screw jacks, see next section), then the average life is 1980.1 million cycles. This is far more than is needed even to get to the end of the tether at 100,000 km altitude. However, the structure of the above equation shows that small changes in the applied load can lead to large changes in the expected life. If the applied load on the bearing were to double to F = 40,000 lbs, the expected lifetime would be reduced to 196.4 million cycles. An increase in bearing load of a factor of two leads to a 90 % reduction from the original

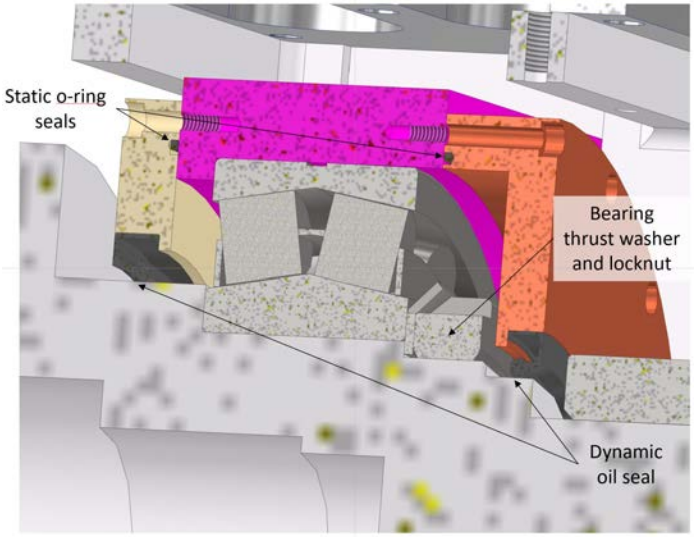

Figure 18: Cross section showing bearing seals: dark gray circles near top and dark gray areas near center

estimated lifetime. The numbers shown do not take into account additional lifetime modification factors from the confidence level to failure of the bearings. These results will become very relevant later in this document.

The preceding analysis was done for bearings used on Earth in atmosphere. Fortescue & Stark (1995) make some very useful and cautionary points about the difference between components and lubrication systems on Earth and in space. More work is necessary to make a space-worthy climber.

4.3.3 Wheel Compression Mechanism

A floating wheel module and a fixed wheel module must be pressed together in order for the wheels to exert pressure on the tether and develop traction. The clamping arrangement should allow for sufficient pressure on the tether and easy addition and removal of wheel modules to the climber during assembly. A section view of the clamping assembly through the vertical mid-plane of the compression mechanism screw jack axis is shown in Figure 19. Figure 20 is a cross sectional view through the axles and wheels.

Force is exerted at both ends of the axle by 10-ton capacity screw jacks which are each driven by a motor. The screw jack pushes on a spring stack of Belleville washers, which pushes on the magenta-colored floating bearing housing. This bearing housing can move left and right with respect to the support structure shown on the left side of the figure. The wheel and axle supported by the red bearing housing on the right side of the figure is fixed with respect to its support structure.

The design concept of the spring stack is to change the force application of the

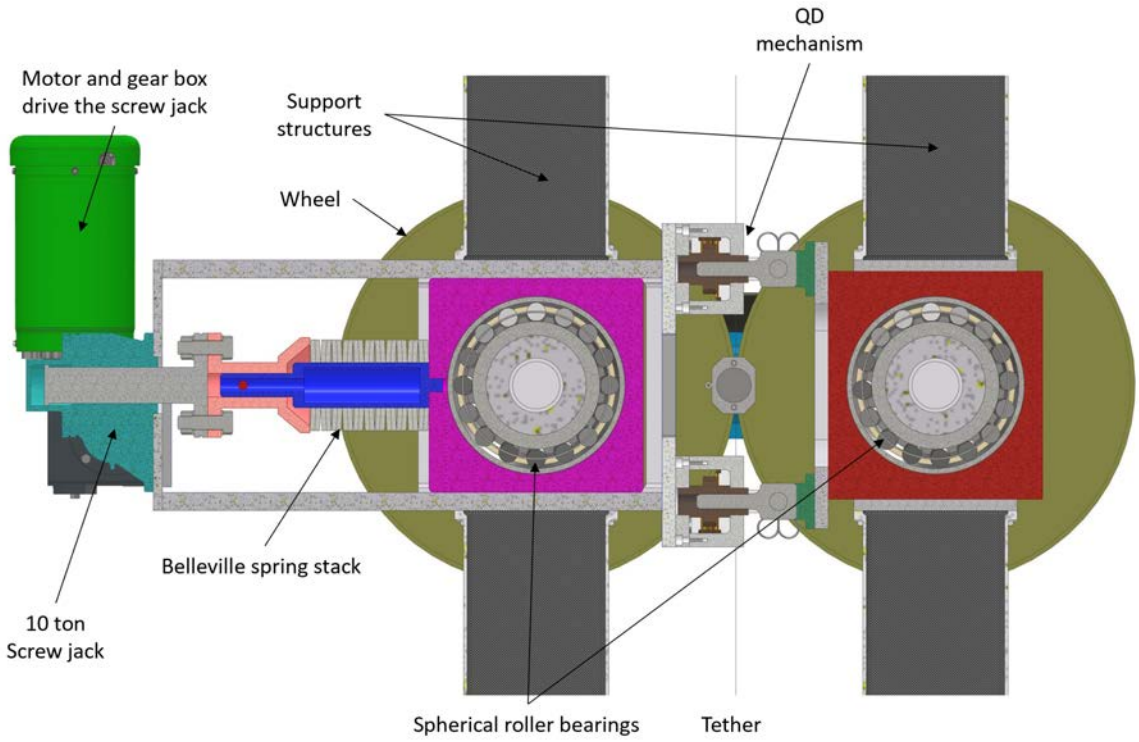

Figure 19: Section view of wheel compression mechanism

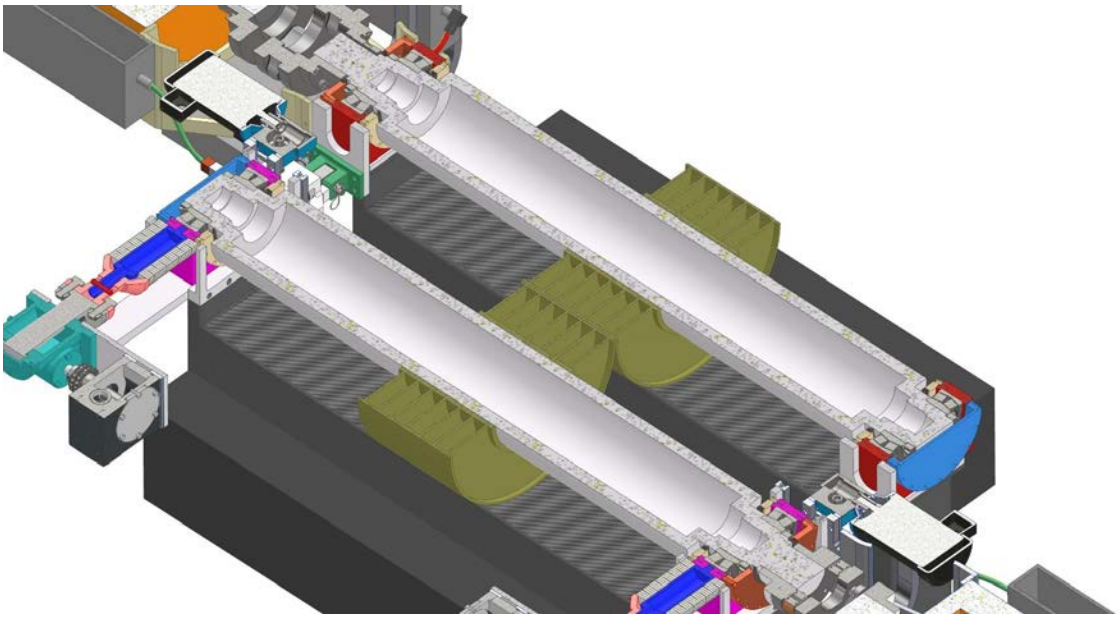

Figure 20: Cross section through axles to show sizes and spacing

screw jack from a step function to a roughly linear ramp function that gives the clamping control system greater resolution in applying the forces on each end of the axle. One design concept that has not been simulated or vetted yet is that a differential force from one end of the axle to the other may cause the wheel to take on a slightly conical shape. It is hypothesized that this shape may allow for steering correction of the climber as it ascends the tether. Load cells for measuring the applied load of each screw jack are not shown yet, but are assumed in the design.

Note that this design is based on the number of wheel pairs of the climber. The 10-ton screw jack applies enough force for a 20 t climber when there are ten wheel-pairs holding the climber up (as long as the coefficient of friction between the wheel and tether is at least 0.1). As noted earlier, the effect of the wheel compression mechanism on the axles is to put the axles in bending. Knowing the compression force required, finite element analysis was performed to study the stress in the wheels and axles. The force from the wheel compression mechanism on the rotating axles puts the axles in a state of fully reversed bending stress, the most damaging condition in metal fatigue. Since the axles have to rotate more than 20 million times just to get to GEO (see Figure 21), this puts the number of rotations well into the long-term fatigue range of the stress vs. cycles (S-N) curve, such as that shown in Figure 23. For the axles to survive, the allowable stress in them must be reduced well below the static yield strength of the aluminum 6061 alloy, 241 MPa. One mitigating factor is that the compression mechanism can be backed off as a function of altitude as gravity diminishes and the effective weight of the climber is less. This mitigation was not included in the fatigue analysis of the axle because it is hoped that the climber may

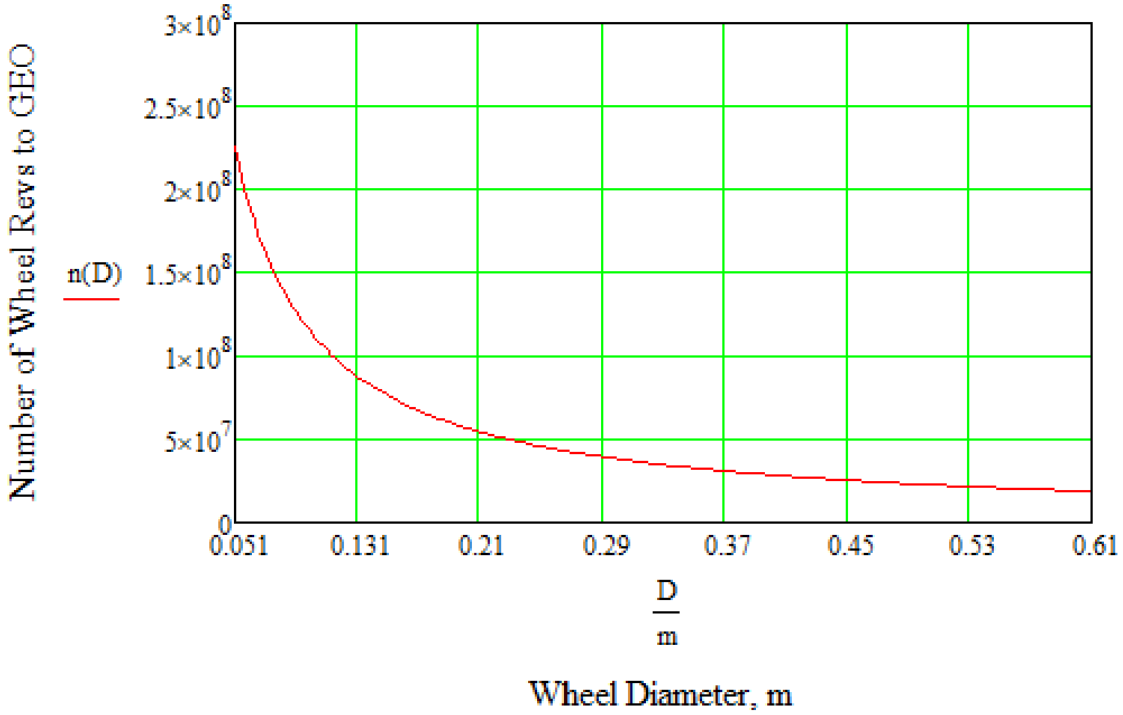

Figure 21: Wheel revolutions to get to GEO as a function of wheel diameter. The wheel in the model is 0.56 m in diameter, giving the number of revolutions to GEO of $\sim$ 20 million.

be used multiple times, so the allowable stress was kept conservatively low. A view of the stress in the axles caused by just the wheel compression force is shown in Figure 22. Dynamic stress from rotation is not included in this model.

To keep the aluminum axles from experiencing fatigue cracking, the axles had to be designed with an outer diameter and wall thickness that kept the stress in the axle below 68.95 MPa. The fatigue strength of the Ti-6Al-4V alloy of the wheels is higher than that of aluminum. The maximum stress in Figure 22 is 17.98 ksi (124 MPa) in the titanium wheel. From Table 2, the 97.5% confidence level allowable stress in fatigue for Ti-6Al-4V at 10^7 cycles is 429 MPa. This indicates that, for the trip to GEO, the wheels could sustain with a high degree of confidence this level of stress without fatigue cracking. It is not known at this time how welding the wheels together would affect the allowable fatigue of this material; the effect is very significant in aluminum.

Figure 22 shows that the stress state in the axles is at or below 10 ksi (68.95 MPa) everywhere. The analysis also shows that maximum stress in the wheels occurs near the outside faces of the hub of the wheels near the zone of contact. This is certainly a by-product of the bending of the axles. This effect may be mitigated in future by crowning the wheels, but the exact contour of the wheel needs to be studied to see if

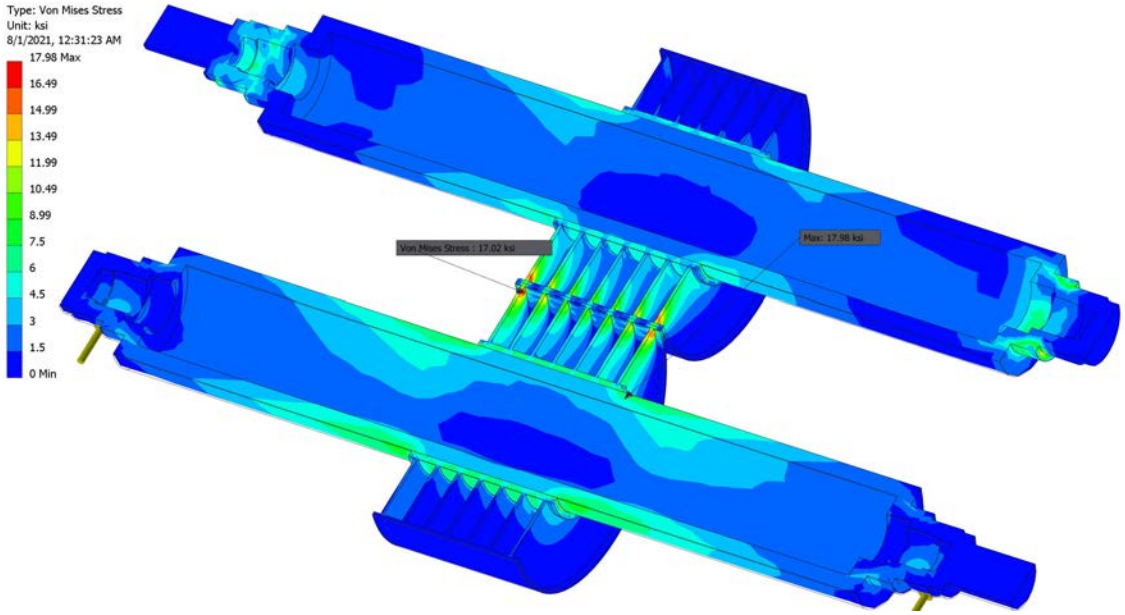

Figure 22: Von Mises stress state of the wheels and axles from wheel compression force

the steering hypothesis works.

Often left out of discussions of metal fatigue is that the trend line usually used to calculate the allowable stress in fatigue for a given number of cycles of stress is actually for a 50% confidence level rate of failure of the component. Figure 23 shows a restatement of the fatigue data from the MIL-SPEC Handbook (MIL-HDBK-5D 1983) that gives varying levels of confidence to failure. The bold red curve in the data is the trend line of 50% confidence of fatigue cracking failure. Below the bold red curve are the curves for 75%, 94.9% and 97.5% confidence of no fatigue cracking failure of a component. Above the bold red curve is the 25% confidence curve for survival of a component. The 68.95 MPa allowable stress quoted above comes from attempting to design the life of the axle to exceed 100 million cycles with 97.5% confidence of no failure. Figure 23 does not include modifying factors such as the presence of water or of welds in the part. As will be seen later, the axles may have to be designed for a shorter life to remain practical if the wheel compression force has to be increased.

The method of joining the wheel to the axle forces a more comprehensive fatigue stress analysis to take place in future. This design attaches the wheel to the axle by a thermal shrink fit of the titanium wheel on the aluminum axle. Calculations show that this method of joining the wheel and axle is perfectly feasible in that the temperatures required of the wheel and axle are within allowable limits for both metals to create a slip fit for assembly, while at room temperature producing a tight

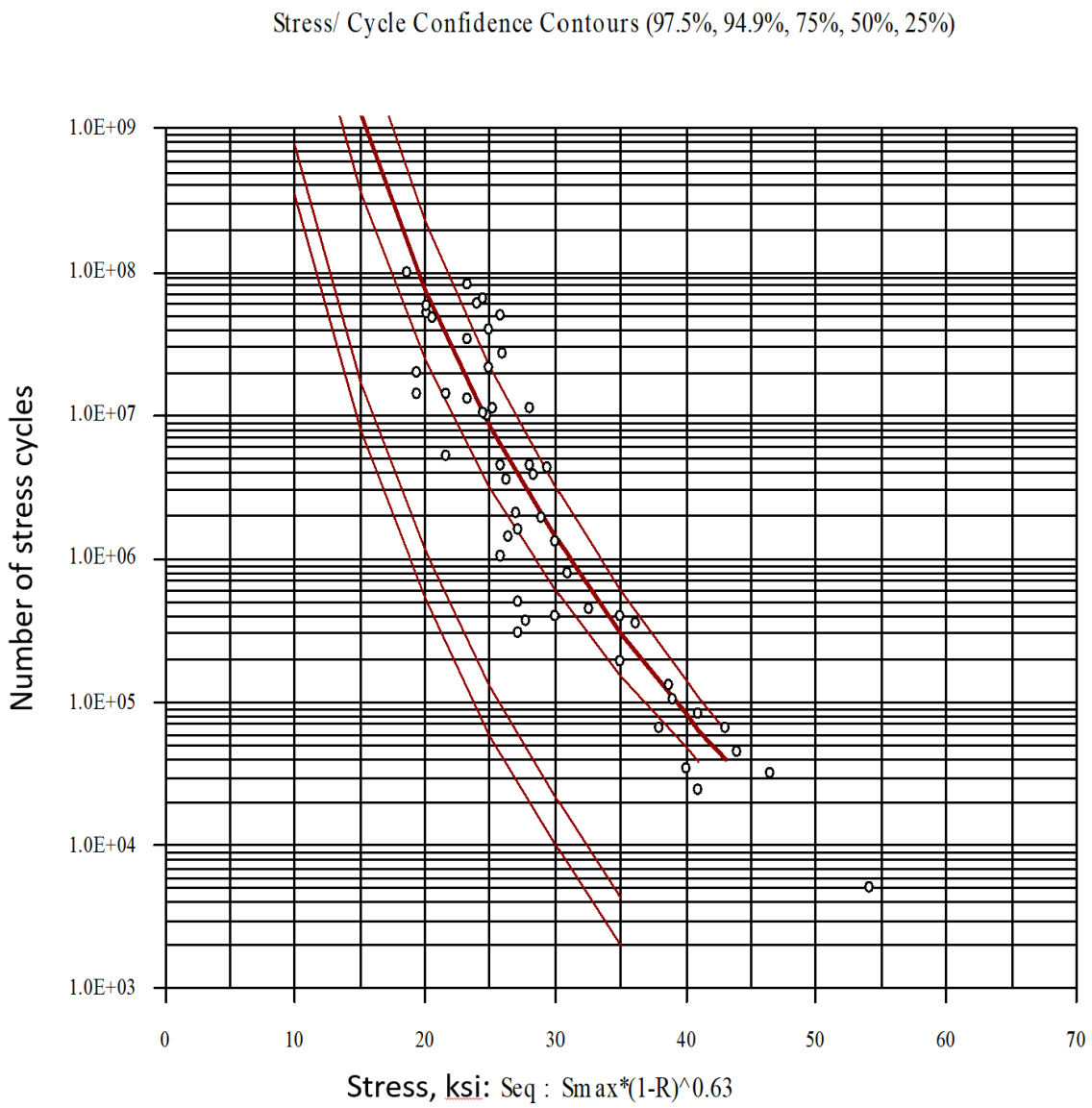

Figure 23: Graph showing how the allowable stress in Al 6061-T6 decreases with increasing number of stress cycles and confidence level of failure (Graph created by Dr. Ron Laszewski for the MiniBooNE experiment.)

enough fit to prevent the wheel from slipping on the axle. Another typical way of connecting axles and wheels is through a key and keyways in the wheel and axle. The thermal shrink fit method was chosen because a key would produce a concentrated stress in the axle that would most likely violate the allowable fatigue stress in the aluminum, and because the wheel hub would have to be thicker to create the keyway, increasing the wheel mass. One limitation of this finite element analysis is that it could not take into account the stress state between the wheel and axle caused by the shrink fit. This additional stress state must be added to the stress state caused by the axle bending.

The effect of rotation also increases the stress in the wheels and axles. Figure 24 shows the Von Mises stress distribution in a single wheel and axle spinning at 2000 RPM with no wheel compression force. Maximum stress is near the axle in the wheel hub and is 1.05 ksi (7.24 MPa). If the wheel were a simple ring with no hub, dynamic stresses from rotation would increase as the square of the product of rotation speed and the radius of the ring. As shown here, the presence of the hub creates a more complex stress state.

Figures 25 and 26 show the difference in stress state when the rotation speed is increased from 2000 RPM to 4000 RPM but the wheel compression force is held at 20 tons. The maximum stress is still in the contact area between wheels. The conclusion from these figures is that at the likely speed of rotation of the wheels of the climber (maximum 3000 RPM), the dynamic stress represents a small contribution to the stress state once the wheel compression force is applied.

The axle shown would likely be fabricated by welding different diameter tubes and rods of aluminum together. Welding is known to reduce the fatigue strength of aluminum by as much as a factor of two. If the axle shown is a weldment, then the allowable stress of 68.95 MPa is not conservative enough for 100 million stress cycles of the axle. Aluminum fatigue strength is also known to be reduced by the presence of water. An ocean-based space elevator Earth anchor platform will likely expose the climber to salt and water spray. This effect must also be included in the fatigue analysis, even though it is only relevant to climbing in atmosphere.

Figure 27 shows the deflection of the fixed and floating axles from the ten-ton screw jack loads applied to the ends of the floating axle (yellow arrows). The boundary condition on the fixed wheel axle (the one mostly in blue) is a fixed boundary condition placed where the spherical bearings would be located at the ends of the axle. This was the only boundary condition available in the finite element analysis (FEA) package used, and it does not have the degrees of freedom that the spherical bearings have, which would allow the ends of the axle to rotate. In effect, the boundary condition causes the fixed axle to look too stiff because its ends cannot rotate. If the boundary condition were similar to the floating axle, both axles would show similar bending deflection. The maximum deflection of the ends of the floating axle is 0.128 inches (3.25 mm). This deflection is large for machine components and causes the ends of the shafts to have a centerline which is at an angle to the motor shaft, hence the need

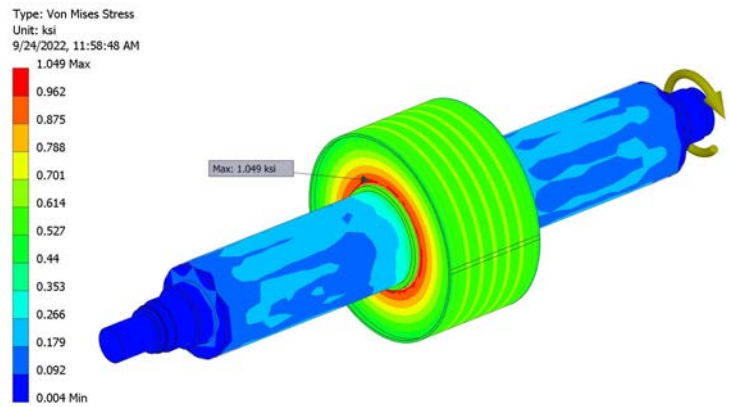

Figure 24: Von Mises stress in a wheel and axle caused by rotation at 2000 RPM with no wheel compression force

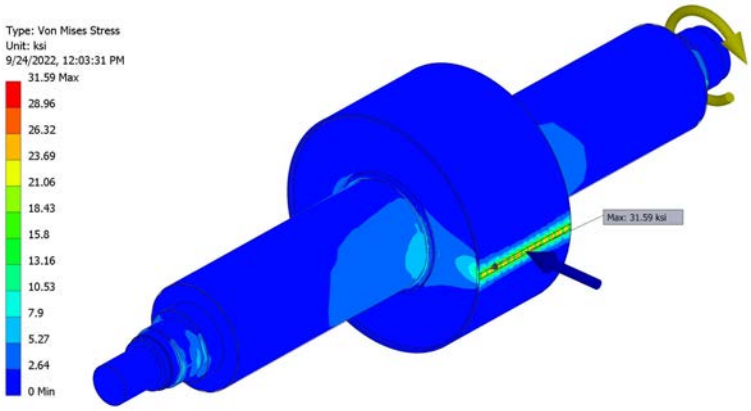

Figure 25: Von Mises stress in a single wheel and axle caused by 2000 RPM rotation and 20 tons of wheel compression force

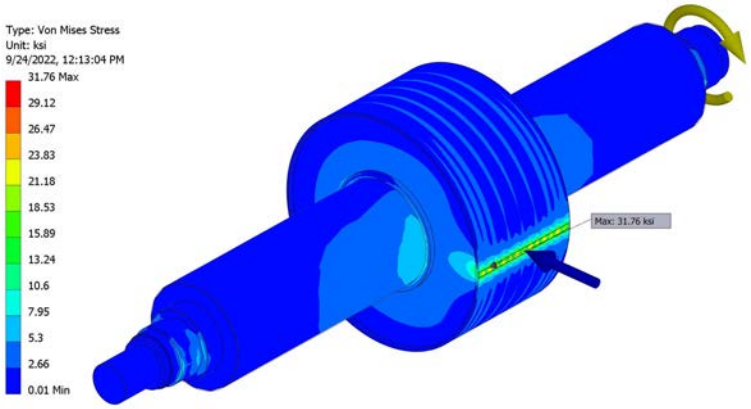

Figure 26: Von Mises stress state caused by 4000 RPM rotation and 20 tons of wheel compression force

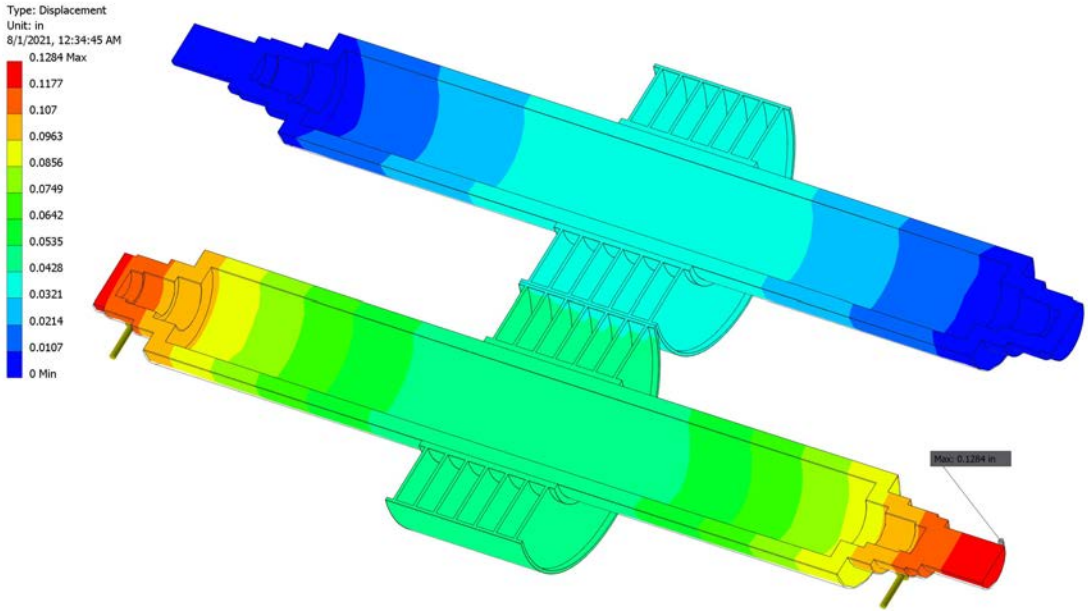

Figure 27: Deflection plot of the wheels and axles in bending from a 10-ton load applied at each end of the lower axle (yellow arrows)

for the spherical roller bearings.

Again, it must be emphasized that the ten-ton wheel compression loading on both ends of the axle is appropriate to a ten-wheel-pair climber. If there were fewer wheels, the wheel compression force would have to be higher to provide the full traction needed by the 20 t climber.

4.3.4 Coupling Between the Axle and the Motor Drive Shaft

As the wheel compression mechanism screw jacks push the floating axle toward the fixed axle, and the wheels both come in contact with the tether, the axle bends. The motor is fixed to the structure on the floating axle side of the climber. If the motor is fixed to the support structure, but the floating axle can move with respect to its support structure, how can they be connected together so that the motor can turn the axle? The answer is a Schmidt coupling. Figure 28 shows a Schmidt coupling sold by ZeroMax (Zero-Max 2022).

A Schmidt coupling is a collection of disks, linkages and bearings that allows a fixed shaft to connect to a movable shaft without additional side forces. Torque is transmitted with no diminution through the coupling and the rotational velocities of the driving and driven shafts are the same. What limits the torque capacity of the Schmidt coupling is the ability of the bearings to dissipate heat.

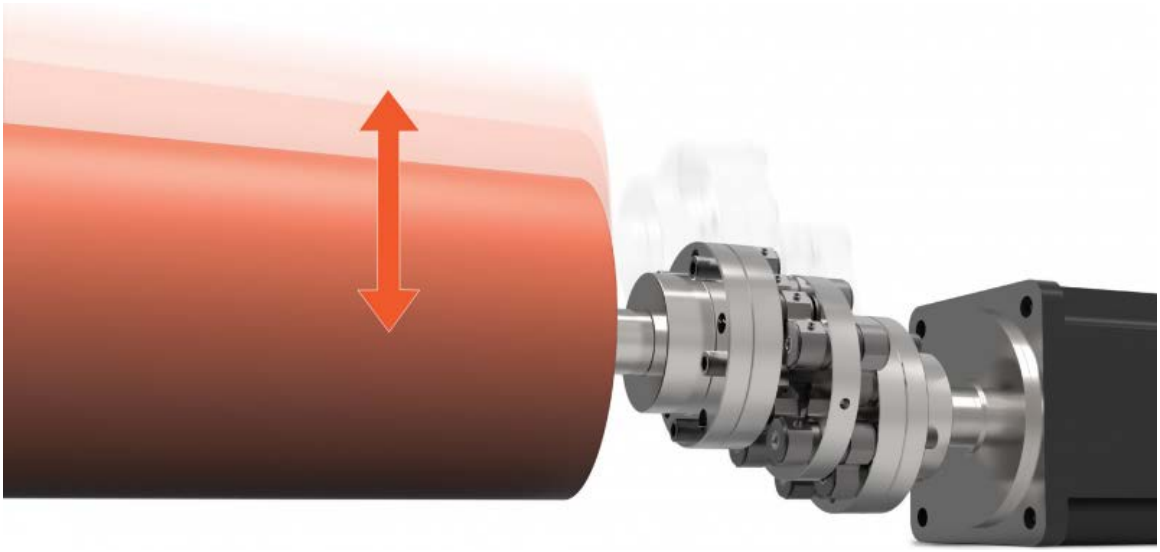

Figure 28: A Schmidt coupling connecting a moving shaft and a fixed motor. Image from Zero-Max (2022).

4.3.5 Quick Disconnect Mechanism

Figure 29 shows the quick disconnect mechanism which holds the two halves of the climber together around the tether. This mechanism must react the compressive load of the wheels as a tension on both sides of the climber, allow for easy connection of wheel modules on opposite sides of the tether and allow for emergency ejection of the whole climber from the tether.

The fixed axle side of the climber has two clevises above and below the axle. The floating axle side of the climber has the motor and gear box mechanism mounted to it on each side. A clevis pin connects the turnbuckles driven by the gear boxes to the clevises. The idea of the clevis pins is to make attachment of one half of the climber to the other as simple as possible. It is imagined that these pins will be engaged during assembly as the two halves of the climber are brought out to the tether and connected.

In the event that the climber needs to separate at any altitude, the quick disconnect mechanism would drive the turnbuckles out until they separated from their gear boxes. When the turnbuckles are clear of their gear boxes, the climber halves are free to fall away from the tether. An additional mechanism such as a compression spring or cold thrusters is needed to move the climber halves far enough away from the tether that they cannot strike it as they fall. This feature has not been included in the reference conceptual design yet. This mechanism uses battery power to drive the motor that causes the turnbuckle separation.

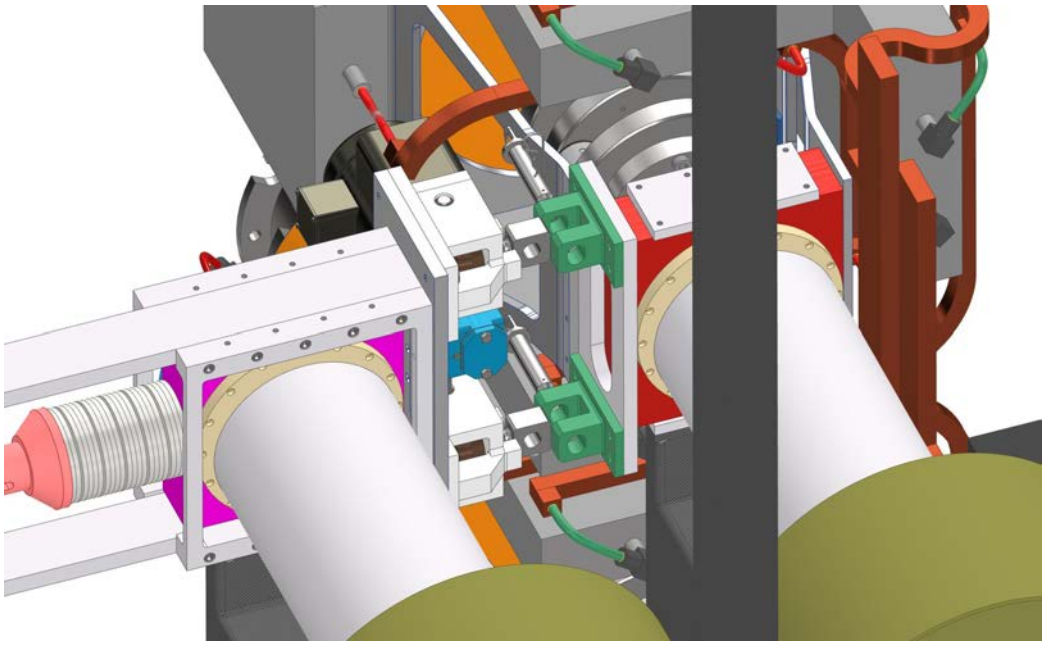

Figure 29: A close-up exploded view of the quick-disconnect mechanism is shown with the climber halves separated by 5 cm. The two clevises (green) are shown in the center of the figure with the clevis pins (silver) withdrawn.

4.3.6 Power Distribution

Power for the motors and other climber subsystems will need to be delivered by an electrical bus reaching throughout the climber chassis. Aluminum is the preferred bus material because it is lighter than copper and still able to handle the anticipated current loads. Large diameter, low gauge wire will be required in many places to take the current off the bus and send it to the motors. It is currently projected that magni650-style motors will require up to 3000 amps of current during startup. The main power bus is conceived to be an aluminum strip-line that runs from the bottom of the climber to the top. It gets its power from the PV arrays and distributes it to the motors and batteries.

The motors, drive components and electrical components in the primary drive system are depicted in the block diagram in Figure 30. Components operate at 800 V for three reasons: to minimize the current carrying needs and thus the weight of the aluminum bus structure while still achieving the power levels needed at the motor speed control/DC-AC inverter; to maintain power long enough to secure the climber on the tether in case of a failure of solar or beamed power; and to take advantage of the development work done on electrical vehicles (EV). The battery size and weight were estimated from the energy density of the commercial lithium-ion batteries in a standard Tesla EV (Kane 2022). Later in the development of the reference conceptual design, lithium-ion batteries were replaced with lithium-sulfur batteries because they have three times the energy density of lithium-ion batteries (Nedelea 2022). The

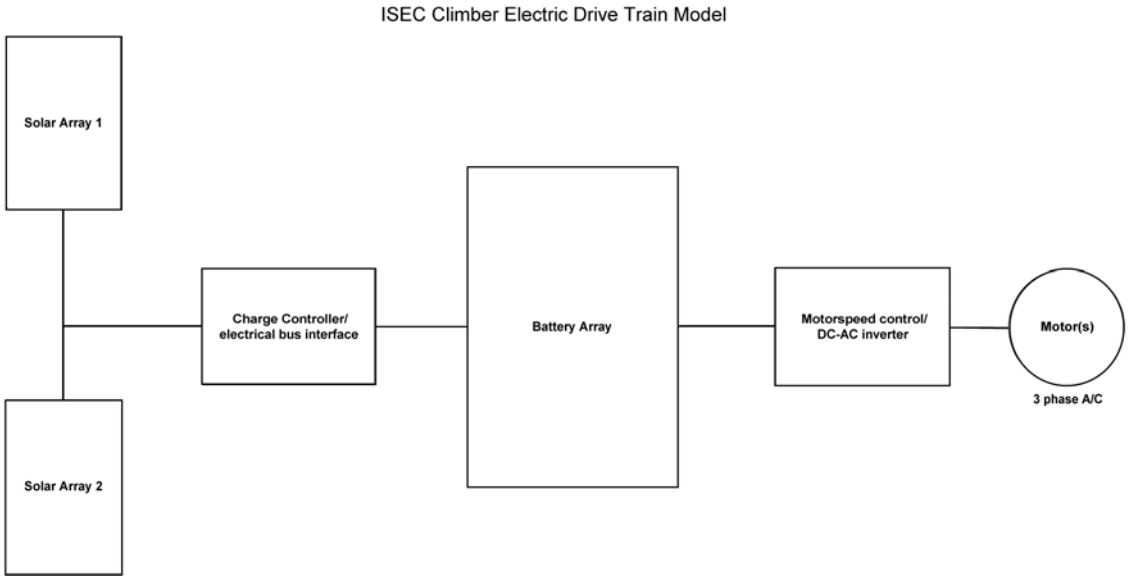

Figure 30: Block diagram of electrical components in the primary drive system

volume of the batteries shown was determined by the size needed to provide five minutes of reserve power to the drive motors operating at full power and complete a controlled shutdown of the drive power electronics (small gray boxes around the orange motors in Figure 31) and brake application in case of a power interruption. This was an engineering judgment that will have to be studied before real climbers can lift off.

Figure 31 shows a perspective view looking up from the bottom of one half of a climber with ten floating axle modules assembled together. The aluminum stripline/bus bar that distributes current to all the drive motors is highlighted in yellow. Smaller bars carry current to and from the batteries, shown as black boxes in between the green motors. All connections are conceptual. The batteries and motor drive electronics are connected in parallel in this design. Additional professional electrical and electronic engineering design development and testing is required to make this model more realistic.

The bus bars are an example of components that need to connect every floating or fixed axle module to its neighbors on the same side of the tether. Most of the assembly of a half climber can take place at the single-wheel level. The electrical system, as well as other fluid distribution systems, has to be threaded through all the wheel modules after they are bolted to each other. The connections of the main bus bar to smaller bus bars are shown as welded, but this is probably not the technology that will ultimately be used. To keep climbers in an easy-to-disassemble state, especially in space, a bolted or some other type of fastener connection that can carry kiloamps will be needed. To prevent the bus from touching grounded parts of the climber, insulating standoffs will be needed but none have been included in the model so far.

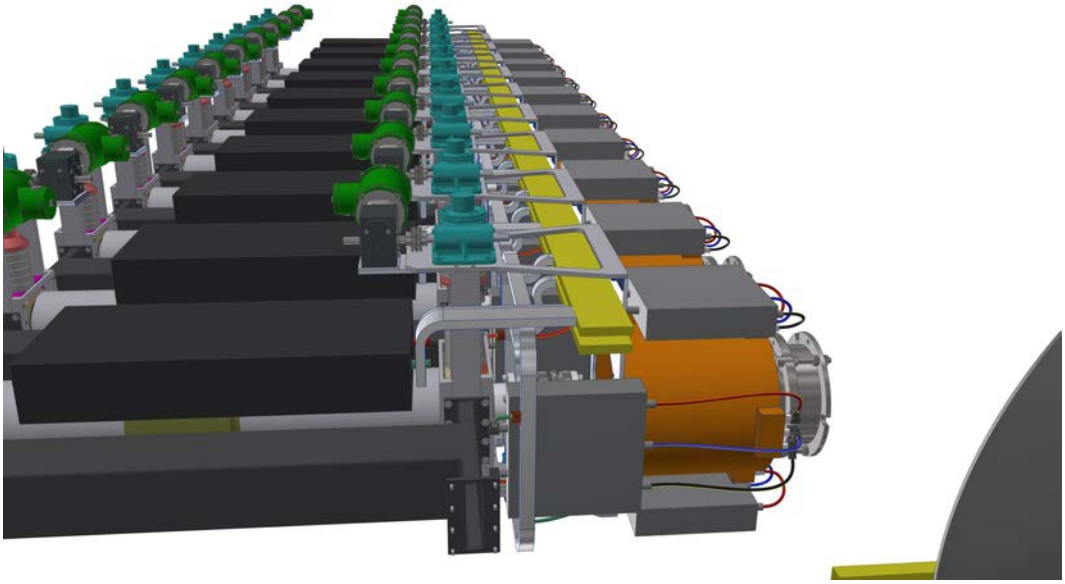

Figure 31: Perspective view of a climber half highlighting the bus bars in yellow

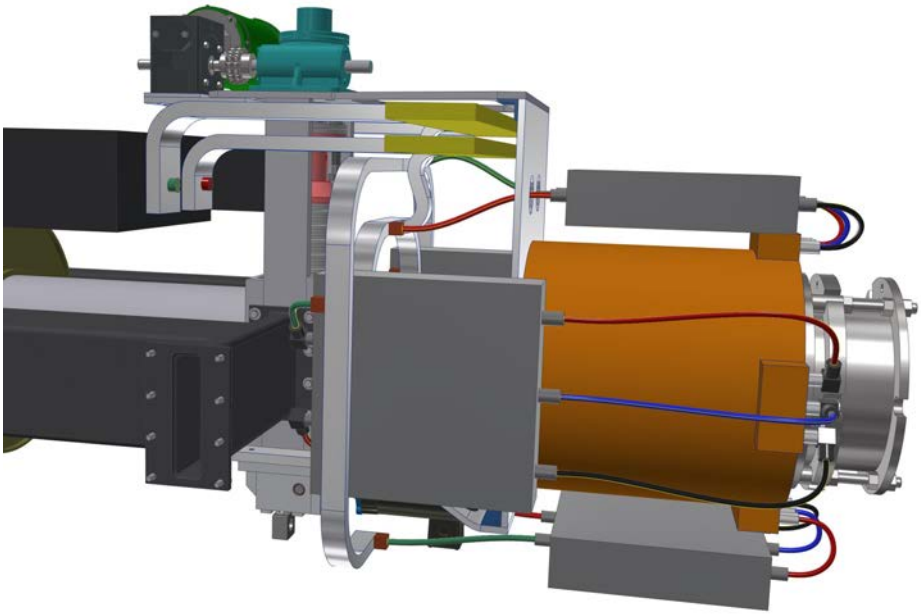

Figure 32: Section view looking up from the bottom of a floating axle module

The space around the motors and bearing housing gets tighter as more subsystems are added. Figure 32 shows the floating axle half of the climber in a section view to simplify the image and show the bus work that feeds power from the main bus bar to the motor driver electronics boxes. None of the insulators for these smaller buses have been added, nor are there support members for the electronics boxes.

Before even a conceptual design of the connections between the bus bar and the PV array can be done, more detailed design work is required for an 800 V PV array that can deliver kiloamps of current. These connections are represented in Figure 30 by the "Charge Controller/Electric Bus Interface" block. Power conditioning electronics have not been included yet.

4.3.7 Brakes

The brakes shown in the model (attached to the outside of the orange motors) are a modification of an Ogura (Ogura 2022) electromechanical brake. The unit shown is scaled up from a commercially available unit. It must have the torque capacity to hold the climber's position on the tether if the motor is not on. Unfortunately, brakes such as these represent a lot of mass in the drive train. Ultimately, custom light-weight units will have to be developed.

Dynamic braking could be provided by the motors. Static braking is only required in one direction (towards Earth below GEO), so it may be possible to install a simple ratchet-type clamp brake on the motor, shaft, wheel or tether itself.

4.3.8 Interconnecting Structures

A single floating or fixed axle module is not a stable object by itself. Because of bearings at both ends of the axle, anything attached to the bearing support housings is free to rotate with respect to the axle. The interconnecting structures are the skeleton of the climber that rigidifies and stabilizes the climber. Interconnecting structures off different materials are found throughout the climber, resisting loads in different directions.

In the original design all interconnecting structures were aluminum alloys. Aluminum is the lightest, strongest, and cheapest material to make structures from. The fact that all three of those adjectives can be applied simultaneously is what makes aluminum such an ideal material and common in spacecraft structures. It is readily available in many stock forms. Joining aluminum can be done by a variety of methods from simple bolted connections to welded joints.

Figure 33 shows an early version of a welded aluminum structure to hold wheel modules together and made from standard aluminum tubing. The structure shown weighs only 25.8 kg because of the thin-walled tubing. For scale, the center tube is 1650.8 mm long and 203.2 mm square with 4.8 mm thick walls. Buckling calculations on the vertical members indicate that it is capable of supporting the weight of the climber above if it were the bottom support structure of a climber.

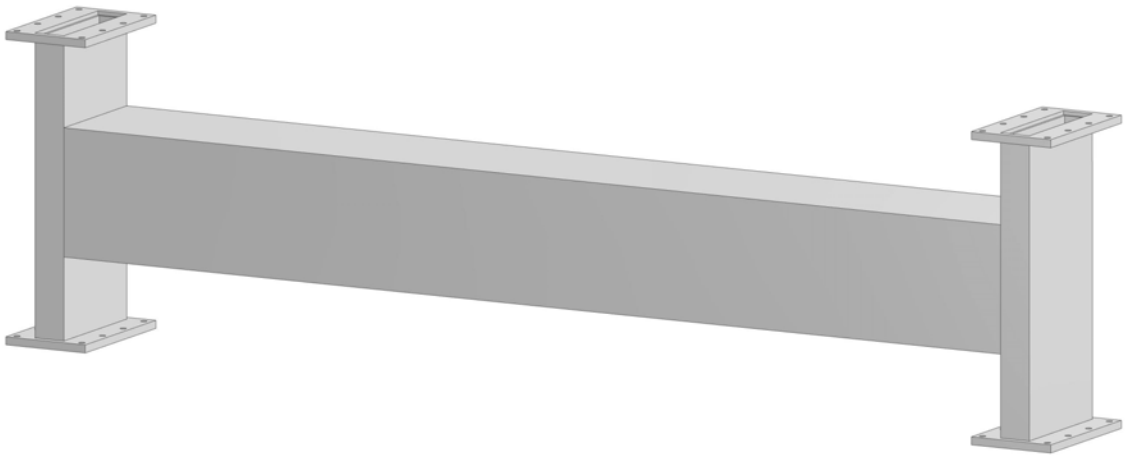

Figure 33: Aluminum weldment interconnect structure between wheel modules

To reduce weight, the structural interconnects between wheel modules were changed to carbon fiber reinforced polymer (CFRP). CFRP is slightly stronger than aluminum, and somewhat lighter. It is also much more difficult to design with. CFRP requires special fixturing to create any structural shapes because it does not come in stock rectangular structural tubes. Joining CFRP is a complex process with many limitations.

A CFRP structure of the same size and shape as the one in Figure 33 weighs just 13.6 kg. Instead of being made from individual stock pieces, this structure might be made as a single piece. CFRP is a brittle material so all corners must be rounded to reduce the effects of stress concentrations.

Another example of interconnecting structure would be that which surrounds the bearing housings and supports the wheel compression mechanism and the drive motors. Figure 34 shows a simplified, and Figure 35 a strengthened, CAD model of the aluminum support structure that holds up the 200 kg magniX motors and resists their torque when the motor is operating. The blue arrow represents gravity which applies the self-weight of the components. The orange arrows are forces coming from the moment on this cantilevered structure caused by the center of gravity of the motor being away from its mounting surface. If the center of gravity of the motor were in the plane of the mounting surface, these arrows would have zero force associated with them. The yellow arrows are the shear forces on the structure due to the 200 kg weight of the motor. The green circular arrow is the moment on the structure caused by the torque of the motor during climbing or holding the climber still on the tether at Earth's surface. The red block is the bearing support housing; it has a fixed boundary constraint representing its attachment to the rest of the climber structure.

The finite element analysis was done in separate load steps to study the distribu-

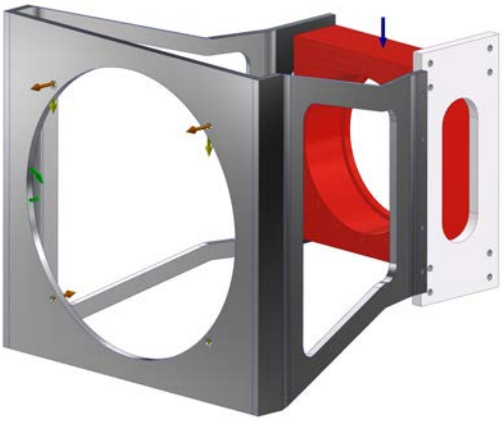

Figure 34: Finite element model of fixed axle motor support structure

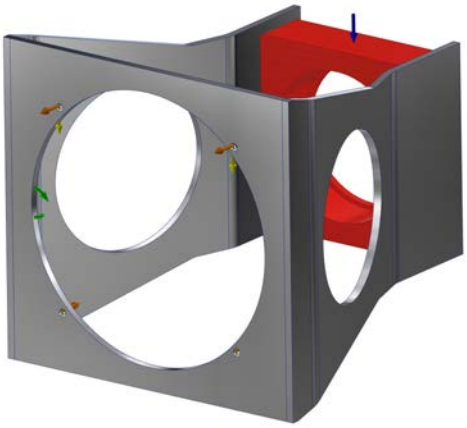

Figure 35: Modified motor mount frame to add stiffness

tion of stresses caused by different forces.

Figure 36 shows the stress state in the fixed-axle motor mount frame caused only by the weight of the drive motor that is not spinning; torque is applied to the frame only by the overhung weight of the motor. The motor mount frames are not subject to the kind of fatigue stresses that the axles and wheels are subject to, so the allowable stress for these quasi-static structures is the yield strength of aluminum divided by a safety factor. The static yield strength of Al 6061-T6 is 35 ksi (241.3 MPa). The maximum stress shown of 18.95 ksi (130.7 MPa) may be a small volume stress concentration because red is not an obvious stress contour color in the figure.

A maximum stress of $\sim$ 12.6 ksi (86.9 MPa) can be assumed at the top sides of the long, slender bars of the frame, where bending would produce the largest tension in the material. The safety factor for stress in this case would be 2.8.

Whenever a structure is analyzed, stress is always the first thing examined because the stress in the material must be less than the allowable stress for the design to succeed. Where the stress is not less than the allowable, the design must be modified. However, not every design is controlled by stress. The next design criterion looks at total deflection to see whether object distortions from applied loads are within acceptable limits. Deflection-controlled designs are always of lower-stress than the stress-controlled variety, hence deflection is a tighter design criterion that requires more support material to limit deflection.

Figure 37 shows the total deflection induced in the frame by the overhung weight of the motor alone. The maximum deflection is 0.105 inches (2.67 mm). This means that the motor shaft will be lower than the axle shaft by almost 3 millimeters. The fixed axle shaft couplings have some ability to absorb this offset, but they were designed mainly to absorb the angular offset caused by the wheel compression mechanisms.

Figures 38 and 39 show what happens when the motors are turned on and torque

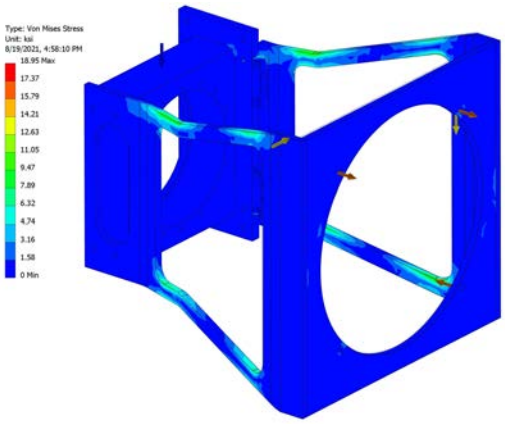

Figure 36: Von Mises stress in the fixed axle motor mount frame from the weight of the motor only

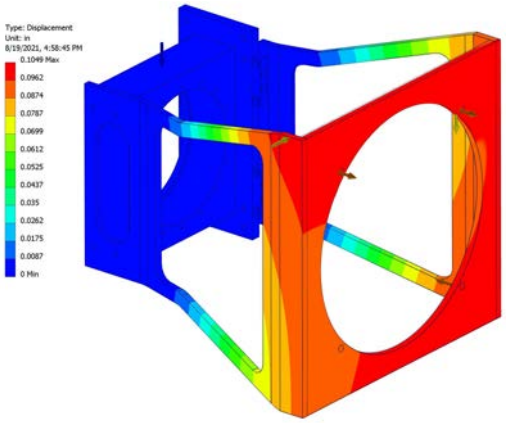

Figure 37: Total deflection of the motor mount frame with the motor not operating

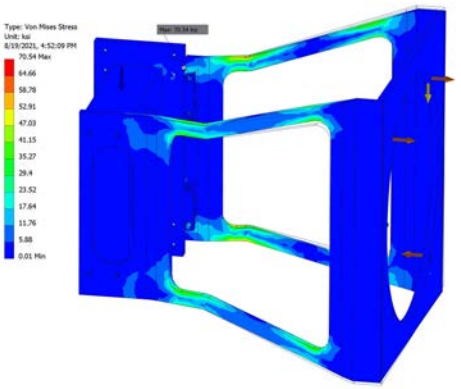

Figure 38: Von Mises stress in the motor mount frame due to motor torque

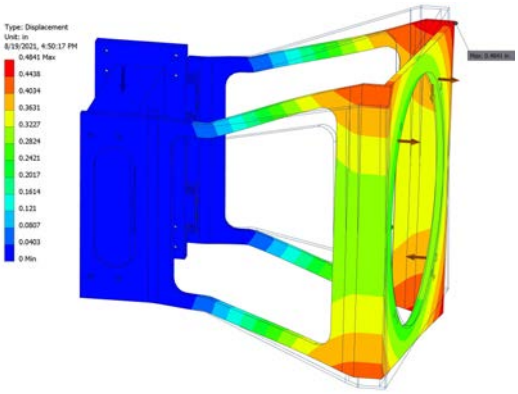

Figure 39: Total deflection of the motor mount frame with motor torque applied

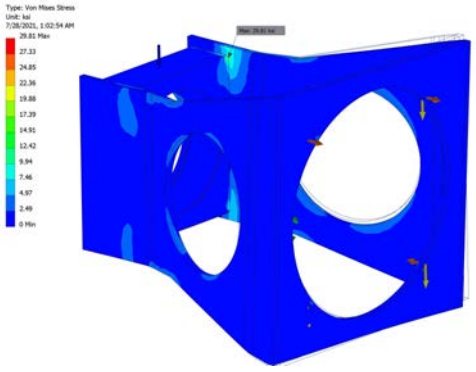

Figure 40: Von Mises stress distribution in stiffened motor mount with torque on

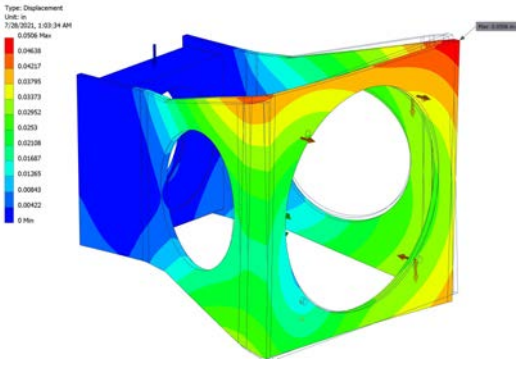

Figure 41: Total deflection of the motor mount frame with motor torque on

is applied to the motor mount frame. Figure 38 shows the stress distribution in the motor mount with the motor on and applying its full torque to the mounting structure. Stresses are much higher here with the maximum at a stress concentration being 70.54 ksi (486.4 MPa), well above the yield point of this aluminum. This value also appears to be a small volume, and in a truly static design, many stress concentrations can be disregarded as they will lead to local yielding of the members and stress redistribution. The FEA must also be studied to determine whether or not it is a meshing artifact or some other fictitious effect from the analysis method. It may not be completely accurate to characterize these mounting frames as truly statically loaded. Looking at the maximum stress in the thinnest members, it appears to be as high as 47 ksi (324.1 MPa) and this is not a small volume effect. The torque from the motor does over-stress the structure and therefore it is inadequate to support the motor during operation.

Figure 39 shows the total deflection of the structure, but it must be understood that this was a static linear finite element analysis. The nonlinear plastic behavior of aluminum was not included. The deflections here are at best the smallest possible deflections produced in a purely elastic material. Once the yield strength of the material is exceeded, aluminum exhibits a very ductile and nonlinear response. The deflections could be much larger in reality.

Standard procedure when a structure is found to be inadequate is to add material to stiffen the structure. Unfortunately, this has the adverse effect of adding weight to the structure. In this case, the size of the openings on the sides of the motor mount frame were reduced to put more material in place to distribute stress. Figure 35 above shows the changes made to the structure. Forces and moments applied to the frame are the same as before. Figure 40 shows that the maximum stress is now less than the yield stress, and the stresses in the narrowest cross-sections that carry the bending load are about 9 ksi (62.1 MPa,) so the design passes the stress criterion. Figure 41

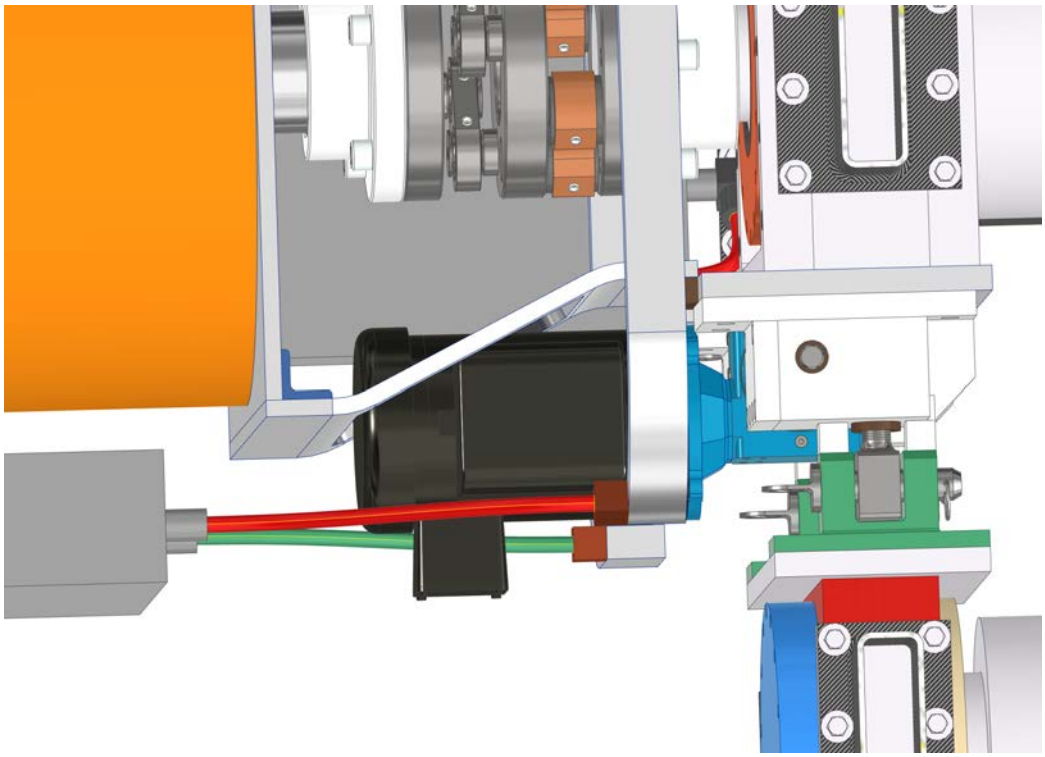

Figure 42: View of the fixed axle motor mount assembled into the climber showing penetration of the quick disconnect motor (black) into the angled cutout (silver)

shows that the maximum deflection is now 0.051 inches (1.3 mm), which is probably also acceptable. This structure looks adequate for the applied loads associated with a magni650-style motor, and could possibly benefit from a little trimming to reduce weight.

This analysis has not yet been incorporated into the assembled climber pictures shown here. The climber shown has a fixed-axle motor mount support frame that is not strong enough to support the drive motor. This means that the weight of the drive support included in the total mass is too small.

Figure 42 shows that the motor for the quick disconnect mechanism that is mounted to the floating-axle module adjacent to the fixed-axle module actually penetrates the space occupied by the fixed axle motor mount structure. The size and shape of the cutouts in the side walls of the motor mount frame shown in Figure 35 needs additional work to make sure that it allows for the attachment of the floating-axle module without interference.

This analysis is just one of many different kinds of analyses that must be applied to the entire structure accounting for all loads at any altitude. This design work will have to wait for a full climber design engineering team to tackle it.

4.3.9 Mass Budget

At this point in the design, many of the components making up the reference conceptual design are known and a relatively complete CAD model has been developed. It is possible, then, to see if the requirement of a 7 t drive train capable of carrying 13 t of payload has been satisfied. All of the components of the CAD model have materials associated with them which allows their weight to be calculated. Some of the commercial component CAD models were modified so that their weight came out to the catalog value of the weight of the component.

Figure 43 shows the top of the bill of materials table generated from the CAD model of the climber. There are over a hundred individual components, many of which, such as bolts, are repeated dozens of times. Many of the fasteners and small support structures for the batteries, drive electronics, and bus bar have not been designed yet and so do not appear in the mass budget.

The end result of the design effort so far is a climber traction module with a total mass of 20.2 t, more than the assumed total mass of the climber with payload. This result forced the exploration of a number of options to reduce the weight of the traction drive.

4.4 Reducing the Weight of the Traction Drive

The main problem with the weight of the climber traction drive can be traced back to the specifications of the motor. A search for the lightest, most powerful motor available identified the magni650 as initially meeting requirements. The size of the wheel came from the rated rotation speed specification for this motor, 1900 RPM, and the requirement of an average speed for the climber of 200 kph. Given the output torque of the motor and the size of the wheels, the number of wheel pairs was derived from the rated torque specification of this motor.

The weight of the drive train can likely be reduced by one of three options or combinations thereof: reducing the wheel radius, using lighter materials or finding a motor with a higher torque to mass ratio. Reducing the drive mass by half could be accomplished by halving the wheel radius, thus halving the number of wheel-pairs needed and reducing the climber mass by about half. Choosing materials with half (or less) the density of those used so far would accomplish the same end. Finding a motor which produces twice as much torque for the same 200 kg mass would also be a solution.

4.4.1 Reducing the Wheel Radius

The number of wheel pairs is given by

$$N_{wheels} \geq m_c g R_W / M_{max}, \tag{65}$$

where M_{max} is the maximum torque the motor can generate, m_c is the climber mass and g is the acceleration due to gravity at the Earth's surface.

Rank	Part Number	Thumbnail	QTY	Unit Mass, kg	Total mass, kg	Percent of total mass	
1	560 kW motor		20	200.25	4004.98	19.89%	
2	MNB_500J_modified		20	130.45	2608.98	12.96%	
3	SE-20t AXLE		20	109.20	2184.08	10.85%	
4	battery pack		20	84.02	1680.40	8.35%	
5	SE-20t WHEEL-2		20	63.96	1279.23	6.35%	
6	Motor driver electronics box		80	12.09	967.55	4.81%	63.21%
7	McM 6135K111 AC MOTOR		20	38.36	767.18	3.81%	
8	zero-max_l411c		10	68.69	686.90	3.41%	
9	McM 2721T24_SPHERICAL-ROLLER BEARING		40	12.66	506.58	2.52%	
10	PV Array 6 MW		2	242.28	484.57	2.41%	
11	JD-WJ810I2S-002.00-STDX-STDX-X_Jack Housing - 10T_Inverted		20	22.44	448.76	2.23%	
12	zero-max_l582s		10	39.52	395.24	1.96%	
13	McM 3540N210 FACE-MOUNT AC MOTOR		20	16.63	332.59	1.65%	
14	0230-02568		20	15.20	303.99	1.51%	
15	Fixed BEARING HOUSING-2		20	11.33	226.63	1.13%	
16	Belleville Spring		440	0.50	220.90	1.10%	
17	SE-04 BEARING HOUSING		20	9.94	198.83	0.99%	85.92%
18	SE-04 SLIDE BAR 1		40	4.21	168.34	0.84%	
19	CFRP Interface structure		10	13.55	135.49	0.67%	

Figure 43: Partial table of the component masses for the ten-wheel-pair climber. Brakes are labeled MNB_500J_modified and Schmidt couplings are labeled zero-max. The percentage of the total climber mass due to each component is highlighted, with the far-right column representing the cumulative mass percentage.

Reducing the radius of the wheel reduces the number of wheel pairs needed. The downside of this is that if the motor can't spin any faster, then the speed of the climber is reduced from the average of 200 kph and the trip takes longer than required. Another problem is that reducing the wheel diameter reduces the distance between the centers of the fixed and floating axles. This reduces the amount of space for the bearing housings and the quick disconnect mechanism. The extreme of this would be to make the wheels the same diameter as the axles. This would eliminate all of the space for the bearings and quick disconnect mechanism.

The ten-wheel-pair climber design allowed the development of many of the subsystems and features needed to assemble the climber and support the magni650 motor. When the development was near completion, with a few significant exceptions, the additional weight of the other subsystems became too high for the magniX motor to lift.

4.4.2 Material Substitution

A very helpful way to determine which materials would be stronger and lighter than aluminum would be to sort through all the known materials and plot their strengths versus their densities. If another material has the same strength as aluminum but less density, then the structure would have the same volume in the new material but would be lighter. If the new material has the same or higher density as aluminum but is much stronger, then weight reduction can happen by redesigning parts to have a smaller cross-section.

Exactly this kind of plot exists (Ashby 2011) and is shown in Figure 44. Among the few candidate materials that are as strong as aluminum but lighter are CFRP and the magnesium alloys. Magnesium alloys have the disadvantages of not having many stock sizes available and being difficult to join. The ceramics overlap this strength and density region of the plot, but suffer from extreme brittleness and difficult fabrication. There may be other composites besides CFRP in the purple region that would work. Surprisingly, beryllium falls within the oval of the magnesium alloys with a density of 1844 kg/m3 and yield strength of 240 MPa. Beryllium is a very light and strong material with the downside that it is toxic to some humans, and very expensive. Beryllium is reserved for very special applications in the nuclear and aerospace fields. Even if it were non-toxic it would still not be superior to CFRP.

What is clear from the graph is that there is no material that is half (or less) the density of aluminum alloys and equally strong. The lowest density materials are things like very weak polymer foams and wood.

Due to the conceptual nature of this study, the cost of components and their possible substitutions was not a prime consideration. In some cases, however, relative cost may have to be considered along with the purely technical and manufacturing tradeoffs. Figure 45 shows for various materials the strength on the y-axis vs. cost per volume on the x-axis (Ashby 2011). While CFRP is lighter and slightly stronger than aluminum, the plot shows that it is also greater than ten times as expensive. Because

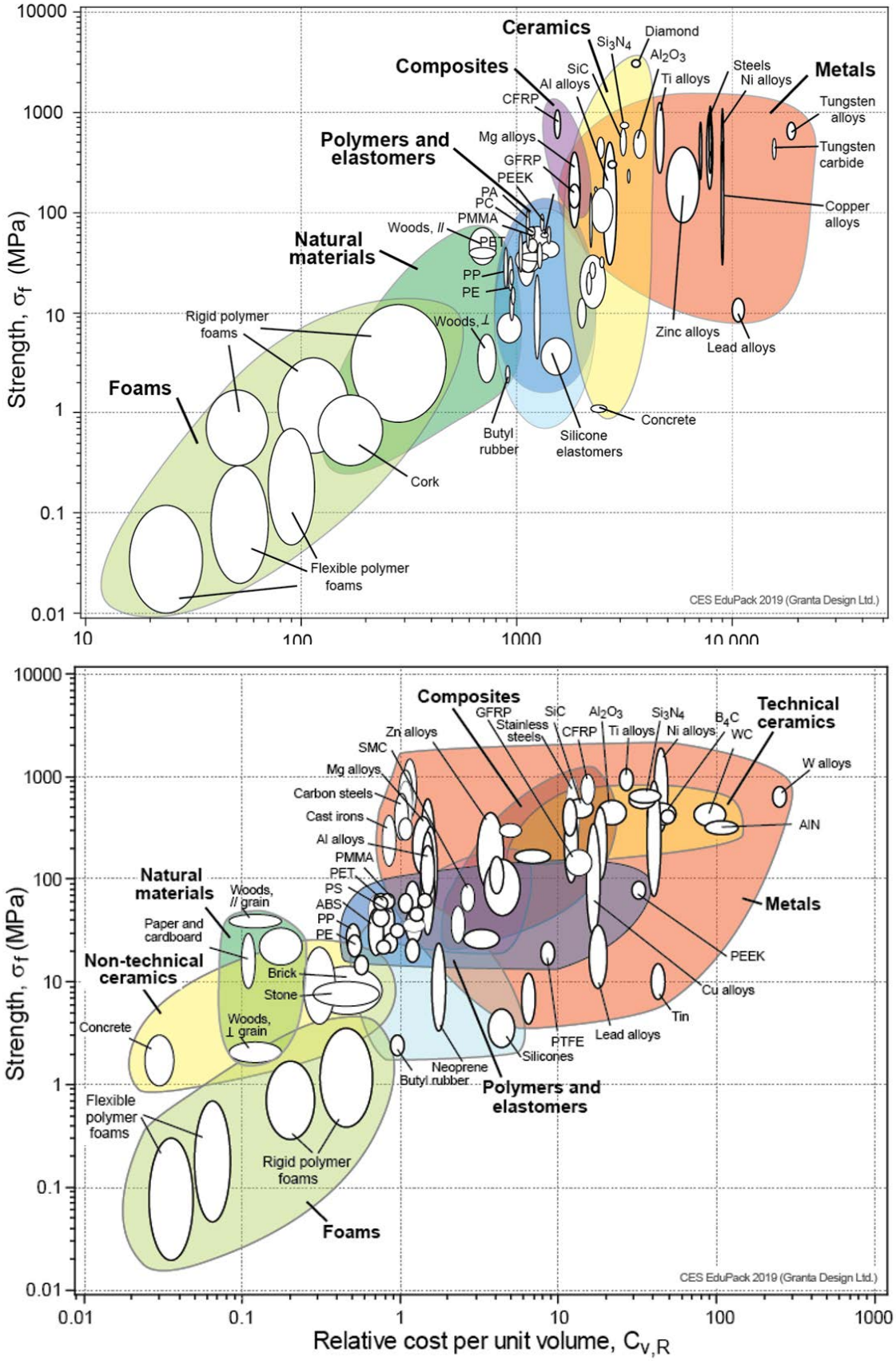

Figure 45: Ashby plot of strength vs. cost for various materials

early climbers may only make one-way trips to space, they could be considered as consumable items. In this case the cost of climbers may dominate the expense of sending payloads to GEO and beyond.

Not all of the climber is made of aluminum and not all of the different materials can be replaced. The bearings are high-strength steels. There are simply no replacements for this material for bearing construction that would allow high load carrying ability and long life. Until large scale production of bulk graphene is available as a current carrying conductor, the aluminum bus bars are the optimal weight for the current requirements. Stress in the wheels precludes making them from aluminum. There, the stronger material, titanium, is actually heavier than aluminum.

Motors are made with ferrous superalloys to maximize the magnetic permeability of the rotor. There are only a few elements and alloys that are at all magnetic and they don't come in versions with half the density.

The conclusion is that there are some substitutions possible, but that the weight reduction cannot be done solely by material substitution. The densities and strengths of the candidate materials are not different enough to reduce the weight of the climber as much as it needs to be reduced, and there are currently no known substitutes for some materials with special properties.

4.4.3 Increasing Motor Torque

The typical answer to a motor with insufficient torque to lift a load is to put a reducer or transmission in between the motor and wheel. The gear reduction of the transmission transmits higher torque to the wheel for the same output torque of the motor by sacrificing speed. If a motor-reducer combination could be found that weighed the same as the magniX motor, then the climber would climb more slowly but would have sufficient torque.

Because the effective weight of the climber decreases with altitude, the torque required to hold the climber on the tether is a maximum near Earth. At altitudes of 2600, 6207 and 13000 km the climber weighs one-half, one-quarter and one-tenth, respectively, what it weighs at the surface of the Earth. This reduction in effective weight looks like a natural application of a transmission that can change the gear ratio between the motor and wheel as a function of altitude. Near the surface of the Earth, the gear ratio could be 2:1 reduction, changing to 1:1 higher up and above 6,207 km it could change to a speed increaser at 1:2. This means the climber would climb more slowly near the Earth and speed up the higher it got. Having high torque motors at high altitude means that the speed increaser stage of the transmission could increase the climb speed dramatically.

Given the rated speed of the magni650 motor at 1900 RPM, a speed increaser with a ratio of 1:2 would produce a rotation speed for the wheel and axle of 3800 RPM, doubling the speed of the climber from 200 kph to 400 kph. While this sounds like a desirable outcome, in fact the spherical roller bearings on the axles also have a maximum rotation rate. The bearings selected have a maximum rotation rate of

3100 RPM. Bearings spun over their maximum speed develop an instability that greatly increases the friction between the rollers and their cage inside the bearing. The bearing quickly heats up. The steel bearings are mounted in aluminum housings and since aluminum melts at 660 C and loses its mechanical properties well before that, destruction of the climber would swiftly follow.

There are four different types of transmissions: mechanical, including gears, chains, belts, rollers and cams; electrical, such as motors which are infinitely variable transmissions; hydraulic, such as car transmissions and torque converters and; pneumatic.

Hydraulic and pneumatic options are not considered here; they require too much additional mass from pumps, storage tanks, plumbing and so on.

The magni650 motor is specified to transmit 2814 N-m of torque continuously at 560 kW of power. These are larger numbers than for automotive transmissions, where most transmission designs were developed. Industrial transmissions in the required range are not designed to be low mass.

All transmissions can be divided into two basic types: infinitely variable, referred to as continuously variable (CVT), and discretely variable. Infinitely variable transmissions have a gear ratio that changes continuously between their extreme values. Discretely variable transmissions have integral gear ratios, such as those found in the manual transmission of a car. The continuously varying effective weight of the climber makes a CVT look like a natural application for a climber. CVTs are, at their heart, traction drives that rely on friction and shear in the lubrication layer between rolling elements. The biggest drawback of a CVT is that different transmissions in the same climber would operate at slightly different gear ratios.

By extrapolating from automotive transmissions, it was found that a reducer able to transmit and multiply the given torque (2814 N-m) from the motor would weigh as much as three times the weight of the motor. There is no combination of motor and reducer that weighs as much or only slightly more than the motor itself. Reducing the number of motors by half but increasing the mass of the motor/transmission combination by four times does not reduce the total mass of a five-wheel-pair climber.

4.5 Five-Wheel-Pair Climber Design

The solution that allowed the conceptual design to proceed was to assume that a motor could be built someday that could deliver twice the torque of the magni650 motor and still have a mass of 200 kg. Any new motor would also have to have the same volume.

Such a motor could be produced today. Helix (HelixMotor 2022) manufactures high-torque, lightweight motors for aircraft and electric vehicles. They have the capability to custom-build motors that provide 5600 N-m at 2000 RPM. Based on motors already produced, these would weigh between 180 and 225 kg. It is not clear yet what the size of these motors would be, but it is likely that they would fit into the current design of the climber chassis.

Still greater torque and power density could be achieved in the near future and research into this area was identified as crucial to the success of the space elevator.

4.5.1 Adapting the Climber Components to the Five-Wheel-Pair Design

Using the Helix motor prompted a re-examination of some of the other components and subsystems of the climber.

The screw jacks in the wheel compression mechanism were changed from 10 ton units to 20 ton units. The gearbox and motor that drives the screw jack was upgraded to units that could drive the new screw jacks. The Belleville springs were reconfigured to handle twice the load.

One subsystem that did not get upgraded was the quick disconnect mechanism. In the five-wheel-pair climber the tensile load in the quick disconnect mechanism was doubled to 20 tons on each side. Components of similar size could be used if they were made from much stronger alloys. For example, if the turnbuckles were made from 4140 steel, they might be strong enough for the extra load. The entire subsystem needs to be examined in detail because the torque required to tighten the quick disconnect mechanism has also gone up. The three gear boxes need to be analyzed for adequacy.

Motors that deliver twice the torque of the magni650 at the same 1950 RPM run at twice the power, or 1.12 MW. This will require doubling the current to the motors, so the bus bars need to be checked for adequacy. They were designed initially to carry 2.5 kiloamps of current. This may not be enough for the new motors, especially during startup.

A finite element analysis of the axles and wheels for the new 40 ton wheel load was performed.

Figure 46 shows that the maximum stress on a wheel pair has gone up to almost 36 ksi (248.2 MPa). As expected, twice the load on each end of the axles creates twice the stress everywhere in the assembly. The maximum stress is a stress concentration in the interface between the axle and wheel. The bending stress in the axle is now approximately 21 ksi (144.8 MPa.) This stress reduces the fatigue life of the axle considerably. Using the graph in Figure 23, the 97.5% confidence limit of the fatigue life of the aluminum near the wheel may be reduced to 5×10^5 stress cycles. This number of rotations is not close to the 2×10^7 rotations needed to get to GEO. The size or materials of the wheels and axles will need to be evaluated further and modified to increase the likelihood of survival to GEO.

Figure 47 shows that the maximum deflection of the floating axle has now increased to 0.26 inches (6.6 mm). It will take a detailed analysis of the shaft coupling between the axle and motor to determine if this offset and angle exceeds the capability of the Schmidt coupling.

Figure 48 shows the safety factor calculated by taking the ratio of the yield stress to the equivalent stress at each point. This analysis shows how close the components are coming to the yield stress of each material. In a static structural application, this kind of safety factor is sensible because the allowable stress is the yield stress. Because

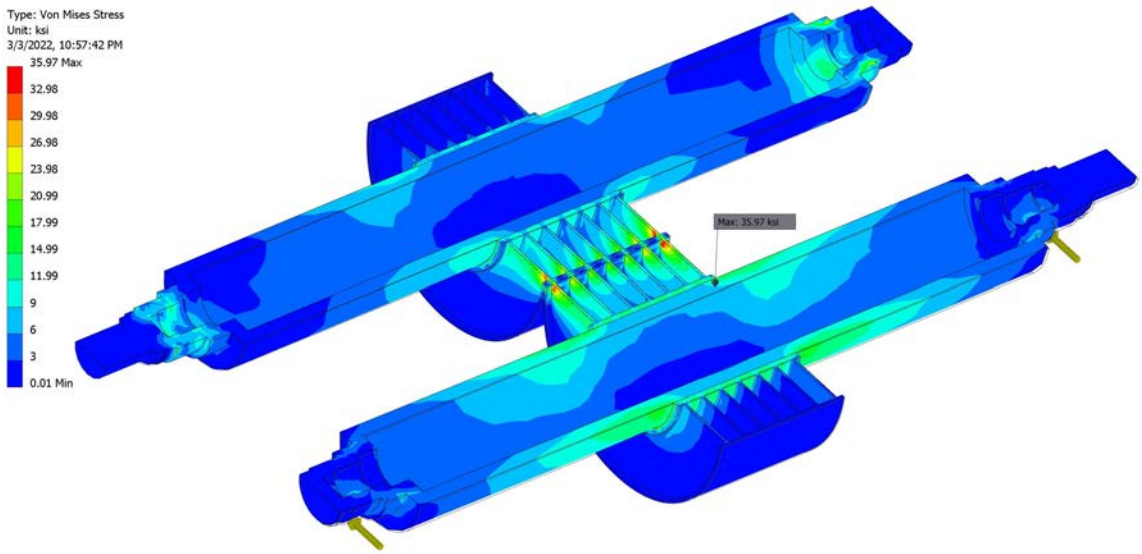

Figure 46: Von Mises stress in the wheels and axles with 20 tons on each end

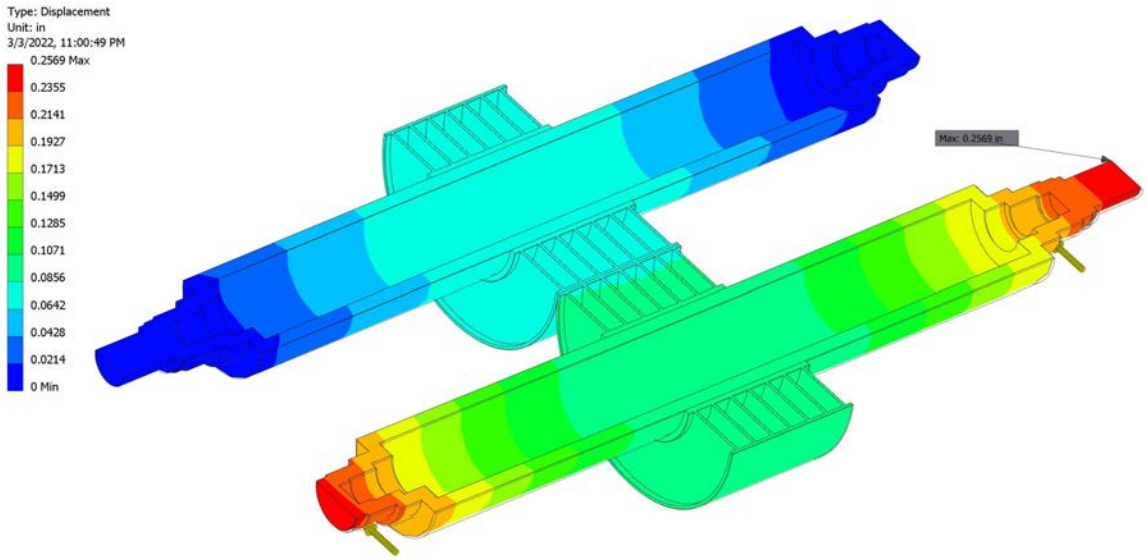

Figure 47: Total deflection of the wheels and axles with 20 tons on each end

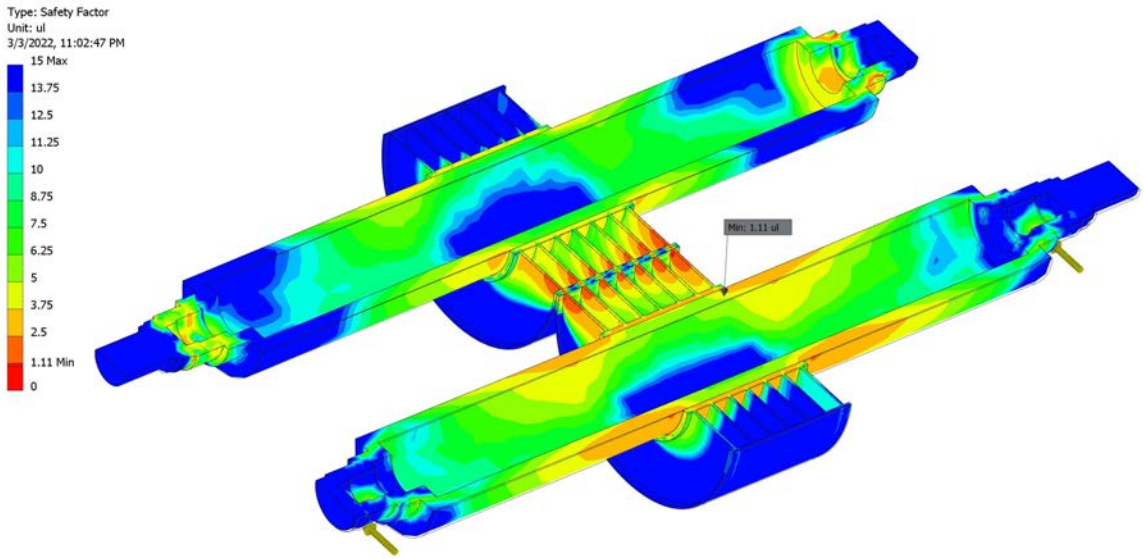

Figure 48: Calculated safety factor for 20 tons on each end

the wheels and axles are in a dynamic stress state that leads to fatigue, coming close to the yield stress of the material is very bad. It looks like the lowest safety factor is in the hub of the titanium wheel. In any case, the interface between the wheel and axle is a likely place for fatigue cracks to begin propagating through the axles.

Another change that was considered but not incorporated into the model was the Schmidt coupling connecting the motor to the axle. The new motors deliver twice as much torque as those in the ten-wheel-pair climber. The Schmidt couplings must be able to deliver this new torque. Figure 49 shows a size comparison of the Schmidt couplings available from ZeroMax. The couplings in the center and left of the image are those currently in the model for the floating and fixed axles. The coupling on the right is the size that would be appropriate for twice the transmitted torque. The larger couplings also have practical speed limits of 1000 to 1750 RPM, less than our desired speed range of 1900 to 2600 RPM. For this climber, it then becomes necessary to have custom-designed shaft couplings.

As shown above (section 4.3.8), the motor mounting structures are probably all inadequate for the doubled torque.

All of these points show that much work still needs to be done to upgrade the five-wheel-pair climber and get a more accurate mass for the traction drive. Every kg added to strengthen the traction drive takes away a kg of payload.

The five-wheel-pair climber is shown in Figure 50 and a listing of its main components and masses is shown in Figure 51. This configuration weighs 10,528 kg. It has the same overall conceptual design, but with upgraded components, as the ten-wheel-pair climber. More non-payload mass must be added to include a heat dissipation system, which will depend on the nature of the payload. If a specific payload exam-

Figure 49: Size comparison of Schmidt couplings. The couplings in the current design are shown at left and center. The larger coupling to handle double the torque is shown on the right. The ruler below is 6 inches (15.24 cm) long.

ple, liquid oxygen, is taken, the mass of two tanks and support structure is 485 kg. How this value was determined, including a description of the support structure and overall size, is given in Appendix B.

4.5.2 Heat Dissipation

Waste heat from the climber motors, bearings and electronics must be radiated into space. No dissipation due to convection is possible except in the atmosphere. The area and mass of the radiator was calculated based on a motor power consumption of 4 MW. This number comes from previous studies that attempted to find a reasonable power level that was a compromise between the high power needed near Earth and the diminishing power needed at higher altitudes. These studies did not take into account the realistic nature of starting from standstill in megawatt electric motors, so the following calculation of waste heat rejection may be an underestimate.

The area and mass of the heat rejection system required was calculated in the climber cooling discussion in section 2.2.3. For an input heat temperature of 400 K and a motor efficiency of 96%, the radiator area must be 178 m^2 with a mass of 222 kg.

400 K (127 C) is a reasonable temperature at which to operate the fluid recirculation system used to collect the waste heat of the electronics, motors and bearings. A higher heat input temperature would help greatly in reducing the area and mass of the radiator, but is limited by the temperature at which the circulating fluid can operate. 473 K (200 C), for example, may be at the edge of what is possible. Most oil lubricants for bearings and motors cannot be used under these conditions. Repeating the above calculation for 473 K gives a radiator area of 76 m^2 and a mass of 94 kg.

The radiator would be a thin aluminum sheet well-connected thermally to heat pipes and fluid recirculation lines coming from all over the climber. Taking the area

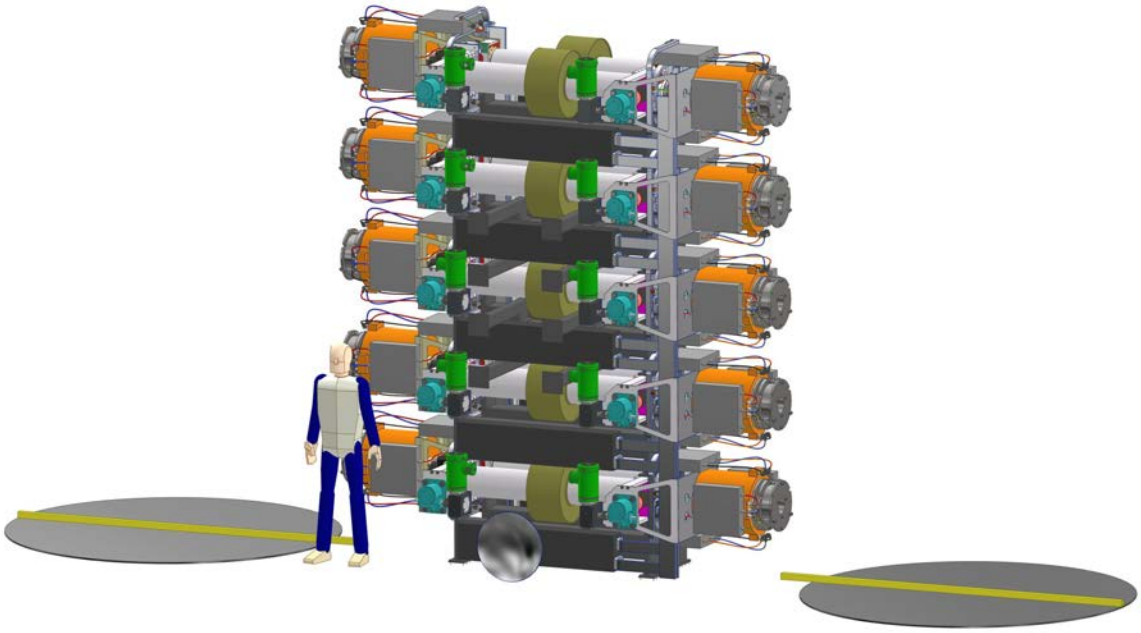

Figure 50: The five-wheel-pair climber

as 76 m^2 and assuming that there are no top or bottom surfaces, the radiator could be a cylindrical shell 3.46 m high with a radius of 3.5 m. This is represented by the blue cylindrical shell in Figure 52.

The shell has to be split and each half attached to a climber half for assembly around the tether. Much work needs to be done to design the piping that takes the waste heat from the climber and distributes it to the radiator. The conversion factor, 1.25 kg/m^2, used to get the radiator system mass includes the mass of the plumbing within the radiator, but not its connection to the climber nor the mass of the recirculating fluid.

Another way to reduce the area and mass of the space radiator is to increase its surface temperature. The motors and electronics should not be subjected to a temperature above 473 K, and might need a lower temperature. In this case, a refrigeration system would be needed that allows the sensitive components to be at a comfortable temperature, but then has a fluid that goes through a phase change to increase the temperature of the radiator surface. This would, in effect, use up some of the power beamed to the climber to run the refrigeration system that would heat up the space radiator. Refrigeration systems are currently being studied to find a system with the highest and lowest temperature extremes.

Figure 53 shows how two climber halves would be separately assembled and brought to the tether for final connection. The presence of the space radiator complicates the order of assembly because the payload tanks are inside the radiator. The thin shell of the radiator would also act as a large sail when the climber is in the

Rank	Part Number	Thumbnail	Unit QTY	QTY	Unit Mass, Kg	Total Mass, kg	% of Total Mass	
1	560 kW motor		1	10	200.25	2002.49	19.1%	
2	MNB_500J_modified		1	10	130.45	1304.49	12.5%	
3	SE-20t AXLE		1	10	109.20	1092.04	10.4%	
4	battery pack		1	10	82.74	827.41	7.9%	
5	SE-20t WHEEL-2		1	10	63.96	639.61	6.1%	
6	PV Array 6 MW		1	2	242.28	484.57	4.6%	60.6%
7	Motor driver electronics box		1	40	12.09	483.77	4.6%	
8	McM 6135K111 AC MOTOR		1	10	38.36	383.59	3.7%	
9	zero-max_l411c		1	5	68.69	343.45	3.3%	
10	JD-WJ2420I2S-001.00-STDX-STDX-X_Jack Housing - 20T_Inverted		1	10	27.66	276.59	2.6%	
11	McM 2721T24_SPHERICAL-ROLLER BEARING		1	20	12.66	253.29	2.4%	
12	zero-max_l582s		1	5	39.52	197.62	1.9%	
13	McM 3540N210 FACE-MOUNT AC MOTOR		1	10	16.63	166.29	1.6%	
14	_0223-07852	*Varies*	1	10	13.54	135.36	1.3%	
15	Belleville Spring		1	240	0.50	120.49	1.2%	
16	Fixed BEARING HOUSING-2		1	10	11.33	113.32	1.1%	
17	SE-04 BEARING HOUSING		1	10	9.94	99.41	0.9%	85.2%
18	SE-04 SLIDE BAR 1		1	20	4.23	84.55	0.8%	
19	JD-WJ2420I2S-001.00-STDX-STDX-X_Screw Inverted - 20T_Type 2 (Load Pad)		1	10	7.91	79.13	0.8%	

Figure 51: Partial table of component masses for the five-wheel-pair climber. Brakes are labeled MNB_500J_modified, Schmidt couplings are labeled zero-max. The percentage of the total climber mass due to each component is highlighted, with the far-right column representing the cumulative mass percentage.

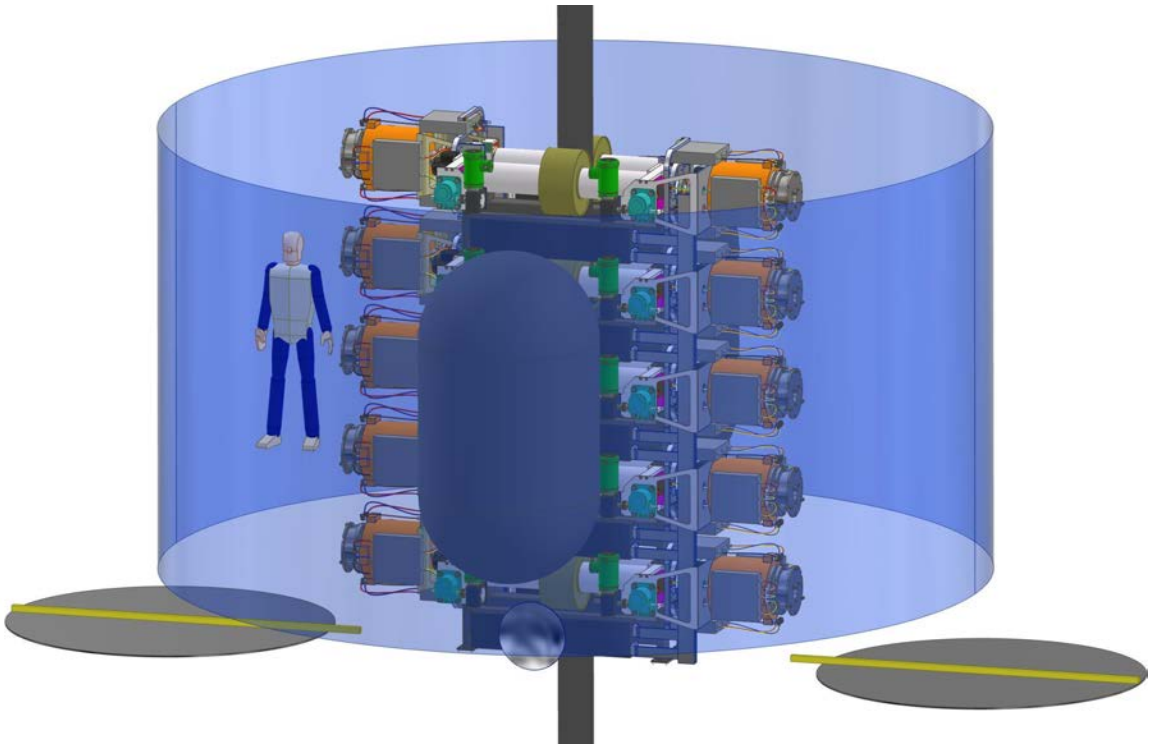

Figure 52: Five-wheel-pair climber with a space radiator surrounding it

atmosphere, making this configuration impractical for travel at low altitudes.

4.5.3 Power Requirements

The current study is not concerned with the type of climber power generation, mainly because there are many options that seem viable. Only the amount of power and its distribution are discussed here. Of course the type of power generation will affect the climber mass.

Given the mass determined in the previous section plus payload, the mechanical power requirements can be calculated for a given velocity profile. Two types of velocity profile, constant power and constant speed, may be considered. With constant speed, the power requirements at Earth's surface are large, tapering to zero near GEO. Constant power limits the velocity near the Earth to small values, but permits large velocities at higher altitudes. A combination of the two options seems to be most efficient: constant power up to a certain altitude and velocity, and constant velocity thereafter. As mentioned in Chapter 2, the climber is designed for a constant mechanical power of 4 MW. Due to motor and drive wheel inefficiencies, the required electrical power will always exceed the mechanical power. From a standing start, the efficiency will be zero, increasing to around 96% at its highest. Thus, much more electrical power than 4 MW will be required during lift-off. The actual value will

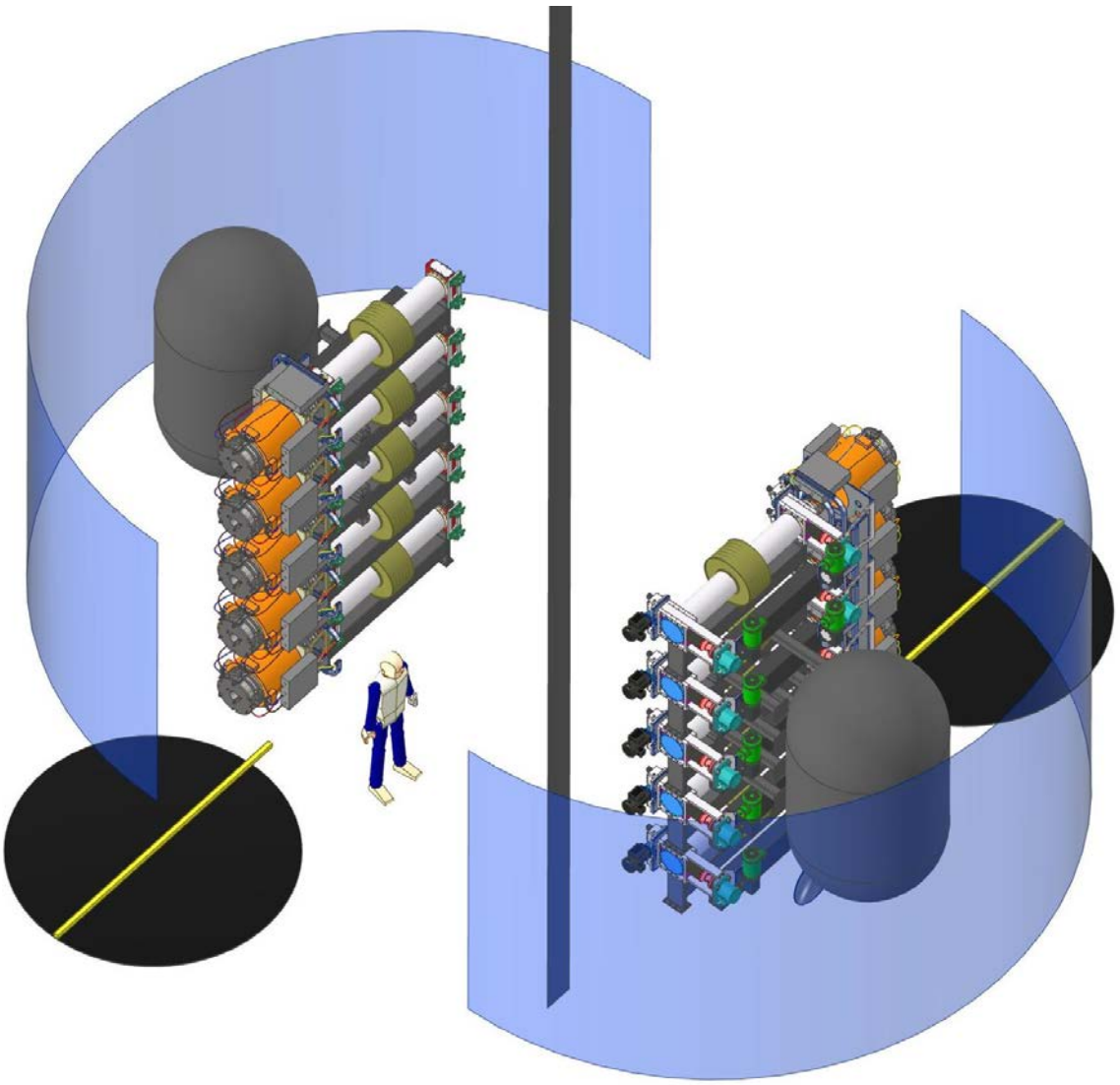

Figure 53: Climber halves brought to the tether for final assembly

depend on the efficiency as a function of altitude which in turn depends largely on the torque required and the motor characteristics.

4.6 Summary

A conceptual design for the space elevator climber was developed based on the following assumptions:

- the existence of tether material with tensile strength greater than 100 GPa, shear strength greater than 9 GPa and coefficient of friction greater than 0.1
- pinched-wheel friction drive
- operation mostly in vacuum
- only today's technology to be used for climber components
- 20,000 kg total mass of climber
- 4 MW maximum mechanical power for climbing
- 8 days travel time from Earth's surface to GEO

The design process was iterative. The starting point was a climber with ten wheel-pairs, using a commercial available electric aircraft motor on each wheel. As the necessary climber systems were developed and corresponding masses were calculated, the total mass exceeded the 20,000 kg limit, even assuming no payload.

Because this climber could not lift itself, the assumptions about the motors were changed; it was found that electric motors with twice the available torque per mass could be produced today. With this, and a reduction from ten wheel-pairs to five, the next iteration was undertaken. The resulting new climber had a tare mass of 10,622 kg (10,528 kg for drive train and chassis + 94 kg for a radiator), leaving 9378 kg for payload to make up the 20,000 kg total climber mass. Some of the payload could be used to transport about 5000 kg LOX, for example.

The five-wheel-pair climber represents one point in the multi-dimensional design space. Optimization of the payload to total climber mass ratio will require varying many parameters and perhaps some of the above assumptions, but it seems likely that a 20 t climber will eventually be able to lift 14 t of payload.

5 Projected Improvements

The study identified a number of areas in which improved technology would enhance the ability of the space elevator to carry payload. These improvements can be made with technology that exists or is likely to exist in the next decade. Areas of research which underpin the anticipated technologies were also identified and will be discussed in Chapter 6.

5.1 Tether Material

The pace of development in the world of graphene and other two-dimensional (2D) materials has been astonishing. Prior to 2004 graphene was considered purely theoretical. Since then, graphene has moved from the laboratory to industrial scale manufacturing, it can now be made in lengths of up to one kilometer and at speeds of two meters per minute. This material is polycrystalline and contains defects which limit its use for high-strength applications; it is not tether-quality material yet.

This progress of industrial manufacturing of graphene is not limited to one location or organization. At least three separate organizations in Asia and North America have publicly declared their development work. There are other organizations actively involved in making tether-quality material and have asked not to be named.

The successes in manufacturing graphene could prompt other researchers to revisit the manufacture of carbon nanotubes, hexagonal boron nitride (hBN) nanotubes and also hBN super laminate.

This pace of development seems set to continue, and it is reasonable to assume that high quality GSL material suitable for the tether will be made within the next decade.

5.1.1 Coefficient of Friction

The current study has revealed that measuring friction is not as straightforward as it might first appear. The peer-reviewed literature contains a wide range of values for the coefficient of friction for the candidate tether materials.

This variation is partly due to limitations of the measurement techniques as small samples of material are generally used. The study also came to the view that a meaningful measure of friction is best performed using the same materials that will be used for the tether and the climber wheel surfaces.

As far as can be determined, no study investigating the friction between titanium and GSL has been performed. This should be possible in the foreseeable future as material samples become available. The authors encourage researchers to perform these tests and make their results public.

5.1.2 Shear Strength

The mechanical stresses between the climber and tether also indicated that there will be significant shear forces on the tether. A tether made of layers of 2D material or braided nanotubes will need to withstand these forces. The layers in a 2D material are held together by Van der Waals forces. Experimental evidence for the behavior of these layers under shear is very limited. This study has also found that computer modeling of the Van der Waals force needs much more work and researchers are encouraged to direct effort in both these areas in the coming years.

5.2 Climber Improvements

Chapter 4 identified high-torque, low-mass electric motors as being the key to reducing drive train mass and increasing payload. Large torques require large currents which in turn require a large heat rejection capability and a subsequent increase in non-payload mass. Motors with higher torque to mass ratios or superconducting motors may address these issues.

The substitution of lighter materials for heavier ones was also mentioned as a way to increase the payload to total climber mass ratio. CFRCs can be used in many cases, but even greater advantage may be drawn from GSLs when they become available.

Smaller climber wheels could reduce torque requirements but the current climber design is already tightly packed, making any reduction in wheel radius unlikely. Miniaturization of climber components would be very useful.

5.2.1 High Torque Motors

High-torque, low-mass electric motors were found to be the key to building a climber that can lift itself and payload. The conceptual design used Helix motors which are reported to deliver 5600 N m of torque and have masses around 200 kg. To increase climber payload beyond the current 9 t value, the state of the art of electric motors must be extended. With proper design, this is possible using today's technology.

Producing More Power with Less Mass

The torque density of an electric motor can be increased by using stronger magnets, adding pole-pairs, reducing the gap between the rotor and stator and increasing the current-carrying capacity of the windings. Permanent magnet synchronous motors have many of these features and are known for their high torque and power densities.

This type of motor is the basis for a climber motor design using 28 poles of neodymium N55 magnets. These are the strongest, commercially available permanent magnets and, coupled with the large number of poles, would produce a high field, and therefore torque. The 28-pole design would allow a decreased rotor-stator gap which

not only increases torque density but also increases power transfer efficiency.

Substituting more specialized materials for common motor components would also increase torque density. Silver windings, for example, would have 7% more current carrying capacity than copper. The rotor could be manufactured from Metglas instead of iron. It has a magnetic permeability about five times that of iron and would help to reduce heat generation and power loss.

Space-worthiness

Electric motors for aerospace applications cannot operate at altitudes above about 11 km. Because they assume fanned air for cooling and liquid lubricants for bearings, they cannot be used in space without modification. Any high-torque electric motor to be used on the climber will have to operate most or all of its lifetime in space.

Ceramic bearings may be a solution to the lubricant problem. Having a lower coefficient of friction than steel bearings, ceramic bearings develop less heat and therefore do not require lubricants for heat dissipation. They are also able to tolerate wider variations in temperature, being able to operate at temperatures up to 1270 K. Although they cannot exceed 90% of the rated speed of stainless steel bearings, they can easily achieve 5000 RPM, which is more than required for the climber discussed in this report.

A greater challenge is to dissipate heat in vacuum, where radiation is the only method. A motor could be built with a non-finned, gas-tubed housing which would absorb generated heat from the inner motor and use a refrigerant to transfer the heat to the climber radiator. This system would have to maintain a temperature below 430 K in the inner motor.

5.2.2 Superconducting Motors

Research is ongoing in this area. A recent report (Ren et al. 2015) showed that field strengths of ten T (Tesla) at 30 K are feasible using YBCO, a popular high-temperature superconductor (HTS). For comparison, a conventional electromagnet will deliver about two T. Moreover, the conventional electromagnet will have a core made predominantly of iron, whereas an HTS magnet will have a vacuum core and so will be very much lighter.

A superconducting motor requires alternating current, and there will be other factors limiting the available field strength, but it is reasonable to expect that two to three times the torque can be delivered compared with existing motors, and the power losses will be lower, though there will still be some. The combination of these factors means that fewer, lighter motors can be used compared to those commercially available today.

A Korean study shows that an HTS motor with a torque of 3315 N-m is feasible (Le et al. 2020). The motor mass is 134 kg, including the cooling equipment – cryostats – which comprise 11% of the total mass; it may be wise to assume a somewhat greater total mass of perhaps 200 kg. The power is 2.5 MW, and the maximum speed is

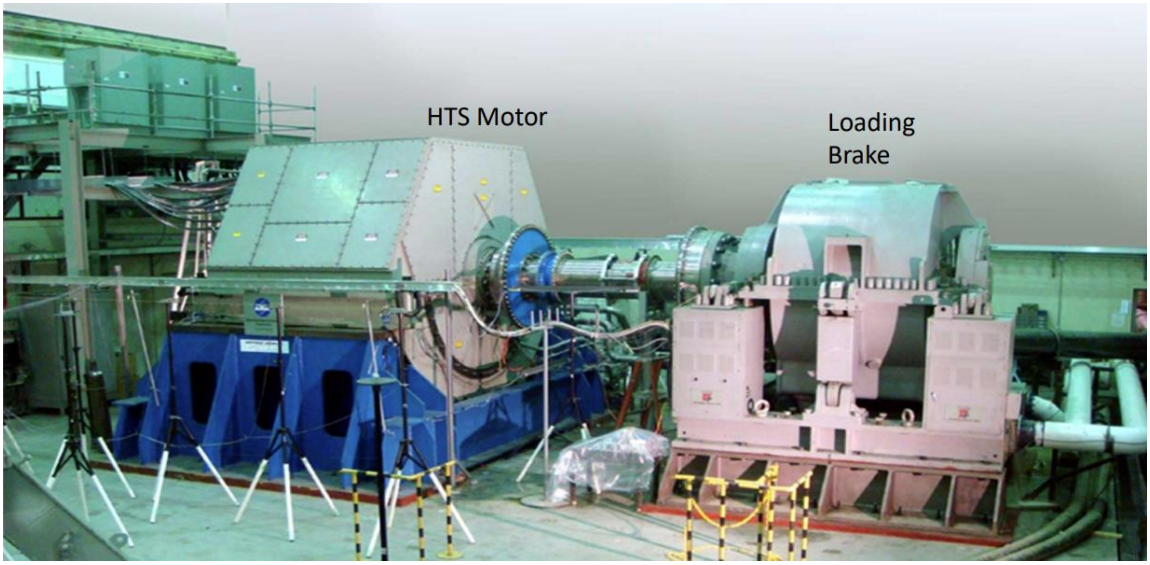

Figure 54: Alsthom's 36.5 MW marine engine

7200 RPM. With a wheel of 15 cm radius, the lifting force would be about 22 kN or 2.25 tonnes. To lift a 20 t climber, nine motors would be needed weighing 1.8 t. There would be plenty of power, and the maximum climbing speed would be $7.2 \times 60 \times 2\pi \times 0.15 = 400$ kph. Perhaps a more optimal design is possible using eight motors at somewhat lower speed. Then two pairs of wheels, each pair having four motors, would be sufficient.

General Electric built and successfully tested an HTS 1.3 MW generator in 2013 (GeneralElectric 2013). It demonstrated the feasibility of HTS technology in commercially scaled applications. Alsthom Electrical Machines built a 36.5 MW HTS marine engine (Figure 54) which was successfully tested on land by the US Navy (Gamble et al. 2011).

Airbus has announced plans to build and test prototype aircraft engines using HTS (Airbus 2021). They have set a target date of 2023 to give the results. They expect weight and electrical losses to be halved compared to their existing electric aircraft.

Cooling

All motors require cooling, and in space only liquid cooling and radiative cooling are possible. Superconductors require cooling, but they have the benefit that they generate much less heat than conventional conductors. Direct current in a superconductor generates no heat, but there are losses due to alternating current, which is normally required in electric motors.

The James Webb space telescope is maintained at a temperature of 40 K (-233 C) to enable it to perform infrared observations (NASA 2022). It uses a heat shield of area 300 m^2 consisting of five layers of Kapton coated with aluminum (see Figure 55). The calculated mass for this is 13.7 kg. To this must be added spacers, which can

Figure 55: Sunshield for the James Webb Space Telescope

be very light, and a strut to support the modest weight. A popular spacing method is to use balloons inflated with helium at very low pressure, so that they expand in the vacuum of space. These would bring the total mass to about 20 kg. More mass would be needed to operate at or near 1 g.

It would be reasonable to add a layer of thin-film photovoltaic cells to the sunshield, which could provide a useful auxiliary supply of power up to 60 kW.

The sunshield keeps the temperature down to 50 K, which is cool enough for HTS materials to maintain a magnetic field strength of about 3 T. Although YBCO will operate at 77 K, it is at field strengths of about 0.6 T. For best results, active cooling will be required. Cryostats that cool to 40 K in ambient conditions on Earth are readily available. It would be worth commissioning a special purpose cooler for space-elevator climbers, possibly based on the design used for the mirror in the James Webb telescope.

Reliability

The big issue with superconductors is reliability; they tend to quench. Once their temperature rises, for whatever reason, they lose their superconductivity and may then suffer damage if high currents are flowing. Until this problem can be solved and reliability is demonstrated, they are not practical for applications like the space elevator where continuous operation for at least a week is required.

5.2.3 Lighter Materials

Where possible, CFRCs were used to replace aluminum alloys in the conceptual climber design in order to reduce overall mass. It is clear that any of the new, strong, low density materials, CNTs, hBN or GSL, would further reduce mass in most climber subsystems, provided it is proven that they can be used as structural materials. While the tensile and compressive strengths of GSL, for example, appear to be very good, its shear strength is lacking.

Assuming its shear strength can be improved as discussed in Chapter 3, GSL could replace CFRCs as the structural and interconnecting material. The additional mass reduction, however, would be marginal compared to mass reductions possible in other subsystems.

According to the bill of materials for the five-wheel-pair climber (Figure 51), the drive motors are the single most massive component of the climber, accounting for about 19% of the total mass. Noting the excellent conductivity of GSL in Table 6, it seems possible that at least the windings of the motors, and maybe the housing, could be made of GSL which has a density of 2.26 g/cm^3. For a permanent magnet motor with metglas windings and aluminum housing, about 35% of the mass is due to the winding and 20% is due to the housing and other structural elements. Using 7.9 g/cm^3 as the density of metglas and 2.7 g/cm^3 as the density of aluminum alloy, the mass of a 200 kg motor would be reduced by about 60 kg by using GSL. The non-payload mass of the five-wheel-pair climber would then go from 10,600 kg to 10,000 kg.

Two other massy components are the titanium alloy drive wheels (6.1% of the total mass) and the aluminum axles (10.4%). For the wheels, compressive and shear strengths are the critical parameters. A comparison of Tables 1 and 3 shows that GSL would have $14/0.88 = 15.9$ times the compressive yield strength of Ti-6Al-4V. Assuming that the shear strength of GSL can be brought up to the 9.08 GPa required by the tether, it would have $9.08/0.55 = 16.5$ times the shear strength, making GSL an excellent candidate for the wheel material. The mass savings of this replacement would be 321 kg.

The above values for compression and shear in GSL would be more than adequate for the axle material. In addition to these, bending must also be considered. GSL is expected to be quite stiff. Its Young's modulus is much greater than that of Al 6061-T6, indicating a high resistance to bending. Provided GSL is not too brittle, it could replace aluminum in the axles with a mass savings of 178 kg. This mass-saving exercise could likely be repeated for many other climber components.

Before GSL could be used in this way, several issues would need to be investigated. Fabrication of cylinders and wheels with cutouts may prove to be a problem. In this report only layering of 2-D materials to make flat ribbons has been considered, but perhaps a wrapping of GSL layers into hollow cylinders could be made to serve as an axle. With no large samples of GSL available, it is not currently known how cutting of this material would proceed. Also unknown is how GSL fabrications would behave

under rotational stress and fatigue.

6 Proposed Research

6.1 Molecular Modeling

The macroscopic properties of graphene and GSL of most interest in the construction of a space elevator tether are: the coefficient of friction between graphene sheets and between graphene and other materials, the multi-axial tensile, shear and compression strengths of single and multiple graphene layers, the formation of defects and their propagation, the adsorption of gasses, the effects of pressure and temperature and the effects of the various stacking configurations of graphene sheets.

In the absence of measurement, molecular modeling must be used to predict these properties. Modeling includes the specification of the molecular structure and the calculation of its dynamics, that is, the state of the molecule as a function of time. From this, the forces on atoms, the effects of pressure and temperature, possible failure modes and so on, can be predicted.

Molecular modeling is a broad and primarily computational area of research consisting of many theoretical approaches depending on the application. In the case of graphene, the behavior of large molecules under various conditions is desired. For such large molecules, the classical molecular dynamics approach is preferred over the quantum mechanical because it can handle a larger number of atoms ($\sim$100,000) and takes less CPU time. Graphene is not a simple molecule, though, so a quantum code may eventually be required.

Software Packages

Three classical software packages that may apply are SAMSON (SAMSON 2022), LAMMPS (LAMMPS 2022) and GROMACS (GROMACS 2022). The quantum mechanical code VASP (VASP 2022) might also be used. These packages allow molecules to be built and simulated using molecular mechanics and dynamics. Individual atoms can be moved around, removed or added to existing molecules. For example, one layer of graphene can be moved with respect to an adjacent one. Various temperatures and pressures can also be applied to the modeled sample. When such changes are made, the codes do automatic force minimization to get the lowest energy configuration.

Classical calculations model atoms as mass points and the bonds between them as springs. Non-bonded forces such as Coulomb and Van der Waals are also modeled. These are summed to create a potential from which forces are derived. Each of these codes provides or allows for different types of interaction models or force fields. Force fields are required in order to describe the interaction between atoms and to calculate the forces and energies in the system.

SAMSON, for example, can use the Brenner force field model (Brenner et al. 2002) which simulates bond formation, breaking and reactions. This would be particularly useful in studying the formation of the sp3 bonds required to spot-weld together layers of graphene within GSL. It could also help to understand how defects and tears in

large graphene sheets form and spread under stress. Ideally, this would provide an indication at the molecular level of when macroscopic failure was about to occur.

GraFF (Forcefield for Graphene and Graphite) (Sinclair et al. 2018) is an interaction model to be used with LAMMPS. It was developed to address problems with existing simple Lennard–Jones potentials in representing graphene–graphene interactions. A typical problem for many molecular modelers is poor Van der Waals interactions which often lead to incorrect potential energy surfaces. GraFF has purpose-built Van der Waals interactions based on the Lennard–Jones potentials. This is important for studies of friction between graphene sheets or other materials because friction arises from the Van der Waals interaction. GraFF can also calculate the sustainable shear stress in GSL. One caveat here is that the Lennard-Jones potential will work for carbon, but it is not known yet if it works for hBN.

In the quantum mechanical approach, calculations are based on either Hartree-Fock methods or density functional theory. The Hartree-Fock method is a means of approximating the wave function and the energy of a quantum many-body system. It is used to solve the Schrodinger equation for atoms and molecules.

Density functional theory (Hohenberg & Kohn 1964) (DFT), is also an approximate method in which the electron density is the fundamental property, instead of the wave function. It allows the interaction potential of an N-electron system to be expressed as the sum of N single-electron potentials, thus greatly simplifying the calculations. Being an ab initio theory, material parameters are not required as input.

VASP is a simulation package for materials modeling which can calculate electronic structure and quantum molecular dynamics from first principles. It can calculate internal forces and stresses, response to ionic displacements (elastic constants) and response to electric fields such as dielectric properties.

A Possible Approach to Modeling Graphene and GSL

The modeling of graphene and GSL would probably best be approached by a hybrid quantum-classical calculation. A quantum calculation would be most accurate, using Schrodinger's equation and DFT. It is, though, CPU intensive and usually cannot accommodate large numbers of atoms. The modeling would probably start with a Hartree-Fock calculation, as this is a detailed quantum-mechanical approach. Only 30 to 50 atoms could be modeled, but it would tell us what approximations could be made in going to larger structures. It could be used to develop a DFT for graphene, which could then be used in the classical calculation to minimize the potential energy in order to get the molecule's ground state and compare to other states. Doing the rest of the calculation with the classical GraFF code would allow orders of magnitude more atoms to be simulated with a smaller expenditure of CPU time. It is also possible that a machine learning approach could be used, which would blend the classical and quantum approaches.

The initial model development may still be very CPU intensive and require a supercomputer. However, once the model is developed, the dynamics calculations

could be performed on personal computing devices.

6.2 Material Properties

Only a few basic tether material properties, summarized in Appendix D, are known at this time. This state of affairs will soon change as new measurements and experiments appear, but for the time being, scalar parameters like tensile strength, shear strength, coefficient of friction, heat conduction and electrical conduction must suffice for all designs and calculations pertaining to the climber-tether interface. It was assumed in this report that the above parameters are isotropic, that is, their values do not depend on the directions of forces in the tether and at the interface. This will certainly not be the case for any of the candidate tether materials, but is assumed to be so due to the lack of anisotropic measurements.

The nature of the anisotropy in these materials can be guessed based on the molecular structure and the way in which the molecules are assembled to form the tether, but measured values are essential. The most-needed measurements and proposals for how these might be obtained are listed below.

6.2.1 Anisotropic Parameters

Anisotropic material parameters depend on the direction of forces in the material. If the material is isotropic, one parameter is sufficient to describe, for example, tensile strength. The material can be treated as uniform in all directions. A non-uniform material will respond differently to forces in different directions and in general will require many more parameters to describe the response.

A fully anisotropic material requires 21 independent parameters to describe, say, its elastic response. However, most materials have symmetries which greatly reduce the number of parameters needed. Laminates, for example, exhibit transverse isotropy in which the material is isotropic in the plane of the layer, but not in the direction perpendicular to the layer. Such materials require only five parameters to describe the response. In orthotropic materials there are three mutually perpendicular directions in which the properties are different. Wood is a good example of this, having symmetry about the ring axis, along the grain and along the ring radius. Nine parameters are required for such materials.

Graphene super-laminate (GSL) may be likened to thin layers of honeycomb glued together in a stack. The honeycomb cell structure is known to be transverse isotropic (Gibson & Ashby 1997), so the stack must be also, as long as the layers are aligned in certain ways. In Section 3.4.2, the concept of cross-bonding the molecular layers in GSL was discussed as a method of improving its shear strength. Assuming that the cross-bonds are made at regular intervals along the length of the layer, another anisotropy will be introduced perpendicular to both the thickness (the stacking axis) and the width of the layer. GSL thus modified becomes orthotropic.

The parameters for orthotropic GSL can be specified using the coordinate system

of the tether. The z axis is taken along the stacking direction which is also the thickness direction of the tether. The y and x axes run along the width and length, respectively, of the GSL layer and correspond to the width and length of the tether. For an orthotropic material the response to a force (generalized Hooke's law) can be given by

$$\begin{bmatrix} \epsilon_{xx} \\ \epsilon_{yy} \\ \epsilon_{zz} \\ \epsilon_{yz} \\ \epsilon_{zx} \\ \epsilon_{xy} \end{bmatrix} = \begin{bmatrix} \frac{1}{E_x} & -a_{xy} & -a_{zx} & 0 & 0 & 0 \\ -a_{xy} & \frac{1}{E_y} & -a_{yz} & 0 & 0 & 0 \\ -a_{zx} & -a_{yz} & \frac{1}{E_z} & 0 & 0 & 0 \\ 0 & 0 & 0 & \frac{1}{2G_{yz}} & 0 & 0 \\ 0 & 0 & 0 & 0 & \frac{1}{2G_{zx}} & 0 \\ 0 & 0 & 0 & 0 & 0 & \frac{1}{2G_{xy}} \end{bmatrix} \begin{bmatrix} \sigma_{xx} \\ \sigma_{yy} \\ \sigma_{zz} \\ \sigma_{yz} \\ \sigma_{zx} \\ \sigma_{xy} \end{bmatrix} , \tag{66}$$

where

$$a_{xy} = \frac{\nu_{xy}}{E_x} = \frac{\nu_{yx}}{E_y} , \qquad a_{zx} = \frac{\nu_{zx}}{E_z} = \frac{\nu_{xz}}{E_x} , \qquad a_{yz} = \frac{\nu_{zy}}{E_z} = \frac{\nu_{yz}}{E_y} .$$

The left-hand column vector contains the normal and shear strains and the right-hand column vector contains the normal and shear stresses. The parameters that must be measured are the Young's moduli, E_x, E_y and E_z, the shear moduli, G_{yz}, G_{zx} and G_{xy}, and the values a_{yz}, a_{zx} and a_{xy} which are the Poisson's ratios ν divided by the Young's moduli.

Electrical conductivity is likely to exhibit anisotropies as well. Each graphene layer within GSL will have a hexagonal array of sp2 electron orbitals above and below its central plane, leading to metal-like conduction in the $x - y$ direction. Perpendicular to the $x - y$ plane, Van der Waals bonds between the layers are unlikely to support a high conductivity. Hence, conductivity in at least two directions will have to be measured.

It is unclear how many heat conductivity parameters will need to be measured. Phonon propagation, important at shorter wavelengths, depends on the molecular structure of GSL and will probably lead to directional heat propagation. In that case, conductivities in the $x - y$ plane and in the z direction will need to be measured. For heat of longer wavelengths, the molecular structure will not be important and one parameter will be sufficient.

The mutual coefficient of friction between the tether material the wheel material will likely be isotropic in the $x - y$ plane of the tether, so only one parameter needs to be measured in this case.

6.2.2 Measurement and Testing

Mechanical Properties

For a hypothetical cube of GSL, say 5 cm on a side, obtaining the nine values above would be straightforward: strain gauges on each face would record the responses to tension, compression and shear forces applied by standard testing machines.

An actual sample of tether material, however, would have a thickness of only about 10 μm, with some samples as thin as a few nm. 10 μm samples, which would still have widths and lengths of the order of cm, pose no problem for the above method as long as measurements are restricted to the $x-y$ plane. Strain gauge rosettes applied to this surface could still provide E_x, E_y, G_{xy}, ν_{xy} and ν_{yx} in response to testing machines which grip and pull along the edges of the samples. The remaining parameters, though, could not be obtained in this way because of the small z dimension of the sample.

E_z could be determined by a cantilever bending of the sample in the z direction. The shear moduli could be provided by torsion tests, in which parallel edges of the sample are gripped and twisted along one of the sample's principal axes (Lempriere et al. 1969). The remaining Poisson's ratios could be obtained by measuring the curvatures of micro-machined cantilever plates of GSL (Krulevitch 1996).

It is difficult or impossible to grip, pull or twist very thin samples without destroying them. Samples would have to be free-standing, mounted or deposited on substrates, or supported in liquid. One method for unsupported thin films could, in principle, measure E_x, E_y, ν_{xy} and ν_{yx} by laser light diffracted from a grating deposited on the sample (Ruud et al. 1993). Another method uses an ultrasonic micro-spectrometer (Tsukahara et al. 1990) in which acoustic waves are focused on a sample which is immersed in water. The reflected waves are analyzed to extract the orthotropic parameters. Using this device all nine parameters were extracted for a 12 μm thick sample (Okabe et al. 1999).

The nine orthotropic parameters describe only the elastic response of the material. It will also be necessary to measure the full stress-strain curve in order to understand where the elastic region ends and where the yield and breaking points are. Graphene is thought to be near the boundary between a ductile and a brittle material. GSL may or may not have the same behavior.

Electrical and Thermal Properties

Electrical conductivity in the tether is not particularly important at the interface between the climber wheels and the tether material, but it is important in determining the response of the entire space elevator to electromagnetic fields and currents in the atmosphere and space. In this case, the values for in-plane and out-of-plane conductivity are required. Some methods for these measurements are summarized by Rojo et al. (2015). The in-plane measurements involve four probes attached by lithography to the sample at various points. The out-of-plane measurements involve etching the sample, depositing the sample in a mesa-like pattern or placing several

probes on the upper surface of the sample and a single large probe on the bottom. The latter method would appear to be most appropriate for GSL.

Values for the in-plane and out-of-plane thermal conductivity are also required. These values are of interest mainly for heat conduction from the wheels into the tether and subsequent dissipation into space. Also, should GSL eventually be used as a radiator material, both in-plane and out-of-plane values will be required for any design. The preferred method for such measurements is transient thermo-reflectance, which depends on the optical reflectance of a material being proportional to the surface temperature of the sample. A variant of this method was carried out for highly oriented pyrolytic graphite (Rodin & Yee 2017) which is an in-plane conductor and an out-of-plane insulator. The same test may therefore be appropriate for GSL.

Friction

The coefficient of friction (μ) is a function of the surface conditions of the two materials in contact. The values quoted in this report result from diamond-tipped probes being dragged across samples of graphene, so the value of μ is strictly only valid for diamond on graphene contacts. What is actually needed is the value for the wheel material (titanium) on graphene or GSL. The atomic force microscopes (AFM) used to measure friction on thin samples can be equipped with metal-coated tips (Xu & Liu 2022) so that not only Ti-GSL coefficients, but other metal-GSL coefficients, may be measured. When GSL samples, larger in both thickness and area, are produced, slip testing devices (Gao 2015) can be used to measure the friction. Here, a sample of one material is dragged across a rigid, fixed plane of another material.

Material Characterization

When GSL is produced it will be necessary to verify that layers of single crystal graphene are being produced and not polycrystalline graphene. The clearest proof of this is the absence of the grain boundaries found in polycrystalline graphene. It will also be essential to demonstrate a low level of defects or impurities in the single crystal graphene planes and in the bonds holding the planes together. These tests can be performed by Raman spectroscopy in which laser light inelastically scattered from a sample provides structural detail of molecules in the material. Raman spectroscopy has already been used for determining grain size, characterizing sp2 and sp3 bonds and determining the number of layers in multi-layer graphene (Barron 2015). It should therefore be an ideal tool for the evaluation of the quality of GSL.

6.2.3 Summary of Required Measurements

The following parameters will need to be measured for GSL before a detailed design of the tether and climber can be made:

- Elastic response parameters
  - Young's moduli along principal material axes: E_x, E_y, E_z

  - Shear moduli: G_{xy}, G_{yz}, G_{xz}
  - Poisson's ratios: ν_{xy}, ν_{yz}, ν_{xz}
- Stress-strain curve from zero to breaking stress
  - tension, σ_{BS}
  - shear, τ_{BS}
  - compression
- Electrical conductivity: in-plane κ_{xy} and out-of-plane κ_z
- Thermal conductivity: in-plane λ_{xy} and out-of-plane λ_z
- Coefficient of friction with titanium μ
- Material characterization: absence of grain boundaries, absence of defects, number of layers

6.3 Climber Redesign and Trade Study

6.3.1 Improved Design

The climber design of Chapter 4 was based on the use of commercially available components. Given advancing technology, it is relatively safe to extrapolate stronger, lighter components becoming available in the near future. These would significantly reduce climber mass and make new design choices possible.

Also affecting the design were assumptions about the mass throughput of the space elevator, the scaling of the climber mass with its dimensions, whether or not to operate in the atmosphere, methods of heat dissipation and methods of power transmission to the climber. All of these are higher-level options not strictly determined by physics or engineering, but also by economics and a lack of detailed knowledge as to what is possible. Of these, only the throughput assumptions are included in the trade study discussed here, but the others could be included in more general studies.

6.3.2 Trade Study

Finding the best set of parameters for the space elevator system is an exercise in multi-dimensional optimization. Even for a subset of the entire system, such as the climber-tether interface, the number of parameters defining it is large and to settle on an optimal set is a difficult undertaking. The parameters in this multi-dimensional space must be varied and traded against one another, hence the term "trade space".

Formal procedures exist to guide the optimization process. These are discussed in Appendix C and summarized here.

The purpose of a trade space analysis is to understand the critical components, explore the relationships between them, and apply value to those relationships in a way that facilitates informed decision making. The three primary components that make up trade space analysis are (DefenseAcquisitionUniversity 2022): physical characteristics, capability attributes and applied utility value or priority. The balance of all three of these is the basis of the decisions.

A trade space analysis should answer three primary questions (Brantley et al. 2002): what is in the trade space; how are the effects of the trade space elements characterized; and when and how decisions should be made. The first step is to define the problem and construct the trade space. Then the essential trade space interactions must be determined, that is, what are the entities to be traded. Consistent decision criteria and metrics must then be established for each trade space entity. Finally a trade-off methodology must be developed.

The current study has uncovered numerous uncertainties when designing the tether, the climber and the interface between the two. In order to design and build an operational, viable space elevator system, the following provides potential areas for trade-space analysis.

Tether Material

Numerous trades of tether material parameters and conditions are defined here. One of the parameters is flexibility. The flexibility and rigidity scale goes from 1(not rigid) to 5 (very rigid).

- temperature (°C) vs expansion (mm)
- layers vs. strength (N)
- carbon nanotubes vs. graphene vs. other viable materials
  - strength (N), Flexibility (1-5), Tubular vs Ribbon Cable
  - stiffness (N-m/radian) vs. rigidity (1 to 5)
  - binding energy (eV) of multilayer graphene
  - electrical conductivity (A) vs time (s)
  - tensile strength (N) vs load vs time (s)
  - fracture evaluation vs time (s)
  - friction vs multilayer graphene vs load
  - yield strength (N) vs. load (kg) vs time (s)
- analysis of various Graphene Samples (SG400, SG2000, SG2800)
  - temperature (°C), flexibility, strength (N)

  - thermal conductivity (W/m/K) vs. slope of curve vs. time (s)

Tether

These trades deal with tether configuration issues.

- single vs. multiple tethers (length-m)
- straight vs. looped (connection to Climber)
- max stress (MPa) vs load (kg) vs length (m)
- max pressure (MPa) vs load (kg) vs length (m)

Climber Motors

Several of the trades here involve climbability which is the set of conditions that must be satisfied in order for climbing to be possible.

- number of motors vs climbability
- power (kW) vs climbability
- wheel mass (kg vs climbability)
- stress (MPa) vs motor speed (rpm)
- power consumption (kW) vs number of motors per climber
- motor drive types vs load (kg)

Climber Wheels

- temperature (°C) vs. stress (MPa)
- wheel diameter (m) vs climbability
- friction (N) between wheel and tether vs speed (rpm)
- yield strength (N) vs Stress (MPa)
- yield strength (N) vs flexibility(m/N), hardness (1-5), load capacity (kg)
- wheel radius (m) vs load (kg) vs climbability
- min/max torque (Nm) vs wheel diameter (m) vs load (kg)
- number of wheels vs load (kg) vs climbability
- wheel material vs stress (MPa) vs density (kg/m^3)

Climber-Tether Interface

- climb duration (s) vs altitude (km) (atmosphere, space)
- friction force (N) vs load (kg) vs time (s)
- temperature (°C) vs location (km) vs time (s)
- min/max stress (MPa) vs load (kg) vs time (s)
- contact length on tether (m) vs Young modulus vs Poisson's Ratio vs stress (MPa) vs torque (N-m)

7 Summary

The conditions at the climber-tether interface, established in Chapter 2, set physical requirements for the space elevator tether, a wheeled climber and the region where they make contact. Design considerations for both the climber and tether indicated the need for future developments. These requirements are listed here.

7.1 Climber

A conceptual design of the space elevator climber came to the following conclusions.

With the availability of space-worthy motors and bearings, a climber could be built with today's technology.

The conceptual design used motors and bearings designed for use at 11 km and below. Above that, space-rated versions would need to be used which do not yet appear to exist. Once they become available, a 20 t climber could be built with frame, drive train and support systems massing about 11 t, leaving 9 t for payload. The postulated 20 t climber with 14 t of payload cannot yet be built, but anticipated advances in materials and electric motor technology could make this possible in the near future.

More high-torque motor development is required.

The recent development of high-torque, low-mass electric motors make possible the construction of the climber from the conceptual design. Further increases in the motor torque to mass ratio are needed and indeed likely, with designs already underway.

7.2 Tether

The state of the art in strong materials production has advanced rapidly in recent years. It is likely that materials satisfying the requirements of a space elevator tether will become available in the near future. The requirements, as established by the climbability conditions, are listed here.

The coefficient of friction of GSL must be increased.

The coefficient friction for graphene and therefore GSL is between 0.03 and 0.1. In order to increase the efficiency of a gripping wheel drive, this must be increased. Two methods were proposed which could double this value: adsorbing hydrogen onto the surface and using hexagonal boron nitride bonded to the outer graphene layers.

The shear strength of GSL must be increased.

While the tensile strength of GSL is sufficient to support the mass of a tether and its climbers, its shear strength is not. The shear may be increased by the cross-bonding the graphene layers using high pressure to convert some of its carbon sp2 bonds to the "diamond" sp3 bond.

Molecular modeling is needed.

Whether the above two proposals will work must of course be tested in the laboratory. Before that, however, molecular modeling of layered 2-D materials could guide improvements to the improved material production process.

More research is required into production of high-strength materials.

The key to the construction of the space elevator is the availability of a large amount of strong materials of sufficient length. Many methods of fast production are now being developed, but to date, none have achieved the length or rate required. At this time, there are no known physical limitations to large increases in the GSL production rate, so the outlook remains optimistic.

7.3 Interface

The effects of the high temperatures and pressures on materials at the interface between tether and climber are largely unknown. While the proposed climber material properties are understood, those of the tether and any new materials that might be used in the climber need to be studied.

Orthotropic material properties of strong materials must be measured.

GSL is likely to be an orthotropic material, so its nine elastic response parameters must be measured. Anisotropies in the electrical and thermal properties of GSL also need to be measured. The same may well be required for other strong materials.

Testing of materials under interface conditions must be done.

Tests specially devised for multi-layer two-dimensional materials must be performed. These include quality control issues such as the absence of domain boundaries, defects in the crystal lattice and intercalated gasses. Response to heat, cold and total combined stress must also be tested.

A trade study is required.

An optimized design of the tether and climber will require trade-offs within components of each and across the interface between them. Once ranges for the above parameters are determined, well-known trade methods can be followed to choose the best values.

7.4 Challenges and Prospects

Within the last decade, advances in strong materials and electric motor technology have made friction-based tether climbing feasible. While it was shown here that a climber could be built today which could lift itself and a payload, a number of challenges were identified. Proposals to overcome these challenges for both the tether material and the climber have been made. Given these, no roadblocks to space elevator tether climbing have yet been found.

Acknowledgements

The authors wish to thank the following people for their preliminary review of the manuscript and helpful suggestions:

Isha Parvaiz, King's College London Space Society

Fedor Sulitskiy, King's College London Space Society

Dr. Bryan Laubscher, Odysseus Technologies

Appendix A Choice of Climber Type

Various methods of climbing the space elevator tether have been proposed. The focus here is on climbers which pull themselves up the tether as opposed to those in which the tether does the pulling. Five methods were examined: electrostatic grippers, linear induction motors, capstans, pinched-wheels and tracked climbers. Each of these is described and evaluated for practicality and efficiency. Based on these evaluations, one option is chosen to be developed in this study.

A.1 Electrostatic Gripper

The remarkable dielectric properties of alumina (aluminium oxide) can be exploited to create a strong pinching force between an insulated pair of electrodes and the space elevator tether. Figure 56 shows the arrangement, with opposing wheels on either side of the tether. In an expanded view of the wheels and tether at 0° rotation, Figure 57 shows the high voltage electrodes insulated from the tether with alumina. A thin layer of alumina (0.635 mm) has an extraordinarily high dielectric strength of 640 kV/mm, which is 6.4×10^8 V/m. This means that a high voltage can be placed across it without breakdown, and the pinching force is proportional to V^2/k^2, for voltage V and thickness k. A force of several MN can be achieved with a voltage less than 100 kV.

To hold a mass of 20,000 kg ($\approx$ 200 kN) with a coefficient of friction of 0.05, a force of 4 MN is needed, 2 MN on each side. Each electrode forms a capacitor with the tether. Let the capacitance be C and the force between one electrode and the tether be F so that

$$F = \frac{V^2 C}{k} \quad and \quad C = \frac{\epsilon_0 \sigma A}{k} \, . \tag{67}$$

Here ϵ_0 is the permittivity of free space and $\sigma = 9.9$ is the dielectric constant of CoorsTek Superstrate TPS alumina (CoorsTek 2021). A is the area of contact with the tether. Assuming a width of one meter, $A = h$, the height of the electrode and alumina film. Combining these equations gives

$$F = \frac{V^2 \epsilon_0 \sigma A}{k^2} \tag{68}$$

Setting V to the maximum safe level based on the dielectric strength s, we get $V = sk$, where $s = 6.4 \times 10^8$ V/m. Then the force equation simplifies to

$$F = s^2 \epsilon_0 \sigma A \tag{69}$$

Eq. 69 can be written in terms of the pressure $P = F/A$ exerted on the tether:

$$P = s^2 \epsilon_0 \sigma \tag{70}$$

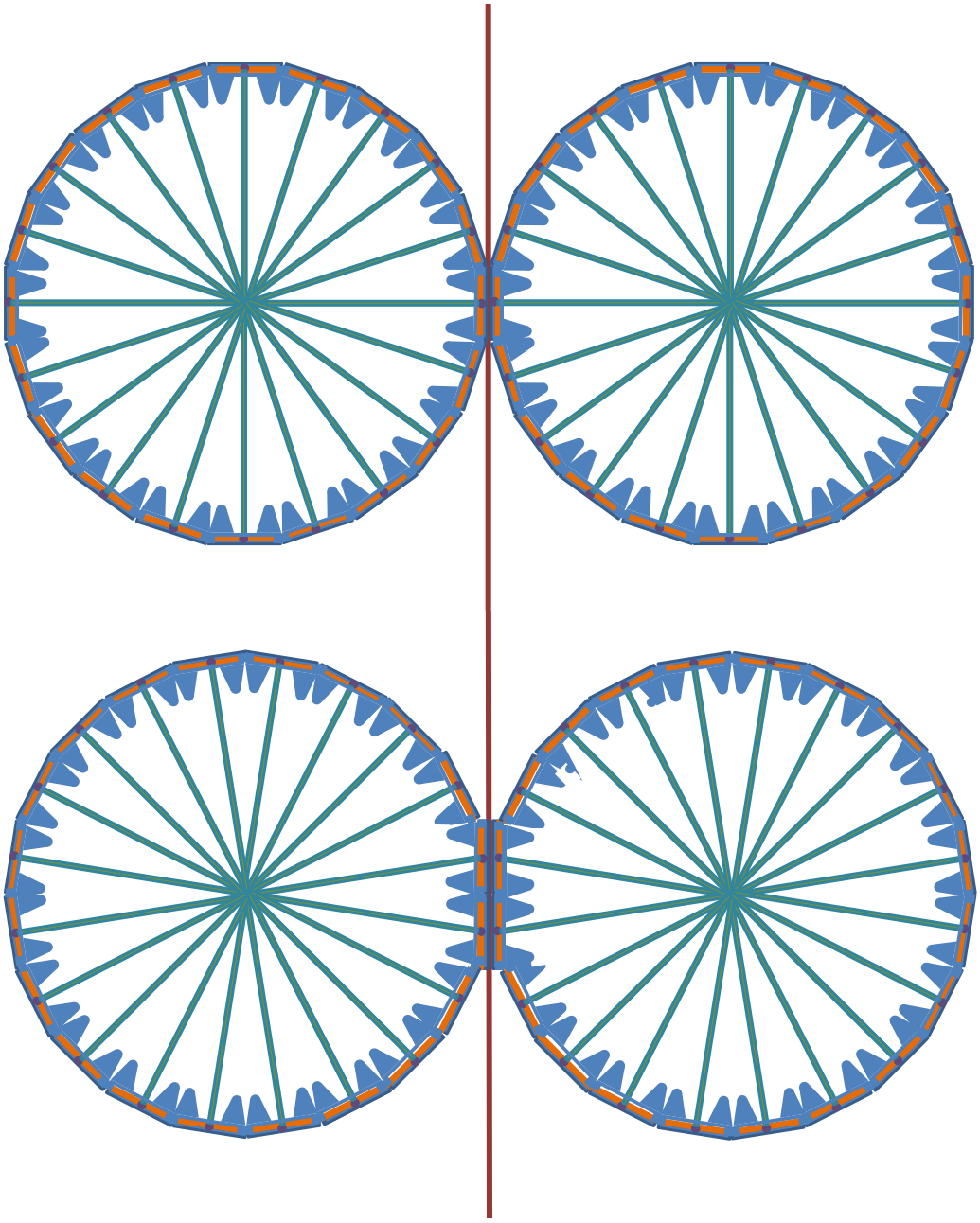

Figure 56: View, edge-on to tether, of drive wheels showing electrodes (orange) surrounded by alumina (blue) gripping the tether (red). Top: wheels at 0° rotation. Bottom: wheels at 9° rotation.

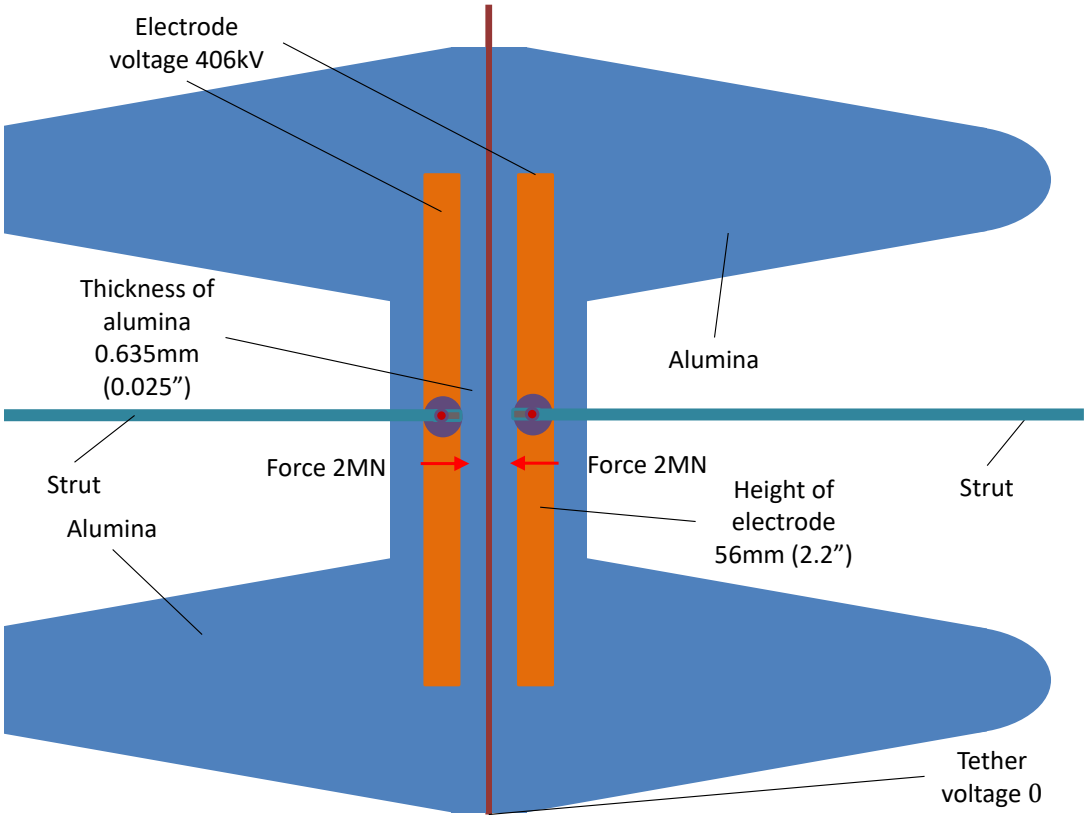

Figure 57: Expanded view of the drive wheels at 0° (Fig. 56, top) in the region where electrodes of opposing wheels are closest together.

Eq. 70 shows that the pressure depends solely on the properties of the dielectric. The force can be adjusted by adjusting the area A. Taking the tether width as 1 meter, the height h of the gripper can be found:

$$h \;=\; A \;=\; \frac{F}{s^2\epsilon_0\sigma}\;. \tag{71}$$

Hence, for a force of 2 MN, $h = 0.0557$ m or 55.7 mm.

The alumina film from CoorsTek is 0.635 mm thick, so the voltage V is $6.4\times10^8\times 0.635\times10^{-3}$, which is 406 kV. However, they state that film as thin as 0.127 mm can be produced. In that case, a voltage of only 81 kV is needed. If the 0.635 mm thickness must be used, Eq. 68 shows that the voltage can still be reduced by increasing A or, equivalently, h. To get a voltage below 100 kV, the height h of the clamp must be increased to 95 cm.

The mechanical properties of CoorsTek Superstrate TPS are shown in Table 4.

Density	Flexural strength	Elastic modulus	Poisson's ratio	Hardness	Gas permeability
3.9 g/cm^3	682 MPa	372 GPa	0.2	87	nil

Table 4: Mechanical properties of CoorsTek Superstrate TPS

The electrode plates are metal, and they are the load-bearing elements. The alumina is simply squeezed between the plates and the tether. The weight of the

climber will be supported by the electrodes, which may be made of any conducting material with sufficient strength. Graphene or aluminium are obvious candidates.

At least two electrostatic clamps will be needed to maintain a constant grip on the tether with a mechanism for swapping them over rapidly. Rapid switching will be needed to reset the voltage in order to detach a clamp. One approach could be to construct a pair of wheels with electrodes covered by alumina at the periphery, as in Figure 56. The electrodes would be on spring-loaded swivel joints to allow for them to move towards the center of the wheel as it rotates. The bottom of Figure 56 shows it after turning 9°, when two electrodes are momentarily engaged with the tether on each side.

A.1.1 Hexagonal Boron Nitride

The coefficient of friction of hBN is about 0.22 (Koskilinna et al. 2006), so the clamping force needed is $F \approx 10^5/0.22 \approx 4.5 \times 10^5$ N. The dielectric constant for hBN is $\sigma = 3.6$. Its dielectric strength s may be as high as 1200 kV/mm (Hattori et al. 2015) or as low as 794 kV/mm (Lee et al. 2011). Using the lower value in Eq. 71,

$$A \approx \frac{4.5 \times 10^5}{(7.94 \times 10^8)^2 \times 8.854 \times 10^{-12} \times 3.6} \approx 0.022\ m^2\ .$$

Taking the width to be 0.8 m instead of 1.0 m, to allow for some insulation, gives an electrode height of 28 mm. The arrangement of the electrodes is shown in Figure 58.

If tether is made of hBN, it can be used as the dielectric. An insulation layer between the tether and the electrodes would no longer be needed, making a tremendous difference to the voltage required, because the tether is so thin. Taking the tether thickness at low altitudes, where the climber's weight is greatest, to be 10 microns, the voltage difference is given by

$$V \approx sk \approx 7.94 \times 10^8 \times 10 \times 10^{-6} \approx 7940\ V.$$

The electrodes therefore need opposite voltages of ± 4kV.

A.1.2 Critique

This climbing method has two advantages: there are few moving parts to wear out or fail and the mechanical clamping force is supplied by electrostatics, not the wheel and shaft. As a result, wear and heat generation due to friction is greatly reduced. The major drawbacks are the large voltages and the short paths to ground. Leakage current is likely to be large.

A.2 Linear Induction Motors

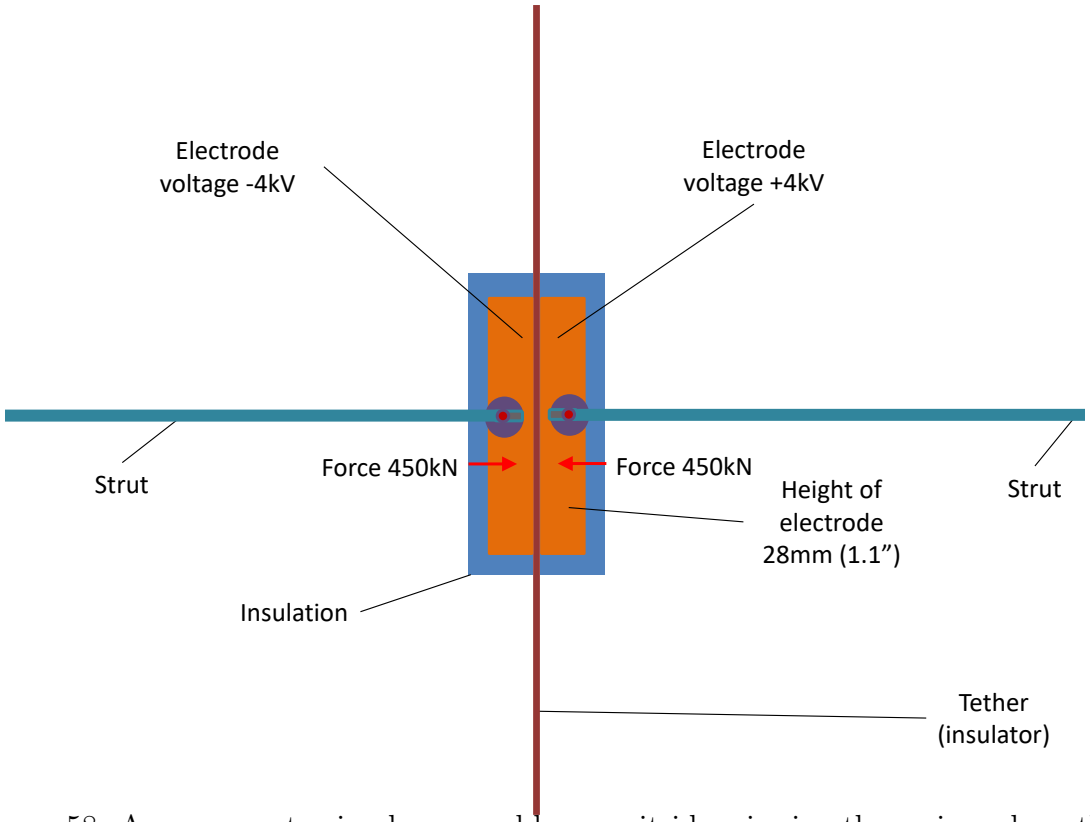

Figure 58: Arrangement using hexagonal boron nitride, viewing the region where the electrodes come closest together around the tether.

Linear induction motors (LIM) can be thought of as electric motors in which the stator is a conductive tether and the rotor is a flat electromagnet fixed to the chassis of the climber. Upward motion is produced by the induction of eddy currents in the tether against which the magnetic field of the coil reacts. Under steady-state running, the field between the tether and coil keeps the climber drive from touching the tether. The principle of a LIM drive is illustrated in Figure 59.

Moving the climber upward will require large induced currents in the tether which can be estimated using the methodology described below. It appears that graphene is the only material that will sustain high enough current densities for the space elevator application. The value of the resistance of a section of the tether can be estimated using the bulk resistivity of graphene ($1/(9.6 \times 10^7$ S/m) from Table 6) and the dimensions of a section of tether. The tether thickness is known, and a length of 1 m and a width of 0.5 m is assumed. Based on the resistance value, the current can be calculated and then converted to a current density to be compared with the measured limit for graphene. The result of this calculation, 1.03×10^{10} A/m^2, is a current density some orders of magnitude lower than the given value for graphene (10^{12} A/m^2 , Table 6), but far higher than that of copper (5×10^6 A/m^2). This current density would not be feasible for any appreciable time in any one section of graphene due to the rapid consequential temperature rise, but could be practical provided the climber was always moving at sufficient speed.

To estimate the tether heating due to the current, the power going into the tether

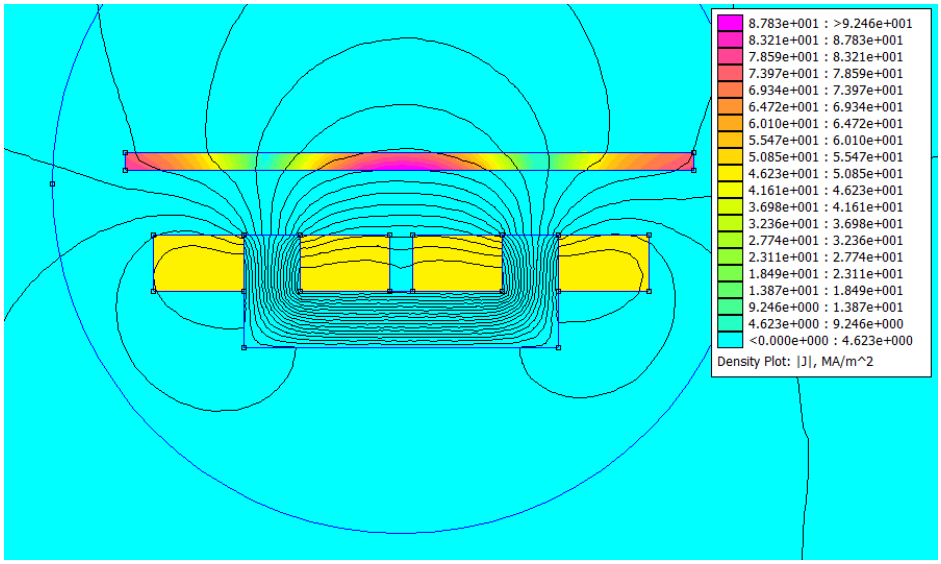

Figure 59: Cross section of linear induction motor showing magnetic field lines from the armature (bottom) interacting with a linear conductor (top). Image by Incompetence used under license: https://creativecommons.org/licenses/by-sa/3.0/

was assumed to be the difference between the input power P_{in} to the LIM magnets on the climber and the power expended to move the climber, $P_{out} = F_w V_{ct}$. F_w is the weight, or force of gravity on the climber and V_{ct} is the climber velocity relative to the tether. The efficiency is the ratio $P_{out}/P_{in} = \eta$. The excess power dissipated in the tether is $H_t = P_{in}–P_{out}$ so that

$$H_t = F_w V_{ct}(\frac{1}{\eta}–1) \ . \tag{72}$$

The tether temperature rise ΔT resulting from power input H_t also depends on the linear mass density of the tether ρ_t, the velocity of the climber V_{ct} and the specific heat capacity of the tether material c_g :

$$\Delta T = \frac{H_t}{\rho_t V_{ct} c_g} \ . \tag{73}$$

Combining Eqs. 72 and 73 yields

$$\Delta T = \frac{F_w}{\rho_t c_g}(\frac{1}{\eta} - 1) \ . \tag{74}$$

Literature suggests (Jeong et al. 2015) that 50% is typically the maximum for ϵ, but this could be as high as 66% Knapman (2021) if graphene were used in the stator (tether) and in the climber electromagnets. Superconducting climber magnets could be even better, but a value of $\epsilon = 0.5$ will be used here.

At the Earth's surface the climber weight F_w is (20,000 kg) $\times$ g = 196,133 N. The linear mass density of the tether, ρ_t is the product of the tether cross-sectional area and the material density. For a graphene tether of total mass 2.74 $\times 10^6$ kg, the area at Earth's surface is 4.1 μm $\times$ 1 m, or 4.1 $\times$ 10^{-6} m^2, with a density of 2298 kg/m^3. Thus ρ_t = 0.009422 kg/m. The specific heat capacity of graphene has been estimated at c_g = 707 J/kg/K (Picard et al. 2007). Using these values in Eq. 74 yields a temperature rise of $\Delta T = 29,443$ K.

This temperature rise is clearly excessive, meaning the LIM drive concept is not feasible at these conditions. At higher altitudes the tether will have a higher mass density and the drive force will be lower, but the problem will persist for much of the way to GEO. The maximum tether temperature is unlikely to be limited by the graphene melting point of 5000 K (see Table 6); the heating of the lower parts of the climber by radiation from the hot (perhaps incandescent) tether is likely to be a more critical factor.

It must also be noted that the efficiency depends greatly on speed as well as the motor design and tether dimensions. The optimum speed depends on the LIM design, but efficiency will fall to zero when the speed drops to zero.

The LIM concept becomes more feasible if used only at high altitudes; the low climber weight and thicker tether mean that very high speeds could be possible, even if the drive efficiency at these speeds is low.

The temperature rise is proportional to the climber mass, meaning that considerably smaller climbers with LIM drives may become be feasible, especially in the more distant future when tethers are heavier; for early space elevator systems at 50% efficiency even a 2000 kg LIM climber would not be practical below about 5000 km altitude, but a 200 kg climber should be acceptable even at the Earth's surface. The precise maximum climber mass cannot be determined as it depends on too many variables.

Whatever the climber mass, it is clear that starting from rest will be a problem, given that the low efficiency at low speeds will mean excessive temperatures. This is not a problem with terrestrial LIM drives as the stators are far more massive than the space elevator tether. The starting problem could be overcome at the Earth's surface by using some form of launch tower to accelerate the climber to an adequate velocity, but some means of re-starting from a parked position at altitude will be required, especially if the climber did not include some power source to enable climbing throughout the 'night' at lower altitudes.

A.2.1 Critique

Due to the absence of moving parts, the consequent absence of wear on components and the potentially high climber velocities, linear induction motors appear at first sight to be an excellent climber drive. They do, however, suffer from relatively low efficiency due to the open field lines which would be closed in a conventional electric motor. Also, the current drawn by a LIM is higher than a rotary motor of the

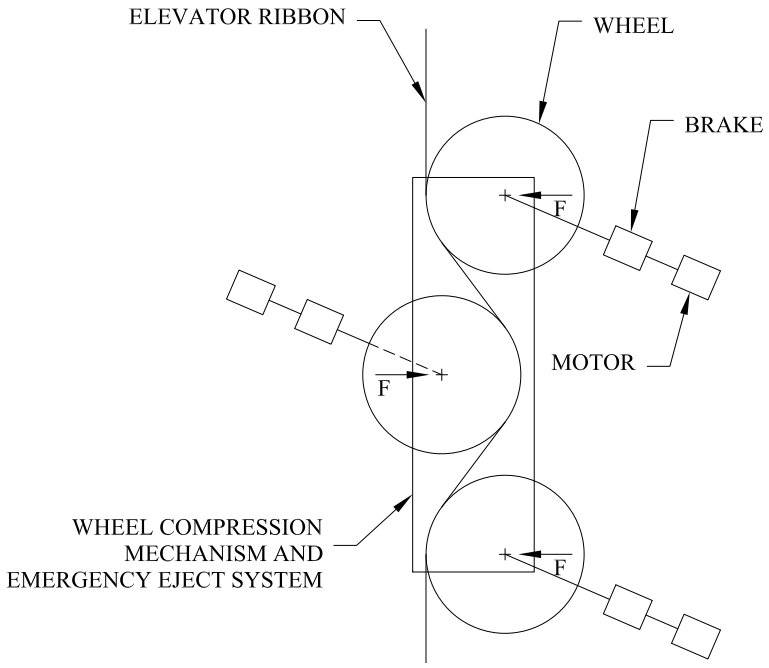

Figure 60: Block diagram of a capstan drive.

same rating. Power consumption when starting from a dead stop would be high, as would the heating of the tether due to low efficiencies. Revisiting LIM technology in the future, when higher-temperature superconductors become available, may be worthwhile.

A.3 Capstans

A block diagram of a capstan drive is shown in Figure 60. The tether is threaded through a set of wheels where it is bent in one direction around one wheel, then in the opposite direction around the next wheel, and so on. A clamping mechanism exerts transverse force to press the wheels against the tether.

The tension that supports the climber is shown in Figure 61, where a tether with thickness t is bent round a capstan of radius r through an angle θ radians. The length of that part of the tether in contact with the capstan is $r\theta$, but the outermost part extends to a length of $(r+t)\theta$. Therefore this layer is subject to the additional strain

$$\frac{(r+t)\theta - r\theta}{r\theta} = \frac{t}{r}. \tag{75}$$

Using Young's modulus of the tether, $E = 10^{12}$ Pa, leads to an additionl stress of Et/r. If the radius is 30 cm and the thickness is 10 μm, the additional stress is $10^{12} \times 10^{-5}/0.3 \approx 3.3 \times 10^{7}$. Thus the stress difference between the two sides of the

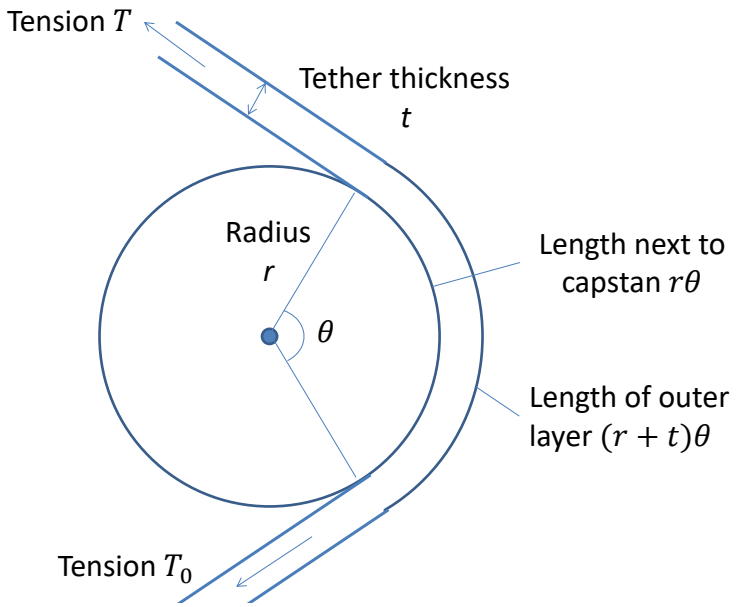

Figure 61: Tether beinding around a capstan.

tether amounts to 33 MPa, which is very small compared to the 89 GPa stress in the tether.

Now the formula for calculating the tension increase around the capstan is

$$T = T_0 e^{\mu\theta} \ . \tag{76}$$

Here μ is the coefficient of friction and T_0 is the tension in the tether below the capstan. The formula shows that the tension T above the capstan is proportional to the tension T_0 below. To hold the climber's full 200 kN weight near Earth, the capstan(s) must increase the tension by 200 kN.

A.3.1 Examples

Graphene ($\mu = 0.1$)
If $T_0 = 200$ kN then $T = 400$ kN is required. With $\mu = 0.1$,

$$\theta = \frac{1}{\mu} ln \frac{T}{T_0} = 10 \ ln2 \approx 6.9 \ radians \ , \tag{77}$$

meaning that 1.1 complete turns are needed, or about 400°. Several capstans would be needed to support the required weight. If the tension T_0 is less, then more capstans would be needed.

hBN ($\mu = 0.22$)
For the same T_0 and T, with the friction coefficient $\mu = 0.22$,

$$\theta = \frac{1}{\mu} ln \frac{T}{T_0} = \frac{1}{0.22} \ ln2 \approx 3.15 \ radians \ , \tag{78}$$

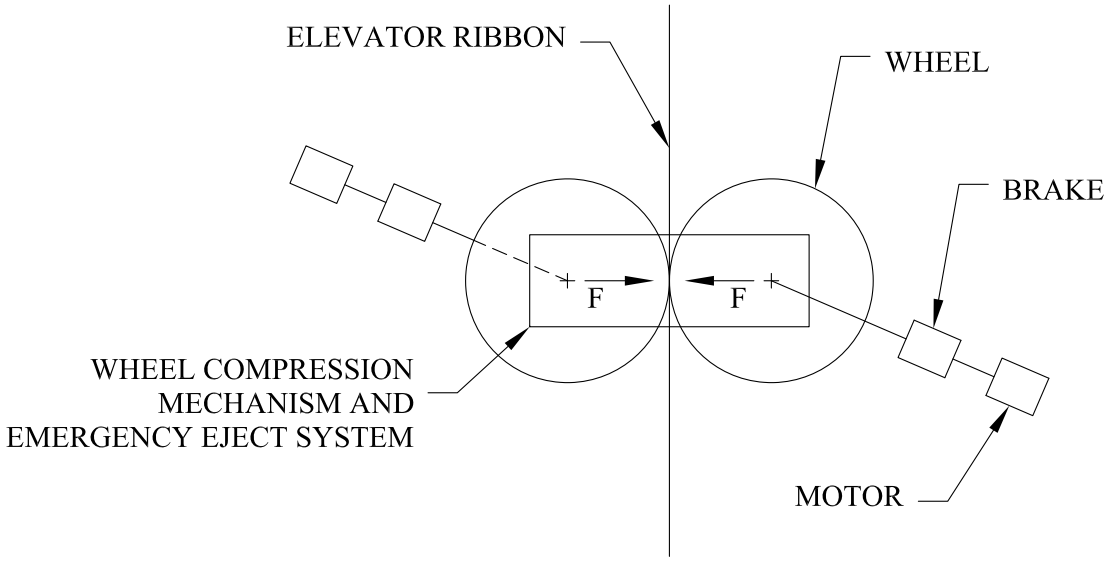

Figure 62: Block diagram of the pinched wheel drive.

so that 200° is needed. Three capstans should be enough to support the required weight.

A.3.2 Critique

A capstan drive provides a large area of contact between the tether and the wheel, making this option attractive for tether materials with low coefficients of friction. It also induces a low amount of distortion in the shape of the wheel, thereby reducing wheel fatigue and heat production due to flexing. However, it does require large transverse forces to hold the wheels against the tether. Because of the high operating tension expected in the tether, and because of its stiffness, these forces are likely to be prohibitive.

A.4 Pinched Wheel Drive

A block diagram of the pinched-wheel drive is shown in Figure 62. This drive depends entirely on friction to generate tractive force, unlike the capstan option which relies on friction and tether tension. A pinched-wheel drive unit consists of a pair of wheels pressed into direct contact with the tether by clamps so that

$$F_t = \mu F_c \ , \tag{79}$$

where F_t is the tractive force, F_c is the compression force and μ is the mutual coefficient of friction between tether and wheel. The tractive force must be great enough to support the climber against gravity and provide upward acceleration.

Although it appears that the contact area between wheels and tether is zero, clamps provide enough transverse force to deform the wheels so that their contact point with the tether has a non-zero area. The friction between the wheel and tether over this area generates the force normal to the tether which is the tractive force. The climber motors must generate sufficient torque $M = F_t R$ to rotate the wheels.

A.4.1 Critique

The pinched wheel drive with its direct contact and friction-only operation seems to be the most energy efficient option since it is likely to have less slippage than the capstan drive. Since it does not bend the tether, the magnitude of the clamping forces would appear to be reasonable. One drawback is the relatively small contact area between wheel and tether which requires either more drive wheels or a larger coefficient of friction.

A.5 Tank Tracks

The schematic in Figure 63 shows tank track drive units, each consisting of a track, or tread, wrapped around two wheels. Two such units are placed on opposite sides of the tether and clamped together in order to generate friction force and traction. The space elevator climber in Edwards & Wesling (2002) uses this type of drive and is shown in Figure 64.

Qualitatively, it is helpful to realize that tank tracks were designed to traverse bumpy and rough terrain. The track in effect smooths the passage of the tank over boulders and other bumps in its path. Tanks are able to get traction from the track in between its drive wheels because of the weight of the tank stretching the track over an obstacle between wheels. These advantages do not apply to a climber moving vertically along a perfectly smooth space elevator tether.

An examination of Figure 1 shows that, like a capstan, there is a large amount of track, or tread, in contact with each wheel. When opposing wheels are pressed together, the treads then contact the tether, and through friction, create traction. There is no added traction in the distance between opposing wheel pairs where the transverse pressure is effectively zero. The treads also increase the rotational moment of inertia J of the wheels: the thickness of the tread segment in contact with the wheel increases the wheel's effective radius as well as the wheel's mass. The effect of increased J can be seen in the expression for the torque supplied by one side of the drive train:

$$M = a\left(\frac{J}{R} + \frac{m_C R}{2}\right) + \frac{m_C g(r) R}{2} \,. \tag{80}$$

Here a is the upward acceleration of the climber, $g(r)$ is the net of the gravitational and centrifugal accelerations as a function of altitude, R is the wheel radius and m_C is the climber mass.

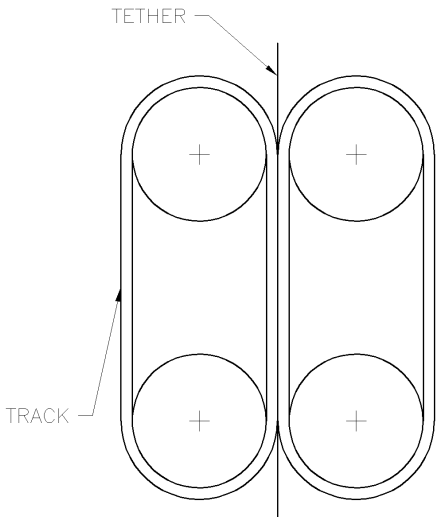

Figure 63: Tank tread drive.

Figure 64: Edwards' space elevator climber.

A.5.1 Critique

With the tank track option, the large amount of tread in contact with the tether would appear to provide abundant traction. However, large areas of the tread are not under pressure and thus provide no extra traction. In fact, traction would only occur where drive wheels inside the track are squeezed against drive wheels on the opposite side of the tether, making the tracked climber look much like a wheeled climber with useless track spinning around. In addition, the tread in contact with the wheel increases the wheel's rotational moment of inertia. Tracks also have a tendency for dynamic instability, requiring damping systems for high speed operation in military vehicles, for example. The required climb speed of a space elevator climber is well in excess of that of any existing terrestrial tracked vehicle.

As applied to a space elevator, then, tank tracks do not increase traction, but do add weight and rotational inertia which compete with payload for available tractive force. This climber option can therefore be rejected.

A.6 Summary

The climber drives considered fall into two categories: electromagnetic and frictional. The electromagnetic types do not appear to be appropriate at this time for the climber drive. The possible high leakage current of the electrostatic gripper and the relatively low efficiency of the linear induction motor are serious problems than need to be solved. Each of these options, however, deserve more study and should be reconsidered at some time in the near future.

The frictional drives appear more practical with today's technology. While the tank track option can be rejected outright as adding weight without increasing traction, the capstan and pinched wheel designs are likely candidates. Of those, the pinched wheel design was chosen for this study.

Appendix B Payload Example: Liquid Oxygen

Cryogenic fuels would be an early and particularly useful payload for the space elevator climber. A specific example is liquid oxygen (LOX).

Elon Musk gave an update on Starship in early 2022 in which he showed how much liquid oxygen (LOX) Starship needs to get to Mars: 1200 t of propellant, about 700 t of which is LOX (Wevolver 2022). This plan includes LEO refueling of Starships from tanker Starships.

A space elevator could create and supply a propellant depot at GEO to serve such major customers. At least two 5 t tanks of LOX or fuel could be sent up the space elevator every day from each of three Galactic Harbors (Swan & Fitzgerald 2018).

A concept for LOX tanks and payload attachment arms that attach to the climber, was thus developed. The initial design, shown in Figure 65 was to create CFRC tanks to contain the LOX. Each tanks weighs 242.6 kg. They can contain 4,634 kg of LOX, for a total weight of 4,877 kg. The weight of insulation around the tanks was considered negligible. No other hardware was included.

The design immediately showed subtleties that had not been considered before. The climber as designed has a center of mass that is not on the tether. If the center of mass is some distance away from the plane of the tether, the climber will cause the tether to twist. Figure 66 shows that if the tanks are identical, the arms that support the payload must be different lengths in order to keep the center of mass on the tether. A finite element analysis of the CFRC arms was performed to see if the arms were strong enough to hold the 5 t load at the end.

Figures 67 and 68 show the results of the first analysis. Stress in the arms and the climber frame exceeded the strength of the CFRC, and the deflection was far too large. The payload arms were too small in cross-section to carry the load, and their anchoring points on the climber structure were overstressed as well.

One of the most efficient ways to strengthen cantilevered beams is by increasing the height of the beam cross-section. The stiffness of the beam is a cubic function of the height of the beam cross-section. Unfortunately, the space between the axles and structural interconnects was too narrow to increase the height of the arms. Increasing that height would mean adding extra weight to the whole climber. The answer was to add more arms to help distribute the load to the frame of the climber.

Figures 69 and 70 show the effect of doubling the number of support arms. The volume of material where the stress exceeds 40 ksi (275.8 MPa) is still significant but the maximum stress has come down substantially from the 4-arm design. The maximum deflection is still 1.8 inches (45.7 mm), so too large.

The next step of strengthening the arms was to add a shear panel across pairs of arms. The effect of this is to transform the stiffness of the individual arms to the effective stiffness of a beam whose height is from the bottom surface of the lower arm to the top surface of the next arm up.

Figure 71 shows the effect on the stress distribution. The horizontal beams are

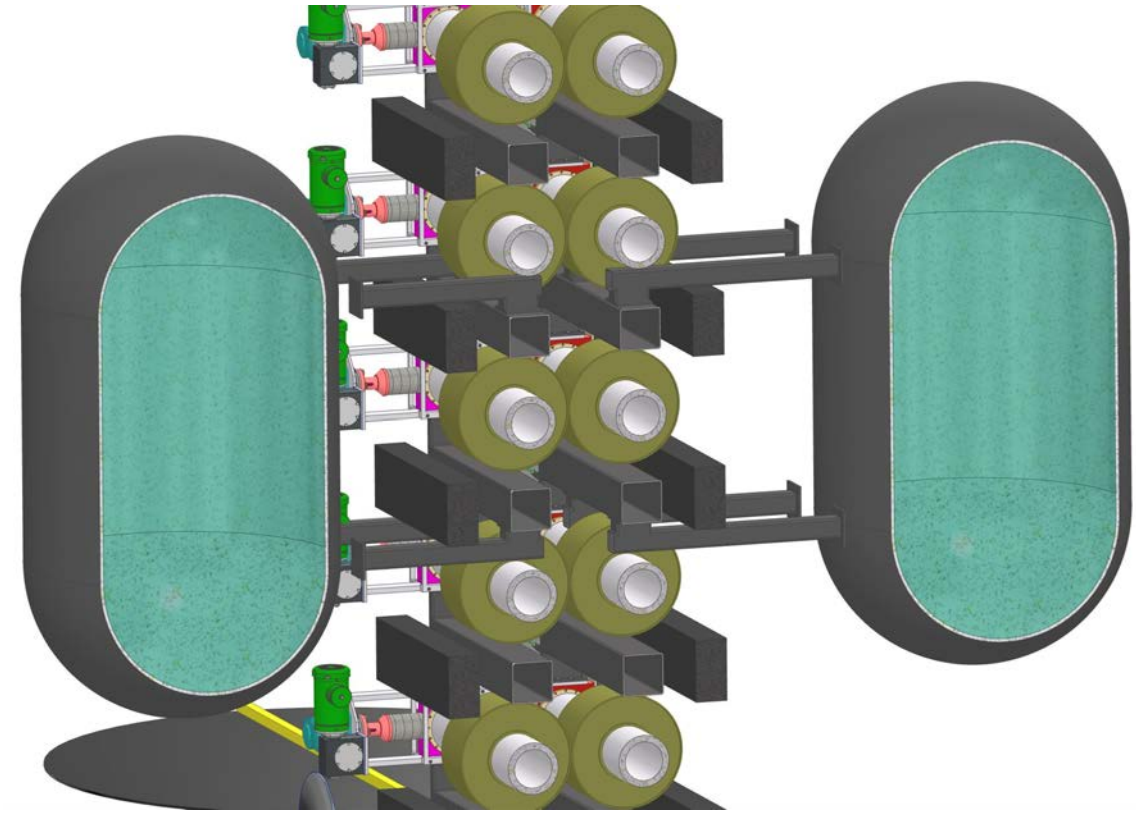

Figure 65: Initial draft of the arms to support 5 t LOX tanks

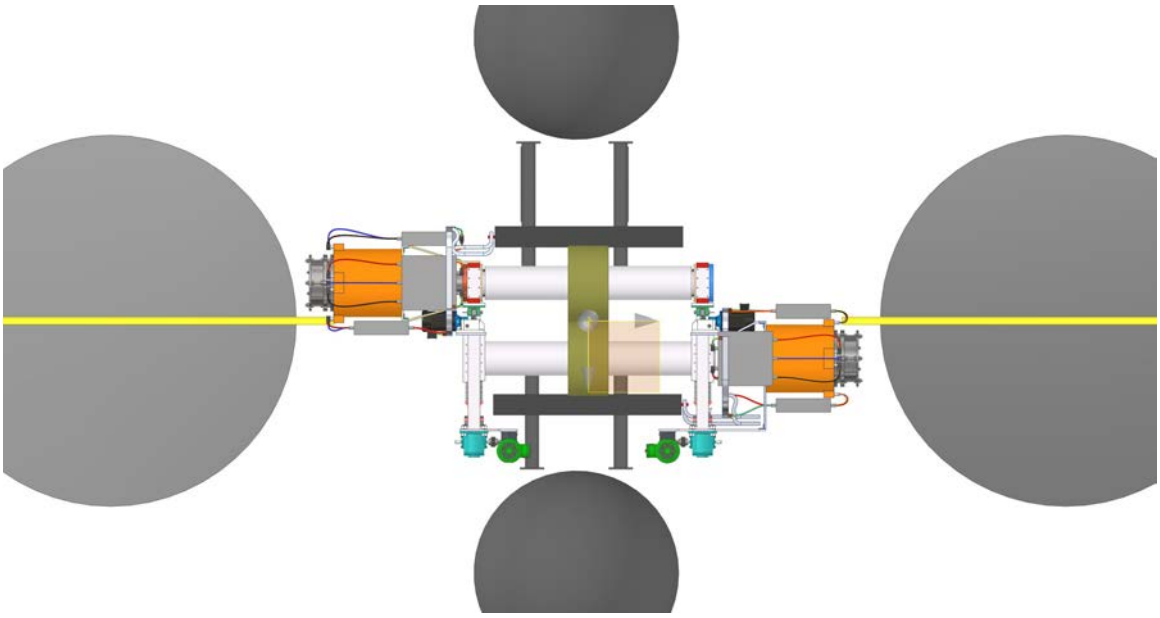

Figure 66: Top view of the climber showing its center of mass

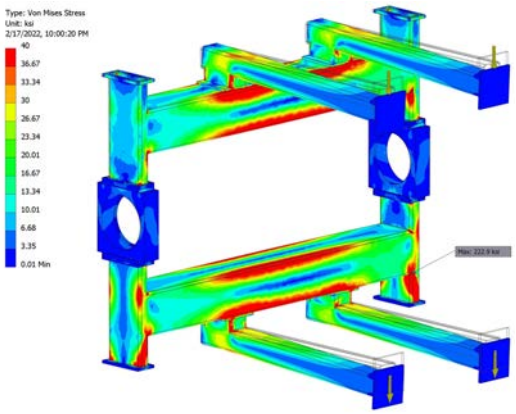

Figure 67: Von Mises stress in the four-arm climber frame from a 5 t load

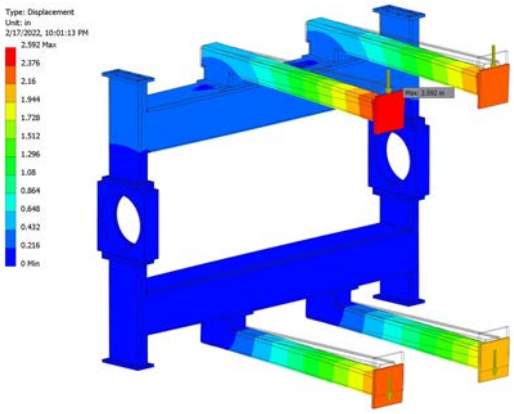

Figure 68: Deflection in the four-arm frame from a 5 t load

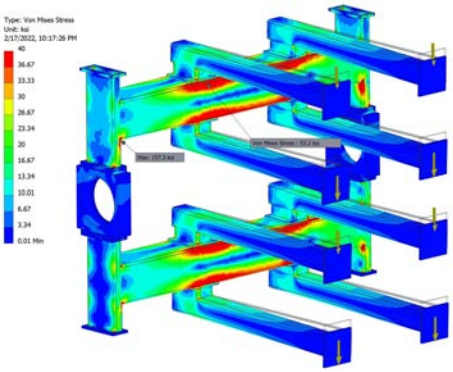

Figure 69: Von Mises plot for eight arms supporting 5 t

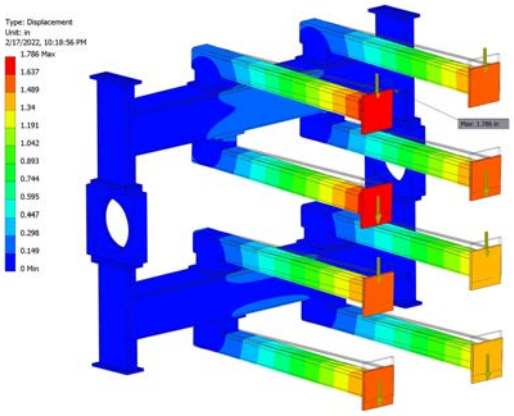

Figure 70: Total deflection plot for 8 arms holding 5 t

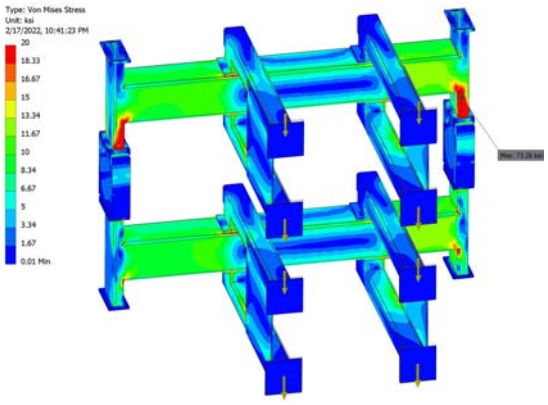

Figure 71: Von Mises stress with shear panels stiffening the arms

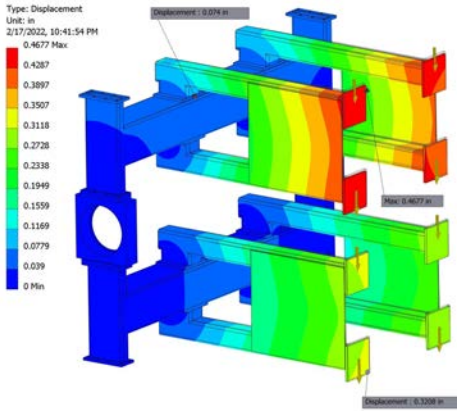

Figure 72: Total deflection for arms stiffened with shear panels

now stiff enough to move the high stress area into the smaller cross-section vertical beams of the climber frame. The maximum stress of 73.3 ksi (505.4 MPa) is still too high for the CFRC. This area will need to be redesigned in future.

Figure 72 shows that the total deflection has come down to .47 inches (17.8 mm). This might be acceptable, unless the stress is beyond the failure limit. One of the problems working with CFRC is that the published numbers for its strength can vary by orders of magnitude. If the stress exceeds the yield of the material, then the deflection is just an artifact of the static linear analysis. More work needs to be done, especially in designing connections between CFRC structures that can be assembled and disassembled as needed.

Figure 73 shows the conceptual design of the climber with two 5 t LOX tanks attached. The finite element analysis done for the long arms needs to be done for the short payload support arms on the left side of the picture.

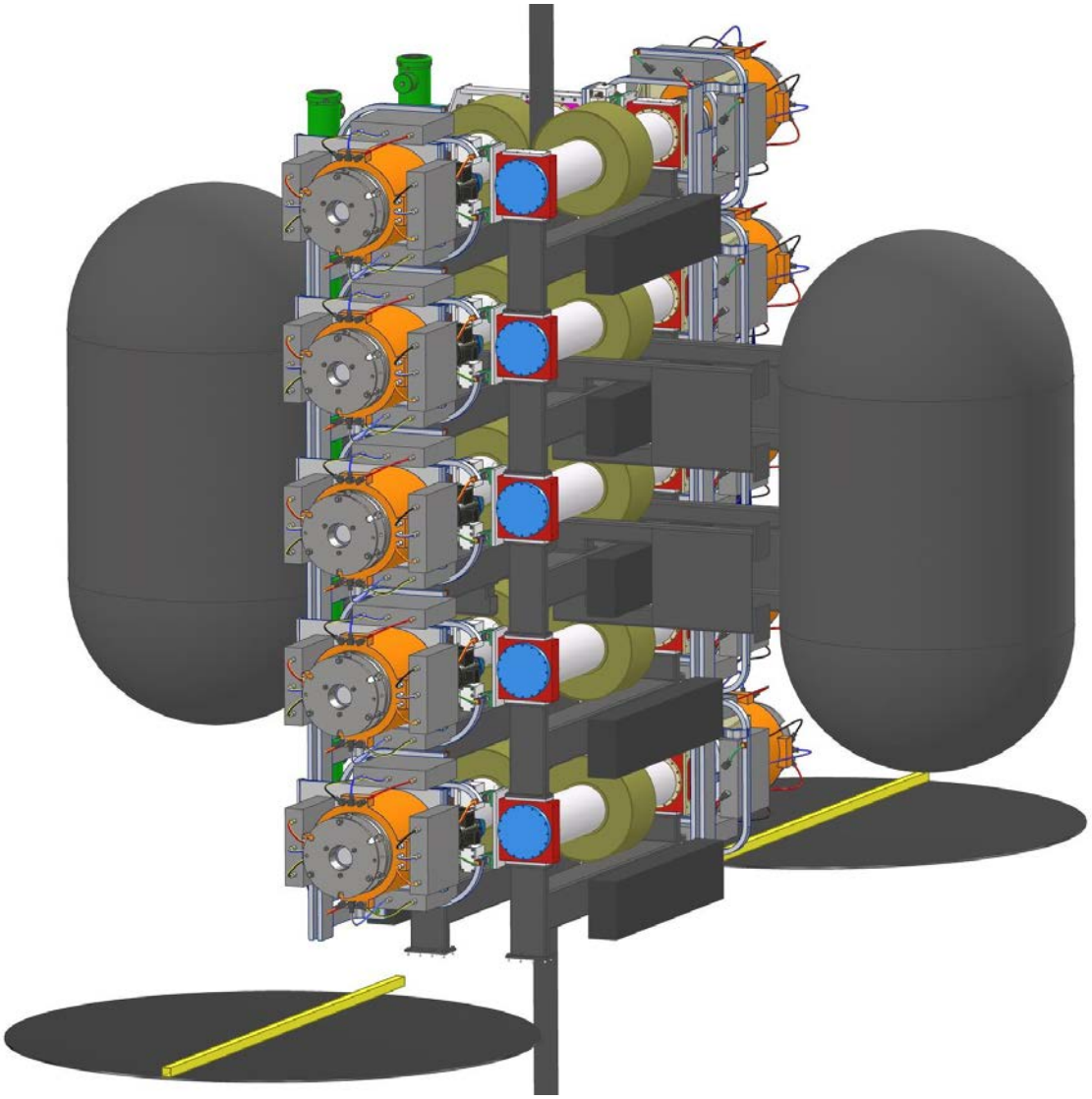

Figure 73: Rendering of final design of arms supporting LOX tanks

Appendix C Trade Space Methodology

Given the state of analysis concerning components of the space elevator system, no single solution is known. Therefore, a series of trade-space analyses needs to be performed to determine the "area" of possible solutions. There are three primary components that make up trade space analysis, namely: physical characteristics, capability attributes, and applied utility value or priority. Finding the balance among all three of these components is what drives decision outcomes. The purpose of trade space analysis is to understand the critical components, explore the relationships between them, and apply value to those relationships in a way that facilitate informed decision making. It also provides a description of several challenges associated with the conduct of trade space analysis and elements that must be contended with throughout the analysis (Smead 2015*b*).

Of the many trade space methodologies available, one is described here. The Defense Acquisition University (DefenseAcquisitionUniversity 2022), identifies several aspects of the analysis. These are performance attributes, also known as Key Performance Parameters (KPP), Key System Attributes (KSA) and Acquisition Performance Attributes (APA); they are critical in the development of effective military capabilities. Identified in Capability Development Documents (CDD), these attributes and their parameters form the requirements foundation of the proposed new materiel solution. KPPs are core performance parameters that capture the essential functionality of the system and represent the major cost drivers of the program. KPPs are so critical that a failure to meet a KPP threshold would bring the utility of the system into question and result in program reevaluation and potential cancellation. Other important performance attributes can be assigned as KSAs or APAs. Sponsors determine the performance attributes that are most critical or essential to the proposed new materiel solution. The number of attributes should be kept to the minimum necessary to properly define essential system characteristics and performance. Performance attribute values become more refined throughout the requirements and acquisition processes as a better understanding of the achievable solutions is developed. The performance attributes must be measurable and testable, and support efficient and effective Test and Evaluation (T&E).

Brantley et al. (2002) proposed that the methodology presented seeks to answer three primary questions: what is in the trade space, how are the effects of the trade space elements characterized, both qualitatively and quantitatively and when and how should decisions be made. The answers to these questions are gained through the following steps:

- define the problem, identify stakeholders and construct the trade space
- determine essential trade space interactions
- establish consistent decision criteria and metrics for each trade space entity

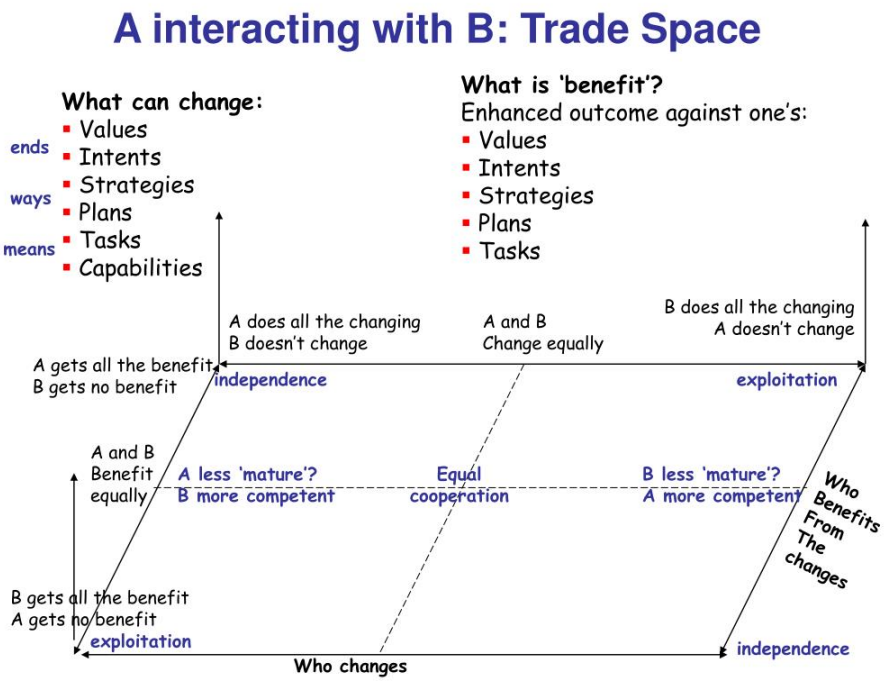

Figure 74: Interaction of items A and B in trade space. Credit: Bing Images: Trade Space Analysis

- develop a trade-off methodology which supports the making of timely trade space decisions
- document decisions, process and results.

Why Perform Trade-Space Analysis

The primary purpose for performing a trade-space analysis is to understand any critical components, identify the significance of given relationships and then to explore the relationships in order to quantify them in a concrete manner (Smead 2015*a*). Figure 74 provides an example of a trade space analysis of two items, A and B.

Steps Taken for a Trade-Space Analysis

Real-life decision analysis is a complex exercise, and usually requires the deployment of various mathematical models and statistical techniques. These basic steps (BrightHub 2011) should be followed:

- Create a model structure. While there is no hard and fast rule on the best model structure, decision trees, influence diagrams and payoff matrices find common use.
- List each possible alternative in the model structure. Possible alternatives are a finite number of possible future events, denoted as "States of Nature" identi-

fied and grouped in sets of mutually exclusive events. Represent uncertainties through probabilities and probability distributions.

- Assign numerical values to the probability of the action taking place, and the money value expected as the outcome. Assign value weights for measuring the trade-off objectives, and the risk preference to lend clarity.

- Analyze for payoffs, or expected returns. Different combinations generate different payoffs. Represent the outcome for each combination in a table, with positive (+) value for net revenue, income, or profit, and negative (-) value for expense, cost or net loss.

- Consider the payoff of each combination together with the sensitivity of the outcome, the weighted utility for key probabilities and the risk tolerance for the combination to select the most preferred alternative.

Undertaking these steps is a complex exercise and requires some practice. Although the decision analysis process lends a structure and a methodology to evaluate choices, the basis of determining numerical values still remains subjective. False assumptions, not having an accurate estimation of the probabilities, relying on expectations, and difficulties in measuring the utility function, or forecasting errors can distort the calculation greatly.

Appendix D Material Properties

Material properties are presented for graphene super-laminate (GSL), hexagonal boron nitride (hBN) and single-walled carbon nanotubes (SWCNT).

D.1 Mechanical Properties

The following abbreviations are used in Table 5 :

ρ	mass density
σ_{TS}	ultimate tensile strength
τ_{SS}	shear strength
E	Young's modulus
G	shear modulus
σ_{BS}	breaking strength
E_{2D}	second order elastic stiffness
D_{2D}	third order elastic stiffness
μ	coefficient of friction

Measure (units)	GSL	hBN	SWCNT	Citation
ρ (kg/m^3)	2260			MaterialProperties (2022)
ρ (kg/m^3)		2200		Roy et al. (2021)
ρ (kg/m^3)			1600	Sugime et al. (2013)
σ_{TS} (GPa)	70 to 130			Lee et al. (2008)
σ_{TS} (GPa)		100.5		Paul et al. (2017)
σ_{TS} (GPa)			77 to 200	Takakura et al. (2019)
τ_{SS} (GPa)	0.14			Liu et al. (2012)
E (GPa)	1000			Lee et al. (2008)
E (GPa)		716 to 977		Falin et al. (2017)
E (GPa)			1000	Takakura et al. (2019)
G (GPa)	0.19 to 0.49			Qu et al. (2019)
G (GPa)		3.07 to 4.31		Qu et al. (2019)
σ_{BS} (N/m)	42			Lee et al. (2008)
E_{2D} (N/m)	350 $\pm$ 50			Lee et al. (2008)
D_{2D} (N/m)	-650 $\pm$ 120			Lee et al. (2008)
μ	0.03			Shin et al. (2011)
μ	0.10			Dwivedi et al. (2021)
μ		0.23 to 0.27		Koskilinna et al. (2006)
μ			0.22 to 0.24	Yamamoto et al. (2008)

Table 5: Mechanical properties of possible tether materials

D.2 Electrical, Thermal and Optical Properties

The following abbreviations are used in Table 6 :

κ	electrical conductivity
j_{BD}	breakdown current density
c_g	specific heat capacity
λ	thermal conductivity
α	light absorptivity

Measure (units)	SCG	hBN	SWCNT	Citation
κ (S/m)	9.6×10^{7}			*
κ (S/m)		1.89×10^{-7}		Deng et al. (2021)
κ (S/m)			7.3×10^{4}	Puchades et al. (2015)
j_{BD} (A/m^2)	10^{12}			Murali et al. (2009)
Melting point (K)	5000 to 6000			Ganz et al. (2017)
Melting point (K)		2900		Roy et al. (2021)
Melting point (K)			4800	Zhang et al. (2007)
c_g (J/kg/K)	706.9			Picard et al. (2007)
λ (in-plane) (W/m/K)	5000			*
λ (in-plane) (W/m/K)		751		Cai et al. (2019)
λ (in-plane) (W/m/K)			6600	Berber et al. (2000)
α (%)	2.3			*

Table 6: Electrical, thermal and optical properties of possible tether materials

* Class for Physics of the Royal Swedish Academy of Sciences (2010)

D.3 Titanium Alloy Properties

The titanium alloy Ti-6Al-4V was chosen as the wheel material for this study. Its mechanical properties are given here.

Measure (units)	Value	Citation
Young's modulus (GPa)	113.8	*
Tensile yield strength (GPa)	0.88	*
Compressive yield strength (GPa)	0.97	*
Shear modulus (GPa)	44	*
Shear strength (GPa)	0.55	*

Table 7: Mechanical properties of Ti-6Al-4V alloy

* ASM Aerospace Specification Metals Inc. (2022)

Appendix E International Space Elevator Consortium

Who We Are

The International Space Elevator Consortium (ISEC) is composed of individuals and organizations from around the world who share a vision of humanity in space.

Our Vision

Space Elevators are the Green Road to Space, enabling humanity's most important missions by moving massive tonnage to GEO and beyond. They will accomplish this safely, routinely, inexpensively and daily. They are environmentally neutral.

Our Mission

The ISEC promotes the development, construction and operation of a space elevator infrastructure as a revolutionary and efficient way to space for all humanity.

What We Do

- Provide technical leadership promoting development, construction, and operation of space elevator infrastructures.
- Become the "go to" organization for all things space elevator.
- Energize and stimulate the public and the space community to support a space elevator for low cost access to space.
- Stimulate science, technology, engineering and mathematics educational activities while supporting educational gatherings, meetings, workshops, classes and other similar events to carry out this mission.

A Brief History of ISEC

The idea for an organization like ISEC had been discussed for years, but it wasn't until the Space Elevator Conference in Redmond, Washington, in July of 2008, that things became serious. Interest and enthusiasm for a space elevator had reached an all-time peak and, with Space Elevator conferences upcoming in both Europe and Japan, it was felt that this was the time to formalize an international organization. An initial set of directors and officers were elected and they immediately began the difficult task of unifying the disparate efforts of space elevator supporters worldwide.

ISEC's first Strategic Plan was adopted in January of 2010 and it is now the driving force behind ISEC's efforts. This Strategic Plan calls for adopting a yearly theme to focus ISEC activities. Because of our common goals and hopes for the future of mankind off-planet, ISEC became an Affiliate of the National Space Society in August of 2013. In addition, ISEC works closely with the Japanese Space Elevator Association.

Our Approach

ISEC's activities are pushing the concept of space elevators forward. These cross all disciplines and encourage people from around the world to participate. The following activities are being accomplished in parallel:

- Yearly conference: International Space Elevator Conferences were initiated by Dr. Brad Edwards in the Seattle area in 2002. Follow-on conferences were in Santa Fe (2003), Washington DC (2004), Albuquerque (2005/6 –smaller sessions), Seattle (2008 to 2019) and online meetings (2020-2022). Each of these conferences had multiple discussions across the whole arena of space elevators with remarkable concepts and presentations.

- Year-long technical studies: ISEC sponsors research into a focused topic each year to ensure progress in a discipline within the space elevator project. The first such study was conducted in 2010 to evaluate the threat of space debris. The products of these studies are reports that are published to document progress in the development of space elevators. They can be downloaded at www.isec.org.

- International cooperation: ISEC supports many activities around the globe to ensure that space elevators keep progressing towards a developmental program. International activities include coordinating with other major societies focusing on space, including the National Space Society (NSS), the British Interplanetary Soceity and the Japanese Space Elevator Association. In addition, ISEC supports symposia and presentations at the International Space Development Conference (NSS) and the International Academy of Astronautics and the International Astronautical Federation Congress each year.

- Publications: ISEC publishes a monthly e-Newsletter and yearly study reports.

- Reference material: ISEC is building a Space Elevator Library, including a reference database of space-elevator-related papers and publications. (See www.isec.org .)

- Outreach: People need to be made aware of the idea of a space elevator. Our outreach activity is responsible for providing the blueprint to reach societal, governmental, educational and media institutions and expose them to the benefits of space elevators. ISEC members are readily available to speak at conferences and other public events in support of the space elevator. In addition to our monthly e–Newsletter, we are also on Facebook, Instagram, LinkedIn, Twitter and YouTube.

- Legal: The space elevator is going to break new legal ground. Existing space treaties may need to be amended, new treaties may be needed and international cooperation must be sought. Insurability will be a requirement. Legal activities

encompass the legal environment of a space elevator including international maritime, air and space law. Also, there will be interest within intellectual property, liability and commerce law. Starting work on the legal foundation well in advance will result in a more rational product.

- History committee: ISEC supports a small group of volunteers to document the history of space elevators. The committee's purpose is to provide insight into the progress being achieved currently and over the last century.

- Research committee: ISEC is gathering the insight of researchers from around the world with respect to the future of space elevators. As scientific papers, reports and books are published, the research committee is pulling together this relative progress to assist academia and industry to progress towards an operational space elevator infrastructure.

ISEC is a traditional U.S. not-for-profit 501 (c) (3) organization with a board of directors and four officers: President, Vice President, Treasurer, and Secretary. inbox@isec.org / www.isec.org

Appendix F ISEC and IAA Studies

F.1 ISEC Yearly Study Reports

All past and current ISEC reports are listed here. They are available for sale in hardcopy or at no cost in pdf format at www.isec.org.

2010 – Space Elevator Survivability, Space Debris Mitigation evaluated the threat of space debris and proposed ways to reduce it.

2012 – Space Elevator Concept of Operations focused on how space elevators would be organized and operated.

2013 – Design Considerations for the Tether Climber studied the physical, operational and economic aspects which constrain space elevator climber design.

2014 – Space Elevator Architecture and Roadmaps delineated the development of the space elevator as a transportation infrastructure.

2015 – Design Considerations for the Earth Port examined the interface of the space elevator and the Earth's surface in terms of a harbor and transportation hub.

2016 – Design Considerations for the Space Elevator GEO Node and Apex Anchor considered the functional aspects of the GEO and Apex Anchor regions in terms of the transportation infrastructure and space enterprise.

2017 – Design Considerations for a Software Space Elevator Simulation studied the requirements for a software space elevator simulator and provides an outline for its development.

2018 – Design Considerations for a Multi-Stage Space Elevator examined the use of a rotating-bolt space tower at lower altitudes connecting to a tether at higher altitudes.

2019 – Today's Space Elevator looked at the development of a space elevator into a global and interplanetary transportation infrastructure.

2020 #1 – Today's Space Elevator Assured Survivability Approach for Space Debris re-examined and updated the space debris situation for 2020 and its effect on the space elevator.

2020 #2 – Space Elevators Are the Transportation Story of the 21st Century considered new mission capabilities supported by the space elevator infrastructure.

2021 - Space Elevators Are the Green Road to Space examined the environmental impact of space elevators as compared to rockets.

F.2 IAA Studies on Space Elevators

The following studies were sponsored by the International Academy of Astronautics (IAA) (www.iaaweb.org) and published by the Virginia Edition Publishing Company, Heinlein Prize Trust. They are available at https://www.heinleinbooks.com/bookstore.

2014 – Space Elevators: An Assessment of the Technological Feasibility and the Way Forward

2019 – The Road to the Space Elevator Era

References

Airbus (2021), 'Airbus to boost cold technology testing', https://www.airbus.com/en/newsroom/press-releases/2021-03-airbus-to-boost-cold-technology-testing-as-part-of-its.

Ashby, M. (2011), *Materials Selection in Mechanical Design*, Elsevier, Burlington, MA, USA.

ASM Aerospace Specification Metals Inc. (2022), 'Titanium ti-6al-4v (grade 5), annealed', https://asm.matweb.com/search/SpecificMaterial.asp?bassnum=MTP641. Accessed: 15 April 2022.

Barron, A. R. (2015), *Nanomaterials and Nanotechnology*, openstax.org Rice University, Houston.

Berber, S., Kwon, Y.-K. & Tomanek, D. (2000), 'Unusually high thermal conductivity of carbon nanotubes', *Physical Review Letters* **84**, 4613–4616.

Brantley, M. W., McFadden, W. J. & J.Davis, M. (2002), 'Expanding the trade space: An analysis of requirements tradeoffs affecting system design', *USMA Acquisition Review Quarterly* **Winter**, 1–15.

Brenner, D. W., Shenderova, O. A., Harrison, J. A., Stuart, S. J., Ni, B. & Sinnott, S. B. (2002), 'A second-generation reactive empirical bond order (rebo) potential energy expression for hydrocarbons', *Journal of Physics: Condensed Matter* **14**, 783.

BrightHub, P. (2011), 'A step-by-step explanation of the decision analysis process', https://www.brighthubpm.com/project-planning/118413-use-decision-analysis-as-a-tool-to-improve-the-quality-of-your-decisions/. Accessed: 1 October 2022.

Cai, Q., Scullion, D., Gan, W., Falin, A., Zhang, S., Watanabe, K., Taniguchi, T., Chen, Y., Santos, E. & Li, L. H. (2019), 'High thermal conductivity of high-quality monolayer boron nitride and its thermal expansion', *Science Advances* **5(6)**.

Class for Physics of the Royal Swedish Academy of Sciences (2010), 'Graphene - scientific background on the nobel prize in physics 2010', https://www.nobelprize.org/uploads/2018/06/advanced-physicsprize2010.pdf. Accessed: 14 August 2022.

CoorsTek (2021), 'Superstrate tps', https://www.coorstek.com/media/4222/thin-film-ceramic-substrates-design-guide.pdf. Accessed: 20 May 2021.

DefenseAcquisitionUniversity (2022), 'Performance attributes', https://www.dau.edu/acquipedia/pages/ArticleContent.aspx?itemid=644. Accessed: 1 October 2022.

Deng, S., Gu, Y., Wan, X., Gao, M., Xu, S., Chen, K. & Chen, H. (2021), 'Probing electronic properties of cvd monolayer hexagonal boron nitride by an atomic force microscope', *Frontiers in Materials* **8**. This paper gives the electrical resistivity for monolayer CVD hBN as 529 MΩ/cm. This was converted to S/m using the converter at https://www.cactus2000.de/uk/unit/masscnd.php.

Dwivedi, N., Ott, A. K., Sasikumar, K., Dou, C., Yeo, R., Narayanan, B., Sassi, U., Fazio, D. D., Soavi, G., Dutta, T., Balci, O., Shinde, S., Zhang, J., Katiyar, A., Keatley, P., Srivastava, A., Sankaranarayanan, S., Ferrari, A. C. & Bhatia, C. (2021), 'Graphene overcoats for ultra-high storage density magnetic media', *Nature Communications* **12**, 2854.

Edwards, B. C. & Wesling, E. A. (2002), *The Space Elevator: A revolutionary Earth-to-space transportation system*, BC Edwards, Houston.

Emrax (2021), 'Emrax electric motors', https://emrax.com. Accessed: 10 March 2021.

Falin, A., Cai, Q., Santos, E. J., Scullion, D., Qian, D., Zhang, R., Yang, Z., Huang, S., Watanabe, K., Taniguchi, T., Barnett, M. R., Chen, Y., Ruoff, R. S. & Li, L. H. (2017), 'Mechanical properties of atomically thin boron nitride and the role of interlayer interactions', *Nature Communications* p. 15815.

Fortescue, P. & Stark, J. (1995), *Spacecraft Systems Engineering, 2nd edition*, John Wiley and Sons, Chichester, UK.

Gamble, B., Snitchler, G. & MacDonald, T. (2011), 'Full power test of a 36.5 mw hts propulsion motor', *IEEE Transactions on Applied Superconductivity* **21**, 1083–1088.

Ganz, E., Ganz, A. B., Yang, L.-M. & Dornfeld, M. (2017), 'The initial stages of melting of graphene between 4000 k and 6000 k', *Physical Chemistry Chemical Physics* **19**, 3756–3762.

Gao, Y. (2015), 'Friction and peel tester thin film test'. Accessed: 3 November 2022.

GeneralElectric (2013), 'Ge successfully trials breakthrough high temperature superconducting technology for next-generation power generation', https://www.ge.com/news/press-releases/ge-successfully-trials-breakthrough-high-temperature-superconducting-technology-next.

GeneralElectric (2021), 'General electric industrial motors'.

Gibson, L. J. & Ashby, M. F. (1997), *Cellular Solids: Structure and Properties*, Cambridge University Press, Cambridge, UK.

Grolltex (2022), 'Boron nitride manufacturer grolltex; graphene rolling technologies', https://grolltex.com/product/contiguous-monolayer-hexagonal-boron-nitride-hbn-8-200mm-wafer-custom-substrate/. Accessed: 16 August 2022.

GROMACS (2022), 'Gromacs: Software suite for high-performance molecular dynamics', https://www.gromacs.org. Accessed: 15 September 2022.

Hattori, Y., Taniguchi, T., Watanabe, K. & Nagashio, K. (2015), 'Layer-by-layer dielectric breakdown of hexagonal boron nitride', *ACS Nano* **9**, 916–921.

HelixMotor (2022), 'Space elevator climber dynamics and climb frequency optimisation', https://ehelix.com/electric-powertrains/custom-built/. Accessed 26 October 2022.

Henninger, J. H. (1984), Solar absorptance and thermal emittance data of some common spacecraft thermal-control coatings, Technical report, NASA. NASA Doc. ID 19840015630.

Hohenberg, P. & Kohn, W. (1964), 'Inhomogeneous electron gas', *Physical Review* **136**, B864–B871.

Ishikawa, Y., Fuchita, Y., Hitomi, T., Inoue, Y., Karita, M., Hayashi, K., Nakano, T. & Baba, N. (2019), 'Survivability of carbon nanotubes in space', *Acta Astronautica* **165**, 129.

Janecek, M., Novy, F., Harcuba, P., Strasky, J., Trsko, L., Mhaede, M. & Wagner, L. (2015), 'The very high cycle fatigue behaviour of ti-6al-4v alloy', *Acta Physica Polonica A* **128**, 497–502.

Jeong, J.-H., Lim, J.-W., Park, D.-Y. & Choi, J.-Y. (2015), 'Characteristic analysis of a linear induction motor for 200-km/h maglev', *International Journal of Railway* **8**, 15–20.

Kane, M. (2022), 'Tesla's 4680-type battery cell teardown: Specs revealed', https://insideevs.com/news/598656/tesla-4680-battery-cell-specs. Accessed: 10 October 2022.

Knapman, J. (2021), 'Estimate of linear induction motor efficiency', private communication.

Knapman, J. K. & Swan, P. A. (2014), 'Design concepts for the first 40 km: a key step for the space elevator', *Acta Astronautica* pp. 526–530.

Knapman, J. M., Glaskowsky, P., Gleeson, D., Hall, V., Wright, D. H., Fitzgerald, M. & Swan, P. A. (2018), Design considerations for the multi-stage space elevator, Technical report, International Space Elevator Consortium.

Koskilinna, J. O., Linnolahti, M. & Pakkanen, T. A. (2006), 'Friction coefficient for hexagonal boron nitride surfaces from ab initio calculations', *Tribology Letters* **24**, 37–41.

Krulevitch, P. (1996), A technique for determining the poisson's ratio of thin films (ucrl-jc-123344; conf-961105-3), Technical report, Lawrence Livermore National Lab.

LAMMPS (2022), 'Lammps molecular dynamics simulator', https://www.lammps.org. Accessed: 15 September 2022.

Latychevskaia, T., Son, S.-K., Yang, Y., Chancellor, D., Brown, M. L., Ozdemir, S., Madan, I., Berruto, G., Carbone, F., Mishchenko, A. & Novoselov, K. S. (2019), 'Stacking transition in rhombohedral graphite', *Frontiers of Physics* **14**, 13608.

Le, D.-V., Nam, G.-D., Lee, S.-J. & Park, M. (2020), 'Conceptual design of an hts motor for future electric aircraft', *Journal of the Korea Industrial Information Systems Research* **25**, 49–57.

Lee, C., Wei, X., Kysar, J. W. & Hone, J. (2008), 'Measurement of the elastic properties and intrinsic strength of monolayer graphene', *Science* **321**, 385–388.

Lee, G.-H., Yu, Y.-J., Lee, C., Dean, C., Shepard, K. L., Kim, P. & Hone, J. (2011), 'Electron tunneling through atomically flat and ultrathin hexagonal boron nitride', *Applied Physics Letters* **99**, 243114.

Lempriere, B. M., Fenn, R. W., Crooks, D. D. & Kinder, W. C. (1969), 'Torsion testing for shear modulus of thin orthotropic sheet', *AIAA Journal* **7**, 2341–2342.

Lipp, A., Schwetz, K. A. & Hunold, K. (1989), 'Hexagonal boron nitride: Fabrication, properties and applications', *Journal of the European Ceramic Society* **5**.

Liu, Z., Zhang, S.-M., Yang, J.-R., Liu, J. Z., Yang, Y.-L. & Zheng, Q.-S. (2012), 'Interlayer shear strength of single crystalline graphite', *Acta Mechanica Sinica* **28**, 978–982.

magniX (2021), 'magnix 650 electric aircraft motor', https://magnix.aero. Accessed: 19 April 2021.

Magnomatics (2021), 'Energy efficient motors and generators', https://www.magnomatics.com. Accessed: 10 March 2021.

Maia, F. C., Samad, R. E., Bettini, J., Freitas, R. O., Nilson D. Vieira, J. & Souza-Neto, N. M. (2015), 'Synthesis of diamond-like phase from graphite by ultrafast laser driven dynamical compression', *Scientific Reports* **5**, 11812.

MaterialProperties (2022), 'Graphite: Density, strength, hardness, melting point', https://material-properties.org/graphite-density-strength-hardness-melting-point/. Accessed: 14 August 2022.

Maxwell, T., Tarau, C., Anderson, W. G., Stern, T., Walmsley, N. & Wrosch, M. (2014), 'Low-cost radiator for fission power thermal control', https://tfaws.nasa.gov/wp-content/uploads/TFAWS-2014-AT-10.pdf. Presented at Thermal and Fluids Analysis Workshop (TFAWS 2014).

MIL-HDBK-5D (1983), Metallic materials and elements for aerospace structures, Technical report, United States Navy, Naval Publications and Forms Center.

Murali, R., Yang, Y., Brenner, K., Beck, T. & Meindl, J. D. (2009), 'Breakdown current density of graphene nanoribbons', *Applied Physics Letters* **94**, 243114.

NASA (2022), 'James webb space telescope: the sunshield', https://jwst.nasa.gov/content/observatory/sunshield.html. Accessed: 9 September 2022.

Nedelea, A. (2022), 'Lithium-sulphur batteries could provide 1,200-mile per charge range', https://insideevs.com/news/411567/lithium-sulphur-li-s-batteries-tech/. Accessed: 10 October 2022.

Niu, C., Zhang, J., Zhang, H., Zhao, J., Xia, W., Zeng, Z. & Wang, X. (2022), 'Configuration stability and electronic properties of diamane with boron and nitrogen dopants', *Physical Review B* **105**, 174106.

Nixon, A. (2021), 'Charmgraphene: development of graphene-based pellicle for euv', *Nixene Journal* **5**, 43.

Nixon, A. (2022), 'Forward thinking about the cvd graphene market', *Nixene Journal* **6**, 8–11.

Nixon, A., Whieldon, R. & Nelson, D. (2021), *Graphene: Manufacturing, Applications and Economic Impact*, Nixene Publishing, Manchester, UK.

Ogura (2022), 'Electromagnetic clutches and brakes', https://ogura-clutch.com. Accessed: 5 September 2021.

Okabe, Y., Takeda, N., Yanaka, M. & Tsukahara, Y. (1999), 'Determination of the orthotropic elastic constants of thin pet film by an ultrasonic micro-spectrometer', *IEEE Transactions on Ultrasonics, Ferroelectrics, and Frequency Control* **46**, 1269–1275.

Paul, R., Tasnim, T., Dhar, R., Mojumder, S., Saha, S. & Motalab, M. A. (2017), 'Study of uniaxial tensile properties of hexagonal boron nitride nanoribbons', https://arxiv.org/pdf/1710.05790.pdf. Accessed: 20 February 2021.

Picard, S., Burns, D. T. & Roger, P. (2007), 'Determination of the specific heat capacity of a graphite sample using absolute and differential methods', *Metrologia* **44**, 294.

Puchades, I., Lawlor, C. C., Schauerman, C. M., Bucossi, A. R., Rossi, J. E., Coxa, N. D. & Landi, B. J. (2015), 'Mechanism of chemical doping in electronic-type-separated single wall carbon nanotubes towards high electrical conductivity', *Journal of Materials Chemistry C* **3**, 10256–10266.

Qu, W., Bagchi, S., Chen, X., Chew, H. B. & Ke, C. (2019), 'Bending and interlayer shear moduli of ultrathin boron nitride nanosheet', *Journal of Physics D: Applied Physics* **52**, 465301.

Ren, L., Deng, X., Xu, Y., Liu, H., Li, J., Shi, J. & Tang, Y. (2015), 'Research of hts application on tokamak magnets'. Presented at the International Conference on Power Electronics and Energy Engineering (PEEE 2015).

Robinson, P. (2022), 'Space elevator climber dynamics and climb frequency optimisation'. Presented at the 2022 International Astronautical Congress, paper D4,3,08,x68299.

Robinson, P. & Knapman, J. M. (2022), 'Space elevator tether atmospheric wind loading and a cable lift concept'. Presented at the 2022 International Astronautical Congress, paper D4,3,15,x71307.

Rodin, D. & Yee, S. K. (2017), 'Simultaneous measurement of in-plane and through-plane thermal conductivity using beam-offset frequency domain thermoreflectance', *Review of Scientific Instruments* **88**, 014902.

Rojo, M. M., Manzano, C. V., Granados, D., Osorio, M. R., Borca-Tasciuc, T. & Martin-Gonzalez, M. (2015), 'High electrical conductivity in out of plane direction of electrodeposited bi2te3 films', *AIP Advances* **5**, 087142.

Roy, S., Zhang, X., Puthirath, A. B., Meiyazhagan, A., Bhattacharyya, S., Rahman, M. M., Babu, G., Susarla, S., Saju, S. K., Tran, M. K., Sassi, L. M., Saadi, M. A. S. R., Lai, J., Sahin, O., Sajadi, S. M., Dharmarajan, B., Salpekar, D., Chakingal, N., Baburaj, A., Shuai, X., Adumbumkulath, A., Miller, K. A., Gayle, J. M., Ajnsztajn, A., Prasankumar, T., Harikrishnan, V. V. J., Ojha, V., Kannan, H., Khater, A. Z., Zhu, Z., Iyengar, S. A., da Silva Autreto, P. A., Oliveira, E. F., Gao, G., Birdwell, A. G., Neupane, M. R., Ivanov, T. G., Taha-Tijerina, J., Yadav, R. M., Arepalli, S., Vajtai, R. & Ajayan, P. M. (2021), 'Structure, properties and applications of two-dimensional hexagonal boron nitride', *Advanced Materials* **33**, 2101589.

Ruud, J. A., Josell, D., Spaepen, F. & Greer, A. L. (1993), 'A new method for tensile testing of thin films', *Journal of Materials Research* **8**, 112–117.

SAMSON (2022), 'Samson: platform for integrated molecular design', https://www.samson-connect.net. Accessed: 15 September 2022.

Shelef, B. (2011), 'The space elevator feasibility condition', *Climb* **1**, 85–92.

Shigley, J. & Mischke, C. (1989), *Mechanical Engineering Design, 5th edition*, McGraw-Hill, Inc., New York.

Shin, Y. J., Stromberg, R., Nay, R., Huang, H., Wee, A. T. S., Yang, H. & Bhatia, C. S. (2011), 'Frictional characteristics of exfoliated and epitaxial graphene', https://arxiv.org/pdf/1710.05790.pdf. Accessed: 18 February 2021.

Sinclair, R. C., Suter, J. L. & Coveney, P. V. (2018), 'Graphene–graphene interactions: Friction, superlubricity, and exfoliation', *Advanced Materials Communication* **30**, 1705791.

Smead, K. (2015*a*), A descriptive guide to conducting trade space analysis (trac-mtr-15-029), Technical report, Army TRADOC.

Smead, K. (2015*b*), A descriptive guide to trade space analysis (4feb-30apr15), Technical report, Army TRADOC.

Sugime, H., Esconjauregui, S., Yang, J., D'Arsié, L., Oliver, R., Bhardwaj, S., Cepek, C. & Robertson, J. (2013), 'Low temperature growth of ultra-high mass density carbon nanotube forests on conductive supports', *Applied Physics Letters* **103**, 073116.

Sugime, H., Sato, T., Nakagawa, R., Hayashi, T., Inoue, Y. & Noda, S. (2021), 'Ultralong carbon nanotube forest via in situ supplements of iron and aluminum vapor sources', *Carbon* **172**, 772–780.

Swan, P. A., Raitt, D. L., Swan, C. W., Penny, R. E. & Knapman, J. K. (2013), *Space Elevators: An Assessment of the Technological Feasibility and the Way Forward*, Virginia Edition Publishing Company, Houston, USA.

Swan, P. A., Swan, C. W., Penny, R. E., Knapman, J. M. & Glaskowsky, P. N. (2013), Design considerations for space elevator tether climbers, Technical report, International Space Elevator Consortium.

Swan, P. & Fitzgerald, M. (2018), Today's space elevator: the space elevator matures into the galactic harbour, Technical report, International Space Elevator Consortium.

Takakura, A., Beppu, K., Nishihara, T., Fukui, A., Kozeki, T., Namazu, T., Miyauchi, Y. & Itami, K. (2019), 'Strength of carbon nanotubes depends on their chemical structures', *Nature Communications* **10**, 3040.

Tsukahara, Y., Ohira, K. & Nakaso, N. (1990), 'An ultrasonic micro-spectrometer for the evaluation of elastic properties with microscopic resolution'. Presented at IEEE Symposium on Ultrasonics, https://ieeexplore.ieee.org/document/171498.

Tuball (2022), 'About tuball', https://tuball.com/about-tuball. Accessed: 16 August 2022.

VASP (2022), 'Vasp: The vienna ab initio simulation package', https://www.vasp.at. Accessed: 15 September 2022.

Vlassiouk, I., Stehle, Y., Pudasaini, P., Unocic, R., Rack, P., Baddorf, A., Ivanov, I., Lavrik, N., List, F., Gupta, N., Bets, K., Yakobson, B. & Smirnov, S. (2018), 'Evolutionary selection growth of two-dimensional materials on polycrystalline substrates', *Nature Materials* **17**, 318–322.

Wang, L.-F., Ma, T.-B., Hu, Y., Wang, H. & Shao, T.-M. (2013), 'Ab initio study of the friction mechanism of fluorographene and graphene', *The Journal of Chemistry C* **117**, 12520–12525.

Wang, L., Xu, X., Zhang, L., Qiao, R., Wu, M., Wang, Z., Zhang, S., Liang, J., Zhang, Z., Zhang, Z., Chen, W., Xie, X., Zong, J., Shan, Y., Guo, Y., Willinger, M., Wu, H., Li, Q., Wang, W., Gao, P., Wu, S., Zhang, Y., Jiang, Y., Yu, D., Wang, E., Bai, X., Wang, Z.-J., Ding, F. & Liu, K. (2019), 'Epitaxial growth of a 100-square centimetre single-crystal hexagonal boron nitride monolayer on copper', *Nature* **570**, 91–95.

Wevolver (2022), 'Spacex's starship - sn23, bn7', https://www.wevolver.com/specs/spacexs-starship-sn24-bn7. Accessed 6 October 2022.

Wright, D. H., Bartoszek, L., Dotson, D., Gleeson, D., Knapman, J., Lades, M., Nixon, A., Phister, P. & Robinson, P. (2021), 'The climber-tether interface of the space elevator'. Presented at 72nd International Astronautical Conference, Dubai.

Xu, K. & Liu, Y. (2022), 'Studies of probe tip materials by atomic force microscopy: a review', *Beilstein Journal of Nanotechnology* **13**, 1256–1267.

Xu, X., Zhang, Z., Dong, J., Yi, D., Niu, J., Wu, M., Lin, L., Yin, R., Li, M., Zhou, J., Wang, S., Sun, J., Duan, X., Gao, P., Jiang, Y., Wu, X., Peng, H., Ruoff, R. S., Liu, Z., Yu, D., Wang, E., Ding, F. & Liu, K. (2017), 'Ultrafast epitaxial growth of metre sized single-crystal graphene on industrial cu foil', *Science Bulletin* **62**, 1074–1080.

Yamamoto, G., Hashida, T., Adachi, K. & Tagaki, T. (2008), 'Tribological properties of single-walled carbon nanotube solids', *Journal of Nanoscience and Nanotechnology* **8**, 2665–70.

Yankowitz, M., Ma, Q., Jarillo-Herrero, P. & LeRoy, B. J. (2019), 'van der waals heterostructures combining graphene and hexagonal boron nitride', *Nature Reviews Physics* **1**, 112–125.

Yoshiasa, A., Murai, Y., Ohtaka, O. & Katsura, T. (2003), 'Detailed structures of hexagonal diamond (lonsdaleite) and wurtzite-type bn', *Japanese Journal of Applied Physics* **42**, 1694.

Zero-Max (2022), 'High-performance schmidt offset shaft couplings', https://www.zero-max.com/aca-schmidt-offset-shaft-couplings. Accessed: 11 June 2022.

Zhang, K., Stocks, G. M. & Zhong, J. (2007), 'Melting and premelting of carbon nanotubes', *Nanotechnology* **18**, 285703.

Zhang, R., Zhang, Y., Zhang, Q., Xie, H., Qian, W. & Wei, F. (2013), 'Growth of half-meter long carbon nanotubes based on schulz–flory distribution', *ACS Nano* **7**, 6156–6161.

Zipay, J. J., Modlin, T. C. & Larsen, C. E. (2015), The ultimate factor of safety for aircraft and spacecraft – its history, applications and misconceptions, Technical report, NASA. NASA Doc. ID 20150003482.

Front cover: CAD rendering of a 20 metric ton climber gripping the space elevator tether. This conceptual design, able to carry 9 tons of payload, used components available today or in the near-future.

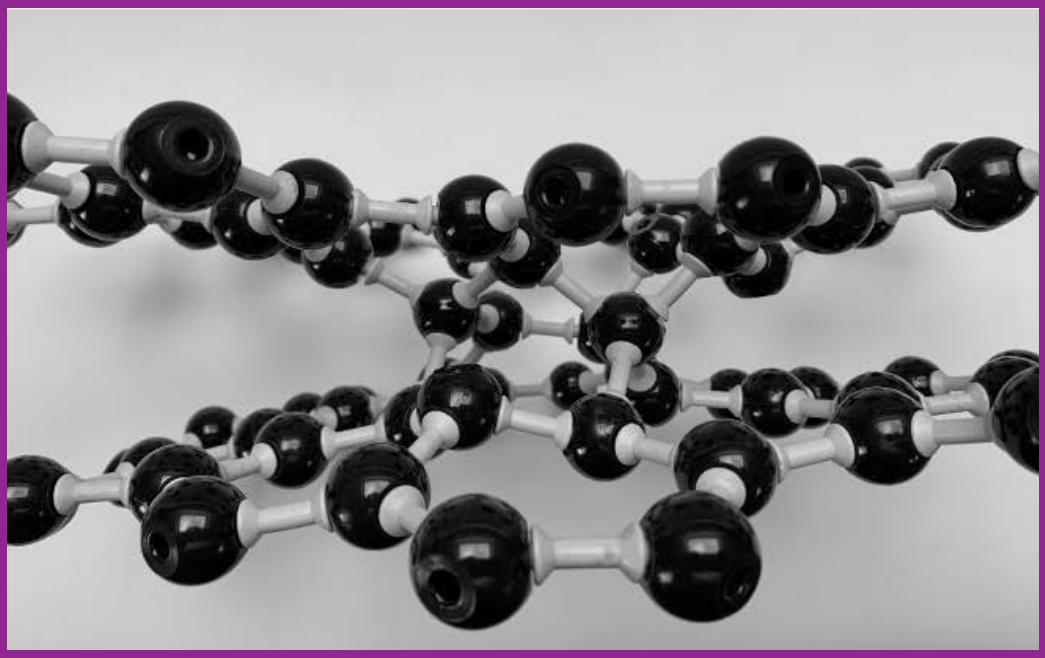

Graphene superlaminate is a prime candidate for the space elevator tether material. Shown here are two layers of single crystal graphene (top and bottom), linked by sp3 bonds (center) to increase shear strength.

The physical properties at the interface between the space elevator climber and the tether determine the minimum requirements for the tether material and the overall design of the climber.

It appears that the necessary improvements in graphene superlaminate can be made in the near future, and that 20 ton climbers with 14 ton payloads are within reach.